Influence of the resistivity on Magnetic Resonance Sounding: 1D inversion and 2D modelling

vorgelegt von
Diplom-Ingenieurin (Angewandte Geophysik)
Martina Braun
aus Berlin

von der Fakultät VI Planen Bauen Umwelt
der Technischen Universität Berlin
zur Erlangung des akademischen Grades

Doktorin der Naturwissenschaften
- Dr. rer. nat. -
genehmigte Dissertation

Promotionsausschuss:

Vorsitzender:	Prof. Tröger
Berichter:	Prof. Yaramanci
Berichter:	Prof. Legchenko (LTHE Grenoble)

Tag der wissenschaftlichen Aussprache: 10. Juli 2007

Berlin 2007
D83

Abstract

Influence of the resistivity on Magnetic Resonance Sounding: 1D inversion and 2D modelling

Martina Braun, PhD thesis, Technical University of Berlin, 2007

Magnetic Resonance Sounding (MRS, or Surface Nuclear Magnetic Resonance, SNMR) is used for groundwater exploration and aquifer characterisation to map water content and hydraulic conductivity. Since MRS is basically an electromagnetic method, the resistivity of the subsurface affects amplitude and phase of the MRS signal. The objectives of this study are, firstly, to investigate to which degree and in which way the resistivity affects MRS and, secondly, to investigate if it is possible to extract the resistivity information from MRS in the inversion.

Recently, the application of MRS has been extended from 1D to 2D water content investigations, thus, also the resistivity should be taken into account as 2D or even 3D. These investigations show the influence of a 2D resistivity model on the MRS signal compared to the calculated signal using an approximated 1D case. The results indicate that a 1D approximation is valid if the midpoint of the loop is at least one loop diameter away from the 2D structure. The substitution of a 2D resistivity with a 1D equivalent layer model has been found impossible due to the different 2D sensitivities. The impact of the 2D resistivity is also demonstrated for field data.

The most essential part of this work is the development of a new inversion scheme, which for the first time incorporates the resistivity as inversion parameter. This is the basis for using MRS as stand-alone method. The new inversion scheme takes advantage of the guided random search algorithm simulated annealing in a stable block inversion in combination with the fast convergence of a least square algorithm used for the actual resistivity inversion, that uses fixed layer thicknesses obtained from the block inversion. The successful application on field data shows that the resistivities derived from MRS are comparable to those from conventional geoelectric methods. By using an appropriate resistivity in the inversion, also the water content determination is improved.

Having also the resistivity along with the water content distribution as inversion result, MRS gives information about the mineralisation of the aquifer and thereby, the quality of the aquifer can be assessed. This is of utmost interest for further hydrogeological interpretation. This specific information cannot be achieved by geoelectrics alone, because of the nonuniqueness in resistivity concerning water content and mineralisation.

Abstract

Einfluss der Resistivität auf die Magnetische Resonanz Sondierung: 1D Inversion und 2D Modellierung

Martina Braun, Dissertation, Technische Universität Berlin, 2007

Die Magnetische Resonanz Sondierung (MRS, oder Oberflächen Nuklear Magnetische Resonanz - SNMR) wird für die Grundwasserexploration und Aquifercharakterisierung verwendet. Da MRS prinzipiell eine elektromagnetische Methode ist, beeinflusst die Resistivität des Untergrundes Amplitude und Phase des MRS Signals. Die Ziele dieser Studie sind zum einen, zu untersuchen bis zu welchem Grad und auf welche Art und Weise die Resistivität das MRS Signal beeinflusst, und zum anderen zu untersuchen ob es möglich ist, die Resistivitätsinformation aus dem MRS Signal wieder zu extrahieren.

Die Anwendung von MRS wurde mittlerweile von 1D auf 2D Wassergehaltsverteilungen ausgeweitet. Deshalb sollte auch die Resistivität in 2D oder sogar 3D berücksichtigt werden. Diese Untersuchungen zeigen den Einfluss eines 2D Resistivitätsmodells auf das MRS Signal verglichen mit dem Signal, das für einen angenäherten 1D Fall berechnet wurde. Die Ergebnisse deuten darauf hin, dass eine 1D Näherung gültig ist, wenn der Mittelpunkt der Spule mindestens einen Spulendurchmesser von der 2D Struktur entfernt ist. Aufgrund unterschiedlicher 2D Sensitivitäten, ist es nicht möglich, eine 2D Resistivität mit einer 1D äquivalenten Schicht zu ersetzen. Die Auswirkung der 2D Resistivität wird auch anhand von Felddaten demonstriert.

Der wesentlichste Teil dieser Arbeit ist die Entwicklung eines neuen Inversionsschemas, das zum ersten Mal die Resistivität als Inversionsparameter berücksichtigt. Dies ist die Grundlage, um MRS als alleinstehende Methode zu verwenden. Das neue Inversionsschema nutzt die Vorteile des zufallsbasierten Suchalgorithmus Simulated Annealing in einer stabilen Blockinversion in Kombination mit der schnellen Konvergenz eines Least Square Algorithmus', der für die eigentliche Resistivitätsinversion verwendet wird. Diese verwendet feste Schichtmächtigkeiten, ermittelt aus der Blockinversion. Die erfolgreiche Anwendung auf Felddaten zeigt, dass die Resistivitäten, die aus MRS ermittelt wurden, vergleichbar mit denen aus konventionellen geoelektrischen Methoden sind.

Hat man nun die Resistivität zusammen mit dem Wassergehalt als Inversionsergebnis, dann kann MRS Aufschluss über die Mineralisation des Aquifers geben; dadurch kann die Qualität des Aquifers abgeschätzt werden. Dies ist von besonderem Interesse für die weitere hydrogeologische Interpretation. Aufgrund der Mehrdeutigkeit der Resistivität bezüglich Wassergehalt und Mineralisation kann man diese Information nicht durch Geoelektrik allein erhalten.

Contents

1. Introduction

Several geophysical methods are used for ground water investigations. Most of them take advantage of a correlation between a physical property (e.g. electrical conductivity) and the water content. However, the interpretation is ambiguous if a change in the physical property is not only linked to a variation in the water content but may be caused also e.g. by a change in the clay content. The technique of Magnetic Resonance Sounding (MRS, also known as SNMR - Surface Nuclear Magnetic Resonance) is directly sensitive to the mobile (extractable) water content in the subsurface via the number of hydrogen protons of the subsurface (e.g. Yaramanci and Hertrich, 2006). Due to its unique capability to determine the water content directly with measurements on the surface, MRS is an important tool for hydrogeological problems (Legchenko et al., 2002; Roy and Lubczynski, 2003; Lubczynski and Roy, 2003; Vouillamoz et al., 2007).

The excitation field of the MRS is generated by a transmitter loop placed on the surface. Due to the electromagnetic attenuation, the magnetic excitation field depends on the resistivity of the subsurface. Therefore, the resistivity has to be taken into account when analysing, i.e. inverting the MRS data. Inappropriate resistivity causes a biased water content distribution in the inversion (Braun and Yaramanci, 2003). The resistivity information used in the inversion can be given by a priori information or, as now introduced in the used inversion scheme, it can be obtained during the inversion.

MRS is used for determining the amount of extractable groundwater in the subsurface. Additional electromagnetic methods are used for estimating the quality of the water via the resistivity. However, the information about the resistivity is also contained in the MRS signal itself. Having also the resistivity along with the water content distribution as inversion result, MRS gives information about the mineralisation of the aquifer and thereby, the quality of the aquifer can be estimated. This is of utmost interest for further hydrogeological interpretation. This specific information cannot be achieved by geoelectrics alone, because of the nonuniqueness in resistivity concerning water content and mineralisation.

The commercially available finite element program COMSOL Multiphysics (formerly Femlab) is used for the calculation of the excitation magnetic field considering a 2D resistivity and for a fast calculation of the excitation magnetic field considering a 1D resistivity when determining the resistivity along with the water content. In Chapter 2 the basic electromagnetic equations as well as the basic principles of the finite element methods as used in COMSOL Multiphysics are presented.

Chapter 3 gives an survey of the MRS response signal including the basic formulation of the MRS response with special emphasis on the excitation magnetic field.

The effects of a frequency shift and of the resistivity are shown for 1D modelling and inversion in Chapter 4. This includes the effects of the resistivity on the penetration depth.

As very recently MRS is extended to 2D investigations (Hertrich et al., 2005b; Yaramanci and Hertrich, 2006; Rommel et al., 2006), also the assessment of the resistivity influence as well as the inversion is needed for 2D. The influence of 2D resistivity on MRS is carefully evaluated in Chapter 5 considering geological scenarios of discontinuous and dipping layers as well as various block sizes.

The most essential part of this work is the realisation of a 1D inversion scheme for determining water content and resistivity from MRS as presented in Chapter 6. This includes a sensitivity analysis with regard to resistivity for homogeneous subsurfaces and with regard to water content, resistivity and layer depth for two 3-layer models. The inversion scheme is tested with and without the layer thickness as a priori information.

In Chapter 7 the impact of the 2D resistivity is demonstrated on field data. Additionally, the feasibility of the inversion scheme is shown on field data of two sites. The successful determination of the resistivity by MRS alone is demonstrated by comparing the resistivity derived from MRS with the resistivity derived from conventional methods such as geoelectric and time domain electromagnetic.

In summary, this thesis shows the influence of the resistivity in 1D and 2D on the MRS signal as well as a new inversion scheme for determining the resistivity along with the water content from MRS measurements. Thus, for the first time, quantitative information about the aquifer, i.e. the amount of water content, along with an estimation of the quality, i.e. the mineralisation of the aquifer, can be derived from MRS measurements alone.

2. Utilisation of the program COMSOL Multiphysics

COMSOL Multiphysics (formerly called Femlab) is an interactive environment for modelling and solving all kinds of scientific and engineering problems based on partial differential equations (PDEs). The built-in physics modes allow to build models by defining the relevant physical quantities, such as material properties, constraints, sources, and fluxes, rather than by defining the underlying equations. COMSOL Multiphysics then internally compiles a set of PDEs representing the entire model. COMSOL Multiphysics can be used as standalone product or by script programming in the MATLAB language (COMSOL, 2005).

There are three ways of describing PDEs through the following mathematical application modes:

- Coefficient form: suitable for linear or nearly linear models
- General form: suitable for nonlinear models
- Weak form: for models with PDEs on boundaries, edges, or points, or for models using terms with mixed space and time derivatives

For the calculations in this study, I used the coefficient form as predefined application mode. When solving the PDEs, COMSOL Multiphysics uses the finite element method (FEM). The software runs the finite element analysis together with adaptive meshing and error control using a variety of numerical solvers. In the 1D inversion, I used a direct solver (UMFPACK) with an adaptive mesh refinement (see Section 6.1). For the 3D calculation of the excitation magnetic field considering a 2D resistivity, the iterative solver GMRES with SSOR vector as preconditioner was used (Chapter 5). Unfortunately, it was not possible to use an adaptive mesh refinement for the 3D modelling due to internal COMSOL problems.

COMSOL Multiphysics provides optional modules for several application areas. In this study I used the Electromagnetics Module.

The first step of the process is creating the geometry. The COMSOL Multiphysics user interface contains a set of CAD tools for geometry modelling in 1D, 2D, and 3D. When the geometry is complete and various parameters are defined, COMSOL Multiphysics automatically meshes the geometry, but the user can still access the set of control parameters of the mesh generation.

2.1. Maxwell's equations

Solving electromagnetic problems on a macroscopic level implies to solve the Maxwell's equations. The Maxwell's equations state the relationships between the fundamental electromagnetic quantities: the electric field intensity $\mathbf{E}$, the electric displacement $\mathbf{D}$, the magnetic field intensity $\mathbf{H}$, the magnetic flux density $\mathbf{B}$, the current density $\mathbf{J}$, and the electric charge density ρ.

For general time-varying fields, the Maxwell's equations can be written in the differential form as

$$\nabla \times \mathbf{H} = \mathbf{J} + \frac{\partial \mathbf{D}}{\partial t} \tag{2.1}$$

$$\nabla \times \mathbf{E} = -\frac{\partial \mathbf{B}}{\partial t} \tag{2.2}$$

$$\nabla \cdot \mathbf{D} = \rho \tag{2.3}$$

$$\nabla \cdot \mathbf{B} = 0. \tag{2.4}$$

Additionally, the constitutive relations are given as

$$\mathbf{B} = \mu_0 \mu_r \mathbf{H} = \mu \mathbf{H} \tag{2.5}$$

$$\mathbf{D} = \epsilon_0 \epsilon_r \mathbf{E} = \epsilon \mathbf{E} \tag{2.6}$$

$$\mathbf{J} = \sigma \mathbf{E}. \tag{2.7}$$

Here $\mu_0 = 4\pi \cdot 10^{-7}$H/m is the permeability of vacuum, μ_r is the relative permeability of the material, $\epsilon_0 = 8.854 \cdot 10^{-12}$As/Vm is the permittivity of vacuum, and ϵ_r is the permittivity of the material. The relation defining the current density is generalised by introducing an externally generated current $\mathbf{J}^e$. Thus, Equation 2.7 becomes

$$\mathbf{J} = \sigma \mathbf{E} + \mathbf{J}^e. \tag{2.8}$$

It is often convenient to define the problems in terms of the electric scalar potential V and the magnetic vector potential $\mathbf{A}$. They are given by

$$\mathbf{B} = \nabla \times \mathbf{A} \tag{2.9}$$

$$\mathbf{E} = -\nabla V - \frac{\partial \mathbf{A}}{\partial t}. \tag{2.10}$$

Equation 2.9 is a direct consequence from Equation 2.4, and Equation 2.10 results from Equation 2.2.

The electric and magnetic potentials are not uniquely defined from Equations 2.9 and 2.10. Introducing two new potentials

$$\widetilde{\mathbf{A}} = \mathbf{A} + \nabla \Psi \tag{2.11}$$

$$\widetilde{V} = V - \frac{\partial \Psi}{\partial t} \tag{2.12}$$

gives the same electric and magnetic fields

$$\mathbf{E} = -\frac{\partial \mathbf{A}}{\partial t} - \nabla V = -\frac{\partial (\widetilde{\mathbf{A}} - \nabla \Psi)}{\partial t} - \nabla \left(\widetilde{V} + \frac{\partial \Psi}{\partial t} \right) = -\frac{\partial \widetilde{\mathbf{A}}}{\partial t} - \nabla \widetilde{V} \tag{2.13}$$

$$\mathbf{B} = \nabla \times \mathbf{A} = \nabla \times \left(\widetilde{\mathbf{A}} - \nabla \Psi \right) = \nabla \times \widetilde{\mathbf{A}}. \tag{2.14}$$

The variable transformation of the potentials is called a gauge transformation. To obtain a unique solution, constraints must be put on Ψ that make the solution unique.

2.1.1. Time-harmonic quasi-statics

In the MRS application, the dimensions of the structure in the problem are small compared to the wavelength. Thus, I used the time-harmonic quasi-static application mode.

Starting with equation

$$\nabla \times \mathbf{H} = \mathbf{J} = \sigma \mathbf{E} + i\omega \mathbf{D} + \mathbf{J}^e, \tag{2.15}$$

and using Equations 2.5, 2.6, 2.9, and 2.10, Equation 2.15 becomes

$$(i\omega\sigma - \omega^2 \epsilon)\mathbf{A} + \nabla \times \left(\mu^{-1} \nabla \times \mathbf{A} \right) + (\sigma + i\omega\epsilon)\nabla V = \mathbf{J}^e. \tag{2.16}$$

Putting the constraint of

$$\Psi = -i\frac{V}{\omega} \tag{2.17}$$

in the gauge transformation, Equations 2.11 and 2.12 result into

$$\widetilde{\mathbf{A}} = \mathbf{A} - \frac{i}{\omega}\nabla V \tag{2.18}$$

$$\widetilde{V} = 0. \tag{2.19}$$

Consequently, the equation to be solved, is

$$(i\omega\sigma - \omega^2\epsilon)\widetilde{\mathbf{A}} + \nabla \times \left(\mu^{-1}\nabla \times \widetilde{\mathbf{A}}\right) = \mathbf{J}^e, \tag{2.20}$$

and the magnetic field is calculated using Equation 2.14 (COMSOL, 2005). Equation 2.20 is used for the calculation when a 2D resistivity structure is considered (Chapter 5).

2D axial symmetric structures

For axially symmetric structures with currents present only in the angular direction, the problem can be formulated using A_φ as the only non-zero component of the magnetic vector potential $\mathbf{A}$.

The dependent variable in this application mode is the azimuthal component of magnetic vector potential $\mathbf{A}$ which obeys the relation

$$(i\omega\sigma - \omega^2\epsilon) \cdot A_\varphi + \nabla \times \left(\mu^{-1}\nabla \times A_\varphi\right) = J^e_\varphi. \tag{2.21}$$

This can be simplified to

$$(i\omega\sigma - \omega^2\epsilon) \cdot A_\varphi - \nabla \left(\mu^{-1}\nabla A_\varphi\right) = J^e_\varphi. \tag{2.22}$$

In a cylindrical coordinate system with $\partial/\partial\varphi = 0$, the equation to be solved is

$$(i\omega\sigma - \omega^2\epsilon) \cdot A_\varphi - \begin{bmatrix} \frac{\partial}{\partial r} \\ \frac{\partial}{\partial z} \end{bmatrix}^T \left(\mu^{-1} \begin{bmatrix} \frac{1}{r}\frac{\partial (r \cdot A_\varphi)}{\partial r} \\ \frac{\partial A_\varphi}{\partial z} \end{bmatrix}\right) = J^e_\varphi. \tag{2.23}$$

To avoid singularities at the symmetry axis, the transformation

$$A_\varphi = u \cdot r \tag{2.24}$$

is used:

$$r \cdot (i\omega\sigma - \omega^2\epsilon) \cdot u - \begin{bmatrix} \frac{\partial}{\partial r} \\ \frac{\partial}{\partial z} \end{bmatrix}^T \left(\mu^{-1} \begin{bmatrix} \frac{1}{r}\frac{\partial(ur^2)}{\partial r} \\ \frac{\partial(ur)}{\partial z} \end{bmatrix} \right) = J_\varphi^e \quad (2.25)$$

$$r \cdot (i\omega\sigma - \omega^2\epsilon) \cdot u - \begin{bmatrix} \frac{\partial}{\partial r} \\ \frac{\partial}{\partial z} \end{bmatrix}^T \left(\mu^{-1} \begin{bmatrix} r(\frac{\partial u}{\partial r} + 2u) \\ r\frac{\partial(u)}{\partial z} \end{bmatrix} \right) = J_\varphi^e \quad (2.26)$$

$$- \begin{bmatrix} \frac{\partial}{\partial r} \\ \frac{\partial}{\partial z} \end{bmatrix}^T \left(r\mu^{-1} \begin{bmatrix} \frac{\partial u}{\partial r} \\ \frac{\partial(u)}{\partial z} \end{bmatrix} + \begin{bmatrix} 2 \\ 0 \end{bmatrix} u \right) + r \cdot (i\omega\sigma - \omega^2\epsilon) \cdot u = J_\varphi^e. \quad (2.27)$$

COMSOL Multiphysics solves Equation 2.27 in the Azimuthal Induction Currents application mode for axially symmetric structures (COMSOL, 2005). This application mode is used for the calculation of the excitation magnetic field when conducting the 1D inversion (Chapter 6).

2.2. Basic principle of the finite element method

The finite element method (FEM) is used to solve partial differential equations (PDEs). An alternative way is the finite difference method (FDM). One of the main differences between these methods is that the FDM is an approximation to the differential equation, but the FEM is an approximation to its solution.

The solution to a PDE is found in three steps:

1. Describe the geometry of the domain Ω and the boundary conditions.
2. Build a mesh on the domain Ω.
3. Discretise the PDE and the boundary conditions to obtain a linear system $Ku = F$. The unknown vector u contains the values of the approximate solution at the mesh points.

PDEs are classified according to their order, boundary condition type, and degree of linearity. Most PDEs encountered in science and engineering are second order, i.e. the highest derivative term is a second partial derivative (Zimmerman and Hewakandamby, 2004).

The essence of the finite element is to express any constraints on the field variable in weak form. The strong form of a system of constraints is the partial differential equation system and appropriate boundary conditions. It is called strong, because the field variables are required to be continuous and have continuous partial derivatives up to the order of the equation. The weak form places a weaker restriction on the functions

that could satisfy the constraints: discontinuities must be integrable (Zimmerman and Hewakandamby, 2004).

Consider the basic elliptic equation in coefficient form

$$-\nabla(c\nabla u) + au = f \text{ in } \Omega, \tag{2.28}$$

where Ω is a bounded domain, c, a, f, and the unknown solution u are complex functions defined on Ω. Often c is called the diffusion coefficient, a is the absorption coefficient and f is the source term (COMSOL, 2005). The variable c can also be a matrix function on Ω. The boundary conditions specify a combination of u and its normal derivative on the boundary:

- Dirichlet: $hu = r$ on the boundary $\partial\Omega$.
- Generalised Neumann: $\mathbf{n} \cdot (c\nabla u) + qu = g$ on the boundary $\partial\Omega$.
- Mixed: A combination of Dirichlet and generalised Neumann boundary conditions.

The vector $\mathbf{n}$ is the outward unit normal. The coefficients g, q, h, and r are functions defined on $\partial\Omega$. The Dirichlet boundary condition specifies the values, that a solution should take on the boundaries. The traditional Neumann boundary condition refers to the case $q = 0$, thus the Neumann boundary condition specifies the values that the derivative of the solution should take on the boundaries.

The FEM approach is to approximate the PDE solution u by a piecewise linear function u_h (MATLAB, 2007b). Equation 2.28 is tested for u_h against all possible functions v of continuous piecewise polynomials. Testing means formally to multiply the residual against any function and then integrate, i.e. determine u_h such that

$$\int_\Omega (-\nabla \cdot (c\nabla u_h) + au_h - f)v \, dx = 0 \tag{2.29}$$

for all possible test functions v. Integrating by parts (i.e. using Green's formula) yields

$$\int_\Omega (c\nabla u_h)\nabla v + au_h v \, dx - \int_{\partial\Omega} \mathbf{n}(c\nabla u_h)v \, dS = \int_\Omega fv \, dx, \tag{2.30}$$

where $\partial\Omega$ is the boundary of Ω. The integrals of this formulation are well-defined even if u_h and v are piecewise linear functions (MATLAB, 2007b). The boundary integral can be replaced by the generalised Neumann boundary conditions

$$\int_\Omega (c\nabla u_h)\nabla v + au_h v \, dx - \int_{\partial\Omega} (-qu + g)v \, dS = \int_\Omega fv \, dx. \tag{2.31}$$

Equation 2.29 can be replaced with the weak for, i.e. find u_h such that

$$\int_\Omega (c\nabla u_h)\nabla v + a u_h v - f v \, dx - \int_{\partial\Omega} (-qu + g) v \, dS = 0 \ \forall v. \tag{2.32}$$

The solution u_h and the test function v belong to some function space V. In the next step, an N_p-dimensional subspace $V_{N_p} \subset V$ is chosen. Thus, the weak form of the differential equation is projected onto a finite-dimensional functions space, i.e. u_h and v are requested to lie in the function space V_{N_p} rather than V.

Since the differential operator ∇ is linear, the test function v in Equation 2.32 is replaced by N_p test functions $\Phi_i \in V_{N_p}$ that form a basis, i.e.

$$v = \Phi_i \qquad i = 1, \ldots, N_p. \tag{2.33}$$

The solution u_h is expanded in the same basis of V_{N_p}, i.e. it is decomposed onto a series of basis functions

$$u_h(x) = \sum_{j=1}^{N_p} U_j \Phi_j(x). \tag{2.34}$$

For example, if the Φ_j are sines and cosines with the fundamental and progressive harmonics, then Equation 2.34 is a Fourier series. Instead, in FEM, the basis functions are chosen to be functions that only have support within a single element, i.e. they are zero in every element but one (Zimmerman and Hewakandamby, 2004).

Thus, the following system of equations is obtained (MATLAB, 2007b)

$$\begin{aligned} \sum_{j=1}^{N_p} \left(\int_\Omega (c\nabla\Phi_j)\cdot\nabla\Phi_i + a\Phi_j\Phi_i \, dx + \int_{\partial\Omega} q\Phi_j\Phi_i \, ds \right) U_j \ &= \ \int_\Omega f\Phi_i \, dx + \\ &\int_{\partial\Omega} g\Phi_i ds \\ &i = 1, \ldots, N_p, \end{aligned} \tag{2.35}$$

which can be rewritten as

$$(K + M + Q)U = F + G \tag{2.36}$$

using

$$K_{i,j} = \int_\Omega (c\nabla\Phi_j)\cdot\nabla\Phi_i dx \ \text{(Stiffness matrix)} \tag{2.37}$$

$$M_{i,j} = \int_\Omega a\Phi_j\Phi_i dx \ \text{(Mass matrix)} \tag{2.38}$$

$$Q_{i,j} = \int_{\partial\Omega} q\Phi_j\Phi_i ds \tag{2.39}$$

$$F_i = \int_{\Omega} f\Phi_i dx \tag{2.40}$$

$$G_i = \int_{\partial\Omega} g\Phi_i ds. \tag{2.41}$$

A suitable basis for V_{N_p} is the set of "tent" or "hat" functions Φ_i. These are linear on each triangle and take the value 0 at all nodes x_j except for x_i. Requesting $\Phi_i(x_i) = 1$ yields

$$u(x_i) = \sum_{j=1}^{N_p} U_j\Phi_j(x_i) = U_i. \tag{2.42}$$

Thus, solving the FEM system means to obtain the nodal values of the approximate solution. The basis function Φ_i vanishes on all the triangles that do not contain the node x_i.

To summarise, the FEM approach is to approximate the PDE solution u by a piecewise linear function u_h, that is expanded in a basis of test functions Φ_i and the residual is tested against all the basis functions. The procedure yields a linear system $KU = F$. The components of U are the values of u_h at the nodes. For x inside a finite element, $u_h(x)$ is found by linear interpolation from the nodal values.

3. The MRS response signal

3.1. Basic formulation of the MRS response

Atoms consist of electrons and nuclei. Each atomic nucleus has four important physical properties: mass, electric charge, magnetism and spin. Whereas the first two properties are obvious, the nuclear magnetism and the nuclear spin are less self-explanatory. The magnetism of a nucleus means that the nucleus interacts with magnetic fields. However, nuclear magnetism is very weak. The spin of the nucleus can be imagined that the atomic nucleus behaves as if it is spinning around, rotating in space like a tiny planet. Spin is a form of angular momentum. However, it is not produced by a rotation of the particle, but it is an intrinsic property of the particle itself (Levitt, 2002). Spin and magnetism are closely related. The spin angular momentum $\mathbf{S}$ and the magnetic moment $\boldsymbol{\mu}$ are proportional to each other

$$\boldsymbol{\mu} = \gamma \mathbf{S}. \tag{3.1}$$

The proportionality constant is the gyromagnetic ratio γ. For hydrogen protons it is $\gamma = 0.267518\,\mathrm{rad\,s^{-1}nT^{-1}}$.

In the geophysical application of Magnetic Resonance, the groundwater is the target of investigation, i.e. the hydrogen protons of water molecules. The nuclear magnetic resonance (NMR) phenomenon is based on the behaviour of nuclear spins in a static field which is superimposed by a monochromatic field. In the Magnetic Resonance Sounding (MRS) technique, the earth's magnetic field is the static field, and a loop on the surface generates the monochromatic field. In equilibrium, the net distribution of spin is oriented along the earth's magnetic field $\mathbf{B}_0$, with magnetic moments along the field slightly more probable than magnetic moments opposed to the field (Levitt, 2002).

The spin magnetic moments in groundwater behave as an ensemble of isolated spins. The total nuclear magnetisation is the sum of innumerable small contributions from

the individual spins. The equilibrium value of the magnitude M_0 of the magnetisation vector $\mathbf{M}_N$ caused by the earth's magnetic field is calculated as

$$M_0 = \frac{\gamma^2 \hbar^2 |\mathbf{B}_0|}{4 k_B T} \frac{N}{V}, \tag{3.2}$$

where $\hbar$ is the Planck constant, k_B is the Boltzmann constant, N/V is the number of spins per volume and T is the temperature in Kelvin.

Applying an external field $\mathbf{B}_T$, oscillating with the angular Larmor frequency (Levitt, 1997)

$$\omega_0 = -\gamma |\mathbf{B}_0|, \tag{3.3}$$

the spin magnetic moments of the water molecules are forced to tilt with respect to the earth's magnetic field, which is assumed to be static within the investigation volume (Fig. 3.1a). The negative sign of the Larmor frequency indicates that the precession is in clockwise direction (Levitt, 2002). Successively deeper regions are explored by increasing the pulse moment

$$q = I_0 \tau_p \tag{3.4}$$

as multiplication of the amplitude of the transmitter current I_0 and the pulse length τ_p.

3.1.1. Excitation magnetic field

Due to electromagnetic attenuation in a conductive subsurface, the magnetic excitation field becomes elliptically polarised, and a phase delay between the transmitted field and the excitation field occurs. Studies from Trushkin et al. (1995) and Shushakov (1996) considered the resistivity of the subsurface for calculations of amplitude and phase of the MRS signal and describe the MRS signal as a complex value. However, they did not consider the elliptical polarisation and use an approximation only valid for an inclination of the earth's magnetic field of 90°, i.e. at the poles. Weichman et al. (1999, 2000) completely cover the elliptical polarisation of the excitation field and describe the complex MRS signal for arbitrary geographical locations and loop configurations.

The description of the excitation magnetic field follows the parametrisation as introduced by Weichman et al. (2000) (a detailed derivation can be found in Braun (2002), Hertrich (2005) and Hertrich et al. (2005b), a brief summary is presented in Becken and Burkhardt (2004)).

Only the field component $\mathbf{B}_T^{\perp}$ of the external field $\mathbf{B}_T$ that is perpendicular to the earth's magnetic field $\mathbf{B}_0$ acts on the spin (Weichman et al., 2000)

$$\mathbf{B}_T^{\perp} = \mathbf{B}_T - \left(\widehat{\mathbf{b}}_0 \cdot \mathbf{B}_T\right) \widehat{\mathbf{b}}_0, \tag{3.5}$$

where the following identities are used (Hertrich, 2005)

$$\mathbf{B}_T^{\perp} = B_T^{\perp} \widehat{\mathbf{b}}_T^{\perp} \tag{3.6}$$

$$\mathbf{B}_0 = B_0 \widehat{\mathbf{b}}_0. \tag{3.7}$$

In an electrically conductive subsurface, the excitation field $\mathbf{B}_T^{\perp}$ is generally elliptically polarised, and a phase delay ζ_T between the transmitter and excitation field occurs (Weichman et al. 2000). The monochromatic excitation field $\mathbf{B}_T^{\perp}$ oscillates with the Larmor frequency ω_0 in time domain with

$$\mathbf{B}_T^{\perp}(\mathbf{r}, t) = I_T^0 \left[\boldsymbol{\mathcal{B}}_{T,1}^{\perp}(\mathbf{r}, \omega_0) \cos(\omega_0 t) + \boldsymbol{\mathcal{B}}_{T,2}^{\perp}(\mathbf{r}, \omega_0) \sin(\omega_0 t)\right] \tag{3.8}$$

$$= \frac{1}{2} I_T^0 \left[\boldsymbol{\mathcal{B}}_T^{\perp}(\mathbf{r}, \omega_0) e^{-i\omega_0 t} + \boldsymbol{\mathcal{B}}_T^{\perp}(\mathbf{r}, -\omega_0) e^{i\omega_0 t}\right] \tag{3.9}$$

in which

$$\boldsymbol{\mathcal{B}}_T^{\perp}(\mathbf{r}, \pm\omega_0) = \boldsymbol{\mathcal{B}}_{T,1}^{\perp}(\mathbf{r}, \omega_0) \pm i\boldsymbol{\mathcal{B}}_{T,2}^{\perp}(\mathbf{r}, \omega_0) = \boldsymbol{\mathcal{B}}_T^{\perp *}(\mathbf{r}, \mp\omega_0) \tag{3.10}$$

is the complex field amplitude in the frequency domain. In an electrically conductive subsurface $\boldsymbol{\mathcal{B}}_{T,1}^{\perp}(\mathbf{r}, \omega_0)$ and $\boldsymbol{\mathcal{B}}_{T,2}^{\perp}(\mathbf{r}, \omega_0)$ are non-collinear, corresponding to an elliptically polarised excitation field.

The complex magnetic field vector $\mathbf{B}_T^{\perp}$ lies in the plane orthogonal to the static earth's magnetic field $\mathbf{B}_0$, that is spanned by $\widehat{\mathbf{b}}_T$ and $\widehat{\mathbf{b}}_0 \times \widehat{\mathbf{b}}_T^{\perp}$ (Fig. 3.1b). For the computation of the effective components of the excitation field, the component $\boldsymbol{\mathcal{B}}_T^{\perp}(\mathbf{r}, \omega_0)$ is decomposed in the form

$$\boldsymbol{\mathcal{B}}_T^{\perp}(\mathbf{r}, \omega_0) = e^{i\zeta_T(\mathbf{r}, \omega_0)} \left[\alpha_T(\mathbf{r}, \omega_0) \widehat{\mathbf{b}}_T + i\beta_T(\mathbf{r}, \omega_0) \widehat{\mathbf{b}}_0 \times \widehat{\mathbf{b}}_T^{\perp}\right]. \tag{3.11}$$

The elliptical polarised field $\mathbf{B}_T^{\perp}$ can then be decomposed in two circularly polarised fields $\mathbf{B}_T^{+}$ and $\mathbf{B}_T^{-}$ with opposite direction of rotation and different amplitude

$$\mathbf{B}_T^{\perp}(\mathbf{r}, t) = \mathbf{B}_T^{+}(\mathbf{r}, t) + \mathbf{B}_T^{-}(\mathbf{r}, t) \tag{3.12}$$

$$= I_T^0 \left[\alpha_T \cos(\omega_0 t - \zeta_T) \widehat{\mathbf{b}}_T + \beta_T \sin(\omega_0 t - \zeta_T) \widehat{\mathbf{b}}_0 \times \widehat{\mathbf{b}}_T^{\perp}\right]. \tag{3.13}$$

Here, α_T and β_T are the major and minor axes of the ellipse and the phase ζ_T determines the vector at $t = 0$, and it is chosen in such a way that α_t and β_T are real. We choose $\alpha_T \geq |\beta_T| \geq 0$ and $-\pi/2 < \zeta_T \leq \pi/2$ (Weichman et al., 2000). The sign of β_T determines the sense of rotation in time domain. The fields $\mathbf{B}_T^+$ and $\mathbf{B}_T^-$ can be expressed as

$$\mathbf{B}_T^+(\mathbf{r},t) = \frac{1}{2} I_T^0(\alpha_T - \beta_T)[\cos(\omega_0 t - \zeta_T)\widehat{\mathbf{b}}_T - \sin(\omega_0 t - \zeta_T)\widehat{\mathbf{b}}_0 \times \widehat{\mathbf{b}}_T^{\perp}] \quad (3.14)$$

$$\mathbf{B}_T^-(\mathbf{r},t) = \frac{1}{2} I_T^0(\alpha_T + \beta_T)[\cos(\omega_0 t - \zeta_T)\widehat{\mathbf{b}}_T + \sin(\omega_0 t - \zeta_T)\widehat{\mathbf{b}}_0 \times \widehat{\mathbf{b}}_T^{\perp}]. \quad (3.15)$$

Only the field component $\mathbf{B}_T^+$ which is co-rotating with the precessing spin and perpendicular to $\mathbf{B}_0$ excites the spin. The amplitude of the counter-rotating field $\mathbf{B}_T^-$ scales the signal response (Fig. 3.1b). The MRS signal evolves from an integrated 3D volume. So the spatial distribution of all three components of the excitation field (amplitudes of the co-rotating field $\mathbf{B}_T^+ = \frac{1}{2} I_T^0(\alpha_T - \beta_T)$ and counter-rotating field $\mathbf{B}_T^- = \frac{1}{2} I_T^0(\alpha_T + \beta_T)$ as well as the phase delay ζ_T) must be calculated for computing the MRS signal.

Computation of the field components

From the combinations

$$\boldsymbol{\mathcal{B}}_T^{\perp} \cdot \boldsymbol{\mathcal{B}}_T^{\perp} = (\alpha_T^2 - \beta_T^2) e^{2i\zeta_T} \quad (3.16)$$

$$\boldsymbol{\mathcal{B}}_T^{\perp} \cdot \boldsymbol{\mathcal{B}}_T^{\perp *} = \alpha_T^2 + \beta_T^2 \quad (3.17)$$

$$\boldsymbol{\mathcal{B}}_T^{\perp} \times \boldsymbol{\mathcal{B}}_T^{\perp *} = -2i\alpha_T \beta_T \widehat{\mathbf{b}}_0 \quad (3.18)$$

one obtains after some algebra (for details see Braun (2002))

$$\alpha_T = \frac{1}{\sqrt{2}} \sqrt{\left|\boldsymbol{\mathcal{B}}_T^{\perp}\right|^2 + \left|\left(\boldsymbol{\mathcal{B}}_T^{\perp}\right)^2\right|} \quad (3.19)$$

$$\beta_T = \operatorname{sign}\left[i\widehat{\mathbf{b}}_0 \cdot \boldsymbol{\mathcal{B}}_T^{\perp} \times \boldsymbol{\mathcal{B}}_T^{\perp *}\right] \frac{1}{\sqrt{2}} \sqrt{\left|\boldsymbol{\mathcal{B}}_T^{\perp}\right|^2 - \left|\left(\boldsymbol{\mathcal{B}}_T^{\perp}\right)^2\right|} \quad (3.20)$$

$$e^{i\zeta_T} = \sqrt{\frac{\left(\boldsymbol{\mathcal{B}}_T^{\perp}\right)^2}{\left|\left(\boldsymbol{\mathcal{B}}_T^{\perp}\right)^2\right|}}. \quad (3.21)$$

The unit vector $\widehat{\mathbf{b}}_T^{\perp}$ is finally determined from equation 3.11 as

$$\widehat{\mathbf{b}}_T^{\perp} = \frac{1}{\alpha_T} \mathfrak{Re}\left(e^{i\zeta_T} \boldsymbol{\mathcal{B}}_T^{\perp}\right). \quad (3.22)$$

3.1.2. Measured MRS signal

After pulse cut-off, the receiver loop measures the alternating magnetic field evolving from the precessional movement of the spins. In coincident loop configuration, as it is used for the studies in this thesis, the same loop used for transmission is also used as receiver loop. Due to relaxation forces, the MRS signal decays exponentially with a time constant T_2^* and has a resulting phase shift φ_0 relative to the transmitter field

$$E(t,q) = E_0(q)\exp(-t/T_2^*(q))\cos(\omega_0 t + \varphi_0(q)), \tag{3.23}$$

where $q = I_0\tau$ is the pulse moment as multiplication of the amplitude of the transmitter current I_0 and the pulse length τ. The phase shift φ_0 depends on the electromagnetic phase delay $(\zeta_T + \zeta_R)$, due to the electrical conductivity of the medium, and on other parameters such as varying Larmor frequency (see Section 4.1). The signal is measured after an instrumental delay τ_d ("dead time"). Thus, the initial amplitude E_0 and phase φ_0 are extrapolated to (Legchenko and Valla, 1998; Braun et al., 2005a)

$$E_0(q) = E(\tau_d, q)\exp(\tau_d/T_2^*(q)) \tag{3.24}$$

$$\varphi_0(q) = \varphi(\tau_d, q) - \Delta\omega(q)\tau_d, \tag{3.25}$$

where $\Delta\omega$ is the difference between the angular frequency of the excitation field, assumed to be very close to the angular Larmor frequency, and the actual measured angular Larmor frequency of the MRS signal. The four parameters $E(\tau_d, q)$, $T_2^*(q)$, $\varphi(\tau_d, q)$, and $\Delta\omega(q)$ are estimated from the in-phase and out-of-phase part of the recorded signal during the post-detection signal processing (Legchenko and Valla, 1998; Iris Instruments, 2000). These parameters are used to extrapolate the measured amplitude and phase values after the delay time $t = \tau_d$ to the initial amplitude and phase at time $t = 0$. The time record of the amplitude is an exponential decay, the phase curve has a linear behaviour. The following study uses the initial amplitude and phase value of the signal. Investigations on the decay time in modelling and inversion can be found in Schirov et al. (1991); Mohnke and Yaramanci (2002, 2005); Roy and Lubczynski (2005).

The complex voltage amplitude $E_0(q, \rho(V))$ relates linearly to the water content distribution $f(\mathbf{r})$ via the kernel function $K(q, \mathbf{r}, \rho(V))$

$$E_0(q, \rho(V)) = \int K(\mathbf{r}, q, \rho(V))\, f(\mathbf{r}) dV, \tag{3.26}$$

where the complex kernel depends on local constants, measurement configuration and ground sensitive parameters such as the resistivity $\rho(V)$ of the investigation volume. The MRS response signal E_0 at time $t = 0$ in the general case of separated transmitter and receiver loops is calculated as

$$\begin{aligned} E_0 &= \omega_0 M_0 \int_V d^3r\, f(\mathbf{r}) \sin\left(\gamma \frac{q}{I_0} \left|\mathbf{B}_T^+(\mathbf{r},\omega_0,\rho(V))\right|\right) \\ &\quad \times \frac{2}{I_0} \left|\mathbf{B}_R^-(\mathbf{r},\omega_0,\rho(V))\right| \cdot e^{i[\zeta_T(\mathbf{r},\omega_0,\rho(V))+\zeta_R(\mathbf{r},\omega_0,\rho(V))]} \\ &\quad \times \left[\hat{\mathbf{b}}_R^{\perp}(\mathbf{r},\omega_0,\rho(V)) \cdot \hat{\mathbf{b}}_T^{\perp}(\mathbf{r},\omega_0,\rho(V)) + i\hat{\mathbf{b}}_0 \cdot \hat{\mathbf{b}}_R^{\perp}(\mathbf{r},\omega_0,\rho(V)) \times \hat{\mathbf{b}}_T^{\perp}(\mathbf{r},\omega_0,\rho(V))\right]. \end{aligned} \tag{3.27}$$

The derivation of this basic MRS formula is given in Weichman et al. (2000) as well as in Braun (2002) and Hertrich (2005). Parameters evolving from the transmitter loop are denoted with the subscript T. Parameters associated to the receiver loop are denoted with the subscript R. The components of the virtual magnetic field of the receiver loop are calculated analogously to the components of the magnetic field caused by the transmitter loop.

For coincident transmitter and receiver loops, i.e. $\mathbf{B}_R = \mathbf{B}_T$ and $\hat{\mathbf{b}}_R^{\perp} \parallel \hat{\mathbf{b}}_T^{\perp}$, Equation 3.27 simplifies to

$$\begin{aligned} E_0(q,\rho(V)) &= \omega_0 M_0 \int_V d^3r\, f(\mathbf{r}) \sin\left(\gamma \frac{q}{I_0} \left|\mathbf{B}_T^+(\mathbf{r},\omega_0,\rho(V))\right|\right) \\ &\quad \times \frac{2}{I_0} \left|\mathbf{B}_T^-(\mathbf{r},\omega_0,\rho(V))\right| \cdot e^{i2\zeta_T(\mathbf{r},\omega_0,\rho(V))}. \end{aligned} \tag{3.28}$$

Thus, the MRS kernel function in the case of coincident transmitter and receiver loops is calculated as

$$K(q,\mathbf{r},\rho(V)) = \frac{2}{I_0}\omega_0 M_0 \left|\mathbf{B}_T^-(\mathbf{r},\omega_0,\rho(V))\right| \sin\left(\gamma \frac{q}{I_0} \left|\mathbf{B}_T^+(\mathbf{r},\omega_0,\rho(V))\right|\right) \cdot e^{i2\zeta_T(\mathbf{r},\omega_0,\rho(V))}. \tag{3.29}$$

For 2D conditions, Equation 3.26 becomes

$$E_0(q,\rho(V)) = \int_0^{\infty}\int_{-\infty}^{\infty} K_{2D}(q;\rho(V);x,z) \cdot f(x,z)\, dxdz \tag{3.30}$$

$$K_{2D}(q;\rho(V);x,z) = \int_{-\infty}^{\infty} K(q;\rho(V);x,y,z)\, dy, \tag{3.31}$$

where K_{2D} is the 2D kernel function assuming that $\partial f(x,y,z)/\partial y = 0$ is valid. 2D resistivity and water content models are considered in Chapter 5.

For a horizontally stratified water content distribution, $f(\mathbf{r}) = f(z)$, Equation 3.26 reduces to

$$E_0(q,\rho(V)) = \int K_{1D}(q,\rho(V),z) f(z)\, dz \tag{3.32}$$

$$K_{1D}(q,\rho(V),z) = \int_{x,y} K\left(q,\rho(V);x,y,z\right) dxdy. \tag{3.33}$$

Equation 3.32 is the basis for the 1D inversion in Chapter 6. When determining the resistivity along with the water content during the inversion, the kernel function must be recalculated in each iteration step.

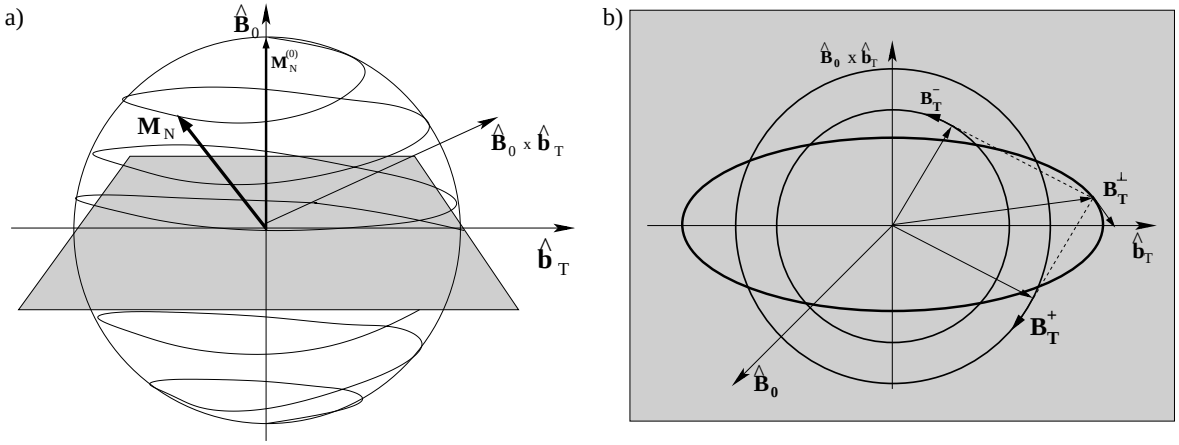

Figure 3.1.: a) Precession of the magnetisation vector $\mathbf{M}_N$ clockwise around the earth's magnetic field $\mathbf{B}_0$. b) Decomposition of an elliptically polarised field $\mathbf{B}_T^\perp$ into two opposite circularly polarised fields $\mathbf{B}_T^+$ and $\mathbf{B}_T^-$. The symbol "^" denotes unit vectors.

4. Evaluation of the effects of frequency shift and 1D resistivity on MRS

4.1. Effects of the frequency shifts on MRS

Under field conditions, the earth's magnetic field varies during one measurement due to the diurnal variation and the variation caused by different magnetic properties of the investigated volume. Consequently, the (angular) Larmor frequency ω_0 changes during one measurement, too. Thus, there is a frequency offset $\Delta\omega$

$$\Delta\omega = \omega_0 - \omega_{\mathrm{rf}} \tag{4.1}$$

between the (angular) clock frequency ω_{rf} of the transmitted radio frequency pulse and the actual measured (angular) Larmor frequency ω_0.

In equilibrium, the spin polarisation is initially along the z-axis. After applying an oscillating magnetic field with the Larmor frequency, it is rotated by 90° about the x-axis, and the result is a spin polarisation along the $-y$-axis (Fig. 4.1). Since the pulse rotates the polarisation of every single spin in the sample by the same angle, the pulse also rotates the entire nuclear magnetisation distribution of the sample. The net spin polarisation along the z-axis is therefore transferred into a net spin polarisation along the $-y$-axis, i.e. along an axis perpendicular to the magnetic field (Levitt, 2002).

In case of off-resonance of the pulse, the rotation axis of the spin polarisation has a z-component as well as an x- and a y-component. The axis is therefore tilted out of the xy-plane. The sense of the tilt depends on the sign of $\Delta\omega$ (Fig. 4.2). If $\Delta\omega$ is positive, the axis is tilted in the positive x-direction, i.e. "above" the plane. If $\Delta\omega$ is negative, the axis is tilted in the negative x-direction, i.e. "below" the plane (Levitt, 2002).

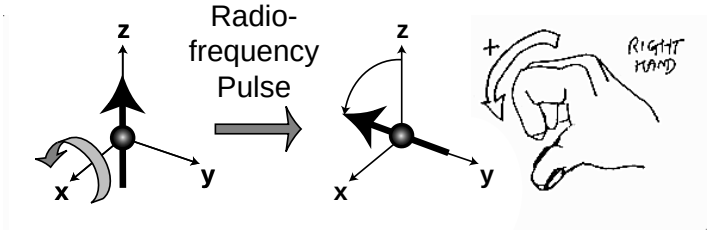

Figure 4.1.: Rotation of a spin around the x-axis (Levitt, 2002).

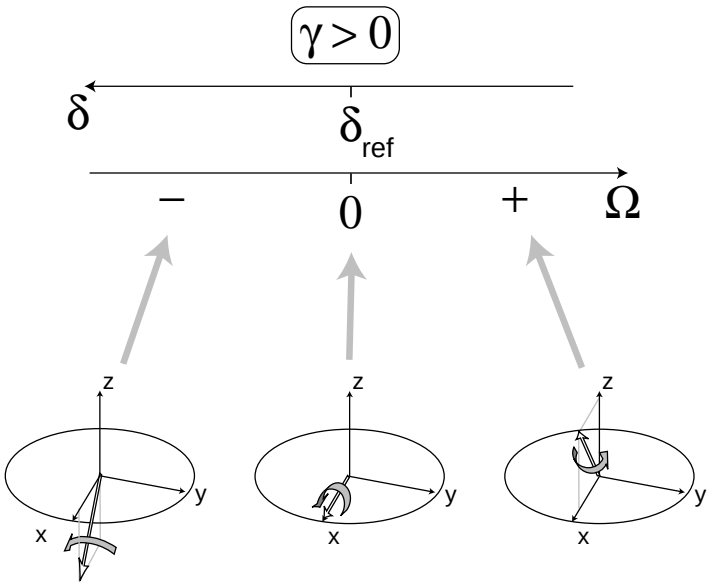

Figure 4.2.: Rotation axes for off-resonance pulses (Levitt, 2002).

The total precession angle θ of the spin is then

$$\theta = \gamma B_{\text{eff}}\,\tau = \omega_{\text{eff}}\,\tau \tag{4.2}$$

using

$$\omega_{\text{eff}} = \sqrt{\omega_1^2 + \Delta\omega^2} \tag{4.3}$$

$$\omega_1 = \gamma \left|\mathbf{B}_T^+\right|. \tag{4.4}$$

The behaviour of the elemental spin magnetisation δM_0 is sketched in Figure 4.3. At time $t = \tau$, it has three components, which from Figure 4.3 are deduced to (Mansfield et al., 1979)

$$M_x = M_0 \sin\Phi\cos\Phi(1-\cos\Theta) \tag{4.5}$$

$$M_y = M_0 \sin\Phi\sin\Theta \tag{4.6}$$

$$M_z = M_0\left(\cos^2\Phi + \sin^2\Phi\cos\Theta\right). \tag{4.7}$$

With the knowledge of

$$\sin\Phi = \frac{\omega_1}{\omega_{\text{eff}}} \tag{4.8}$$

$$\cos\Phi = \frac{\Delta\omega}{\omega_{\text{eff}}} \tag{4.9}$$

$$\Theta = \omega_{\text{eff}}\,\tau \tag{4.10}$$

Equations 4.5 - 4.7 become (Legchenko, 2004):

$$M_x = -\frac{\omega_1\Delta\omega}{\omega_{\text{eff}}^2}\left(1-\cos\left(\omega_{\text{eff}}\,\tau\right)\right)M_0 \tag{4.11}$$

$$M_y = \frac{\omega_1}{\omega_{\text{eff}}}\sin\left(\omega_{\text{eff}}\,\tau\right)M_0 \tag{4.12}$$

$$M_z = \frac{\Delta\omega^2 + \omega_1^2\cos\left(\omega_{\text{eff}}\,\tau\right)}{\omega_{\text{eff}}^2}M_0. \tag{4.13}$$

The transverse component $M_\perp$ of the spin magnetisation

$$M_\perp = M_y - \mathrm{i}M_x \tag{4.14}$$

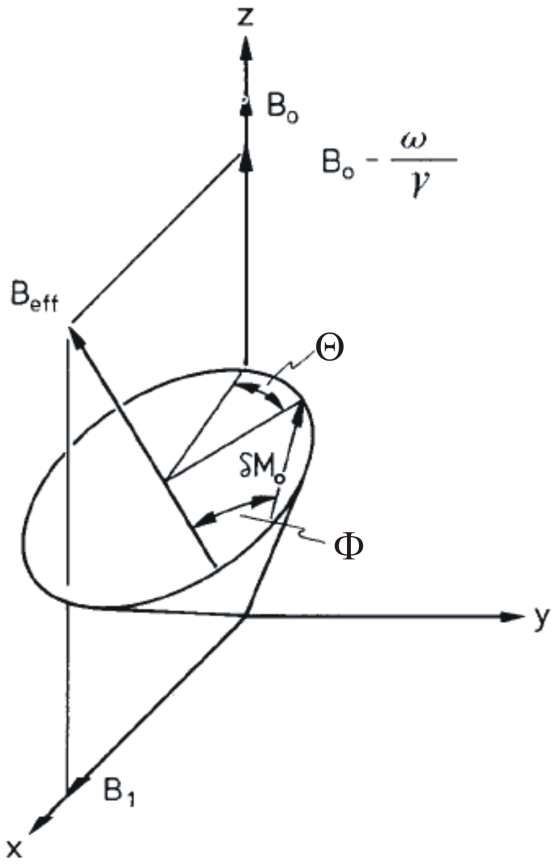

Figure 4.3.: Precession of spin magnetisation in the tilted rotating reference frame (Mansfield et al., 1979).

induces the magnetic resonance signal. Consequently, the kernel function (Eq. 3.29) becomes

$$K(q,\mathbf{r},\rho(V)) = \frac{2}{I_0}\omega_0(q)M_0\left|\mathbf{B}_T^-(\mathbf{r},\omega_0(q),\rho(V))\right| M_\perp(q,\mathbf{r})\cdot e^{i2\zeta_T(\mathbf{r},\omega_0(q),\rho(V))}. \tag{4.15}$$

In the following, the effect of the frequency deviation on the MRS sounding curve is studied using Equation 4.15.

Looking at Equations 4.11 and 4.12, it is obvious that the amplitude of the transverse magnetisation

$$|M_\perp| = \sqrt{M_y^2 + M_x^2} \tag{4.16}$$

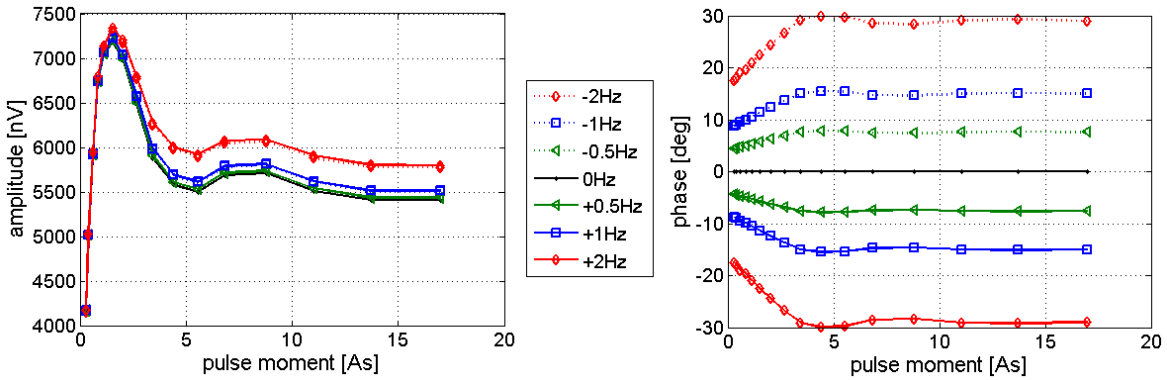

Figure 4.4.: Effect of the frequency deviation between the clock frequency ($f_{\mathrm{rf}} = 2086.8$ Hz) and the measured Larmor frequency f_0. Data are calculated assuming a constant frequency offset and a resistive subsurface (1E6 Ωm) using a circular loop ($d = 100$ m), 100 vol. % water content, 60°N inclination, pulse length $\tau = 40.3$ ms.

does not depend on the sign of the frequency deviation, assuming a resistive subsurface. Also, the amplitudes of the MRS sounding curve are independent from the sign of the frequency deviation, at least in the considered range of frequency deviations (±2 Hz). However, the phase values are anti-correlated to the sign of the frequency deviation, with respect to $\Delta f = f_0 - f_{\mathrm{rf}}$, i.e. a positive sign means that the actual measured Larmor frequency $f_0 = \omega_0/2\pi$ is larger than the clock frequency $f_{\mathrm{rf}} = \omega_{\mathrm{rf}}/2\pi$.

4.1.1. Synthetic data

Figure 4.4 shows the effect of a constant frequency deviation between -2 Hz and +2 Hz on the MRS amplitude and phase, assuming an insulating half-space. Figure 4.5 demonstrates the effect exemplary for two pulse moments. The amplitudes can be described with a power law and the phase values with a linear fit (Girard et al., 2005). However, the curvature of the amplitude curve and the gradient of the phases depends on the pulse moment. Therefore, it is necessary to include the frequency shift in the calculation of the kernel function rather than to correct the sounding curve itself.

The effect of the frequency deviation is also demonstrated for the kernel functions (Fig. 4.6). The amplitudes of the kernel function for constant frequency deviations of 1 Hz, 2 Hz and 3 Hz are compared to those of a conventional kernel function. They clearly show that the area of maximum amplitudes is broadened. This is due to the increased imaginary part even if the subsurface is an electrical isolator. And therefore, the depth focus is not so pronounced any more for increasing frequency deviation.

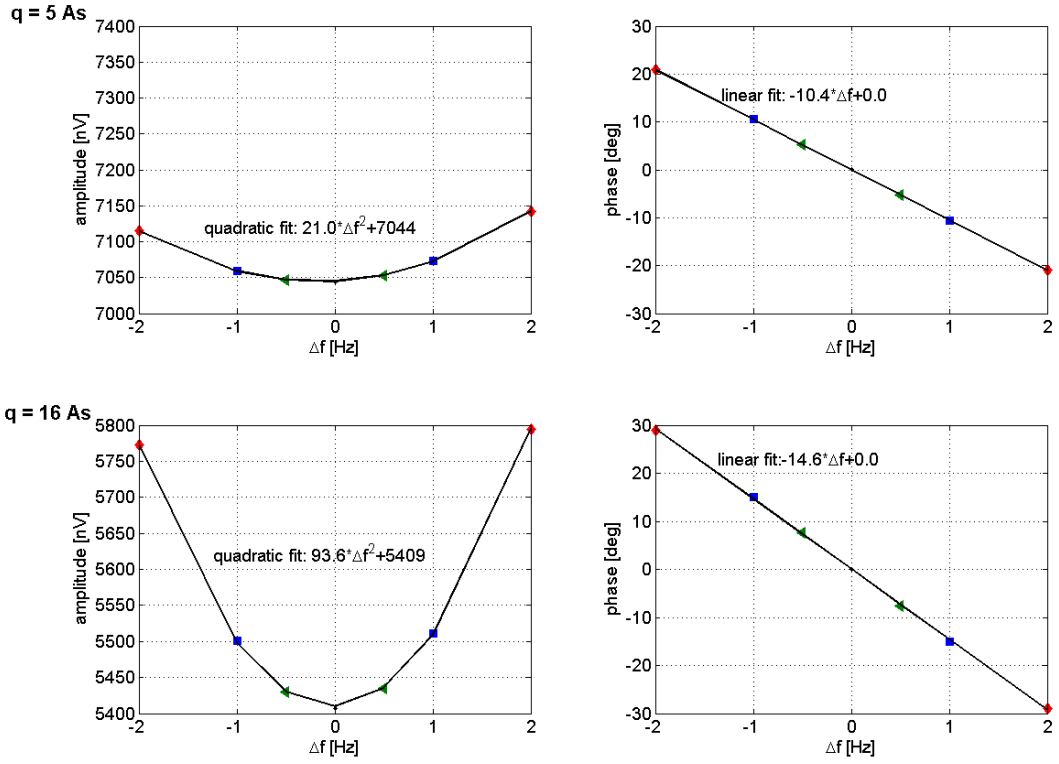

Figure 4.5.: Amplitude and phase values versus frequency offset, exemplary for two pulse moments. The amplitudes can be described with a power law and the phase values with a linear fit. Data are calculated assuming a constant frequency offset and a resistive subsurface (1E6 Ωm) using a circular loop (d = 100 m), 100 % water content, 60°N inclination, pulse length τ = 40.3 ms.

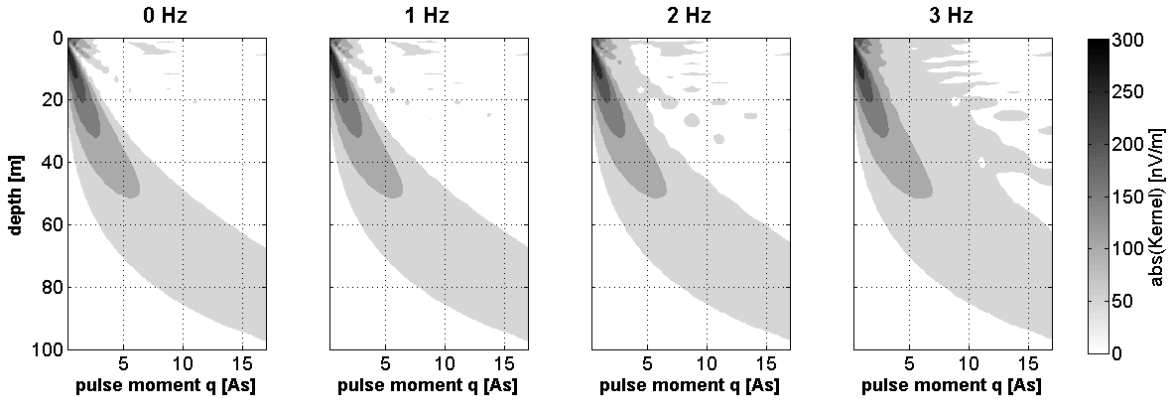

Figure 4.6.: Effect of the frequency deviation between the clock frequency ($f_{\mathrm{rf}} = 2086.8$ Hz) and the measured Larmor frequency f_0 on the 1D kernel function. Data are calculated assuming a constant frequency offset (0-3 Hz) and a resistive subsurface (1E6 Ωm) using a circular loop ($d = 100$ m), 100 % water content, 60°N inclination, pulse length $\tau = 40.3$ ms.

Finally, for a subsurface model with an aquifer between 25 and 50 m, inversions are conducted. The synthetic data are modelled considering frequency deviations of 1 Hz, 2 Hz and 3 Hz. The kernel function used for the inversion neglects the frequency deviation. Figure 4.7 shows the synthetic data as well as the inversion result. For increasing frequency deviation, the peak of the amplitude curve is broadened. Thus, the inversion result for the first layer is still correct. However, the thickness of the aquifer is overestimated but the water content is underestimated. Additionally, the water content of the underlying third layer is overestimated. The change of the inversion result is significant for a frequency deviation of more than 1 Hz.

The phase effects due to frequency variations are also important for smaller loop sizes. Figures A.1 and A.3 in the appendix show the corresponding sounding curves for a circular loop with $d = 50$ m and $d = 10$ m. Having a circular loop with $d = 50$ m or $d = 10$ m, the phase values are still in the same order as for a loop with $d = 100$ m, but they are shifted to smaller pulse moments, corresponding to the decreased penetration depth. However, the amplitudes decrease by a factor of four and ten, respectively. Contrary to the phase effects due to resistivity, the importance of the phase effects due to frequency variations remains the same independently from the loop size. This is demonstrated by the inversions shown in Figure A.2 and A.4.

Considering now an electrically conductive subsurface (Fig. A.5 and A.6 in the appendix), the amplitudes depend on the sign of the frequency deviation, too. They can be described with a power law, but they are asymmetric. This is due to the asymmetry

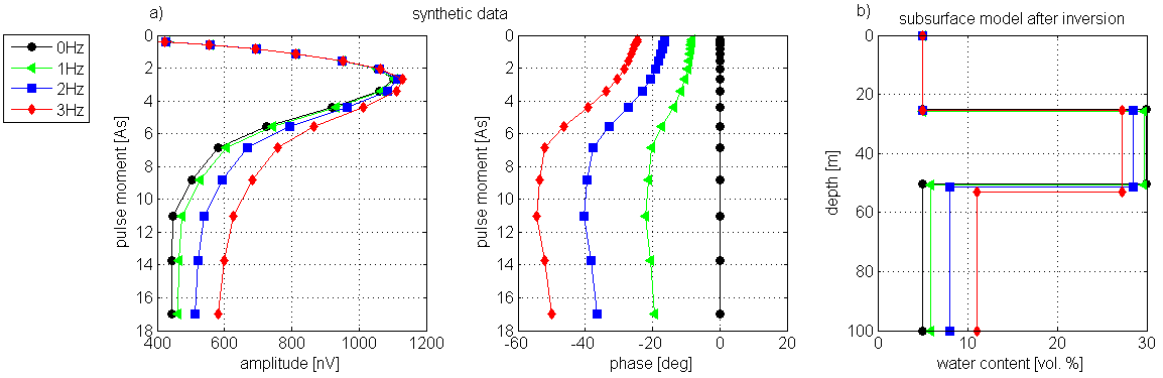

Figure 4.7.: Effect of the frequency deviation between the clock frequency (f_{rf} = 2086.8 Hz) and the measured Larmor frequency f_0 on the inversion result. a) Data are calculated assuming a constant frequency offset and a resistive subsurface (1E6 Ωm) using a circular loop (d = 100 m), 30 % water content between 25 and 50 m, 5 % in the surrounding, 60°N inclination, pulse length τ = 40.3 ms. b) Inversions are conducted neglecting the frequency deviation. Only the amplitude is used for the inversion.

of the amplitude of the co-rotating part $\left|\mathbf{B}_T^+\right|$ for conductive subsurfaces (Weichman et al., 2000; Braun et al., 2002). The linear behaviour of the phases remains, but the line is shifted by the amount of the phase caused by the resistivity.

The forward routine, presented in this section, is well tested with other routines available. Exemplary for the conductive subsurface, the calculated data with my own algorithm, part of the advanced program package Cossmo, is compared to those of the commercially available Numis program package MRS04_5.exe and Samogon (Fig. A.7 in the appendix). There are only slight differences due to numerical reasons.

The assessment of the phase effects due to frequency variations have shown that frequency offsets of more than 1 Hz significantly alter the MRS amplitude and phase. Neglecting these influences on the kernel function in the inversion yields an underestimated water content within the aquifer and an overestimated water content below the aquifer.

4.1.2. Field data

Furthermore we (Braun et al., 2003) verified the influence of the preset clock frequency under field conditions at the test site Nauen. The measurements were conducted directly one after the other with three clock frequencies: appropriate frequency (f_{rf} = 2088.8 Hz), too small frequency (f_{rf} = 2086.8 Hz) and too high frequency (f_{rf} = 2090.8 Hz). The pulse duration is τ_p = 40.3 ms.

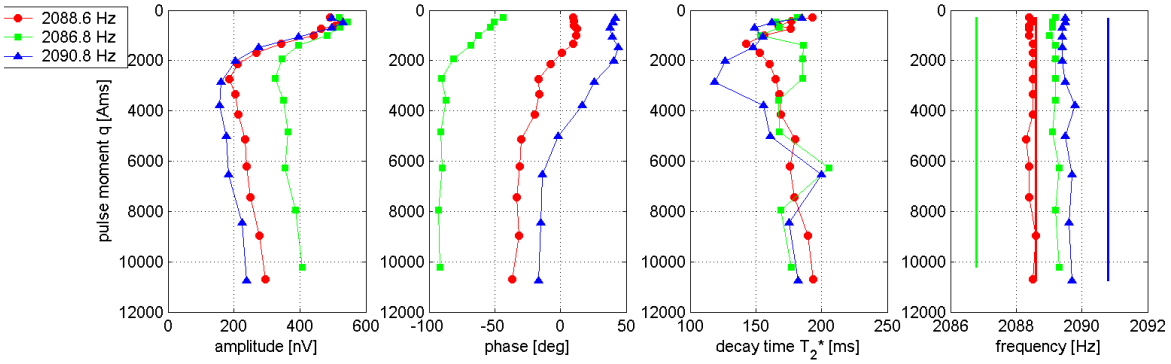

Figure 4.8.: Clock frequency test for figure-of-eight ($d = 50$ m) measurements, pulse duration $\tau_p = 40.3$ ms, test site Nauen.

The field results correspond to the synthetic analyses (Fig. 4.8). The recorded amplitudes are much higher if the clock frequency is preset too small. The deviation of clock frequency and Larmor frequency is smaller for the 2090.8 Hz case, so the effect of a too high frequency is smaller for the amplitude, but it is still prominent in the phase values. The decay times are not clearly affected by the clock frequency. However, the decay time curve for the appropriate frequency is much smoother, both other curves run even in opposite direction for small pulse moments.

In the following chapters, the effect of the frequency shift on MRS is neglected. In Chapter 6, synthetic data are used assuming ideal conditions. However, in Chapter 7 field data are used. Figure 4.9 and Figure 4.10 show the measured data, used in Chapter 7, along with the forward calculated data assuming ideal conditions ($\Delta f = 0$, red curve) and considering the measured frequency offset of each pulse moment (blue curve). The subsurface models are obtained from the MRS inversion with resistivity (see Figs. 7.4 and 7.7).

Due to the very small frequency offset (< 1 Hz) in the field case of France (Fig. 4.9), the frequency offset does not affect the amplitudes, it just affects slightly the phases and the imaginary part, respectively.

In the field case of Israel (Fig. 4.10), the very low resistivity has the main impact on the MRS signal. Thus, the frequency offset becomes apparent only at the last pulse moment.

The effect of the frequency shift on MRS should be estimated when analysing field data. The inversion scheme presented in Chapter 6 could be easily extended on considering the frequency shift when calculating the kernel function. However, this would require additional computation time.

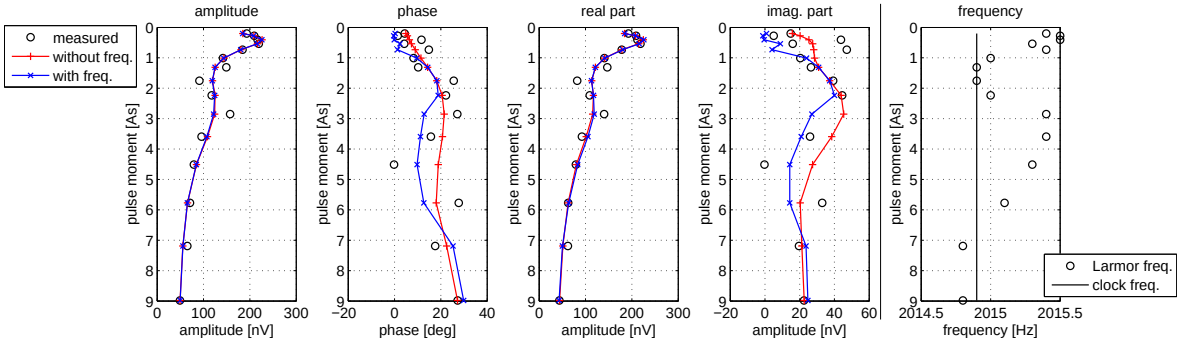

Figure 4.9.: MRS field data from the 1D area at the test site St-Cyr-en-Val (France) along with the forward calculated data assuming ideal conditions ($\Delta f = 0$, red curve) and considering the measured frequency offset (blue curve). The data are measured with a circular loop ($d = 48$ m, 2 turns). Magnetic field intensity 47324 nT, 63°N inclination. Subsurface model (see Fig. 7.4b): Layer 1 (0 - 6.5 m): 4 vol.%, 14 Ωm; Layer 2 (6.5 - 20.2 m): 10 vol.%, 30 Ωm; Layer 3 (20.2 - 27.1 m): 0.0 vol.%, 6 Ωm; Layer 4 (27.1 - 36 m): 14 %, 28 Ωm; Layer 5 (36 m-?): 0.0 vol.%, 17 Ωm.

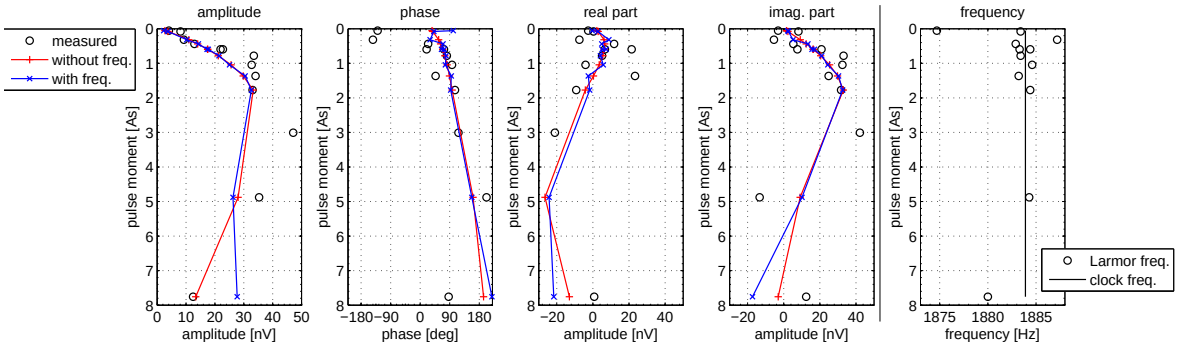

Figure 4.10.: MRS field data at station MRS 6 from Israel along with the forward calculated data assuming ideal conditions ($\Delta f = 0$, red curve) and considering the measured frequency offset (blue curve). The data are measured with a 100 x 100 m^2 square loop. Magnetic field intensity 44247 nT and 30°N inclination. Subsurface model (see Fig. 7.7b): Layer 1 (0 - 6.5m): 4 vol.%, 14 Ωm; Layer 2 (6.5 - 20.2m): 10 vol.%, 30 Ωm; Layer 3 (20.2 - 27.1m): 0.0 vol.%, 6 Ωm; Layer 4 (27.1 - 36m): 14 %, 28 Ωm; Layer 5 (36m - ?): 0.0 vol.%, 17 Ωm.

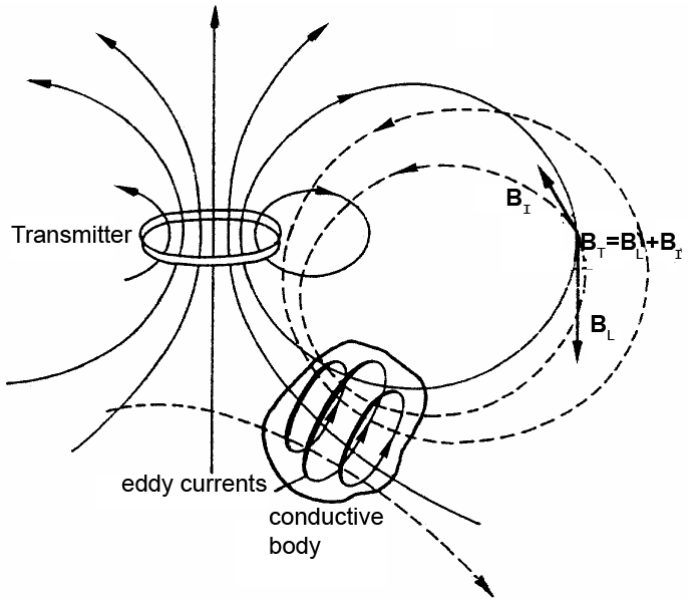

Figure 4.11.: The excitation field $\mathbf{B}_T = \mathbf{B}_L + \mathbf{B}_I$ is the superposition of the transmitted loop field $\mathbf{B}_L$ and the induced field $\mathbf{B}_I$ due to a conductive body (adapted from Militzer and Weber (1985)).

4.2. Effect of 1D resistivity on MRS

4.2.1. The magnetic excitation field

To understand the effect of the resistivity on MRS, it is necessary to study the effect of the resistivity on the electromagnetic field, that is induced in the subsurface. The transmitter loop generates a magnetic field $\mathbf{B}_L$. In a conductive body eddy currents are produced, that induce the field $\mathbf{B}_I$. The effective excitation field is the vectorial superposition $\mathbf{B}_T$=$\mathbf{B}_L + \mathbf{B}_I$ (Fig. 4.11).

Figure 4.12 shows the norm of the magnetic field of the excitation field

$$B_{norm} = \sqrt{|\mathbf{B}_r|^2 + |\mathbf{B}_z|^2}, \tag{4.17}$$

where $\mathbf{B}_r$ is the radial component and $\mathbf{B}_z$ is the vertical component of the magnetic field. The electromagnetic skin depth δ describes the distance, where a plane wave will be reduced by a factor of $1/e$, i.e. by 37 % (Ward and Hohmann, 1988)

$$\delta = \sqrt{\frac{2\rho}{\omega\mu}}, \tag{4.18}$$

where ρ is the half-space resistivity, $\omega = 2\pi f$ the angular frequency and μ the magnetic permeability. Hence, the skin depth depends on the resistivity as well as on the frequency. For $\mu = \mu_0 = 4\pi \cdot 10^{-7} \frac{\mathrm{Vs}}{\mathrm{Am}}$ in vacuum, Equation 4.18 becomes

$$\delta[\mathrm{m}] = 503\sqrt{\frac{\rho[\Omega\mathrm{m}]}{f\,[\mathrm{Hz}]}}. \tag{4.19}$$

The MRS method uses a loop as an active source with a low frequency (0.8-3 kHz). Thus, there is also a geometrical attenuation dependent on the inhomogeneity in horizontal direction: the more the field is inhomogeneous in horizontal direction, the more the field is attenuated in vertical direction (Weidelt, 2005).

In Figure 4.12 the norm of the magnetic excitation field at the loop centre and the skin depth are depicted for various resistivities of a homogeneous half-space (1, 10, 100, 1000, 10000 Ωm) and for various loop diameters (10, 50, 100 m). The skin depths are drawn as coloured encoded lines; they do not depend on the loop diameters. The vertical axis limit is five times the loop diameter. Due to the geometrical attenuation, the magnetic field rapidly decreases even for a quasi insulating half-space (10000 Ωm). The correlation between the influence of the resistivity on the magnetic field and the skin depth is immediately obvious: having a resistivity with a skin depth greater than one loop diameter, this resistivity does not affect the magnetic field. The effect of the resistivity is the strongest for a large loop ($d = 100$ m) and resistivities smaller than 100 Ωm. The magnetic field decreases the most for a small loop ($d = 10$ m). The resistivity effect decreases for decreasing loop size; it is shifted to resistivities smaller than the geologically relevant lower limit of 1 Ωm for a loop with $d = 10$ m.

The magnetic fields are calculated for a current of $I = 1$ A in the loop. The currently upper limit of the Numis system is $I = 450$ A, corresponding to a pulse moment $q = 0.04\,\mathrm{s} \cdot 450\,\mathrm{A} = 18\,\mathrm{As}$ for a pulse length $\tau = 0.04\,\mathrm{s}$. The magnetic field increases linearly with the actual current used. The principal curve shape remains the same, but the absolute values increase by the factor of the actual current.

4.2.2. MRS sounding curves

Now the effect of the resistivity is studied on the MRS curve. Figure 4.13 shows MRS calibration sounding curves (100 vol.% water content) for several resistivities (1, 10, 100, 1000, 10000 Ωm) and various loop sizes ($d = 100$ m, 50 m, 10 m). The number of loop turns (1 turn and 2 turns) is varied for a loop size of $d = 50$ m. The phase values

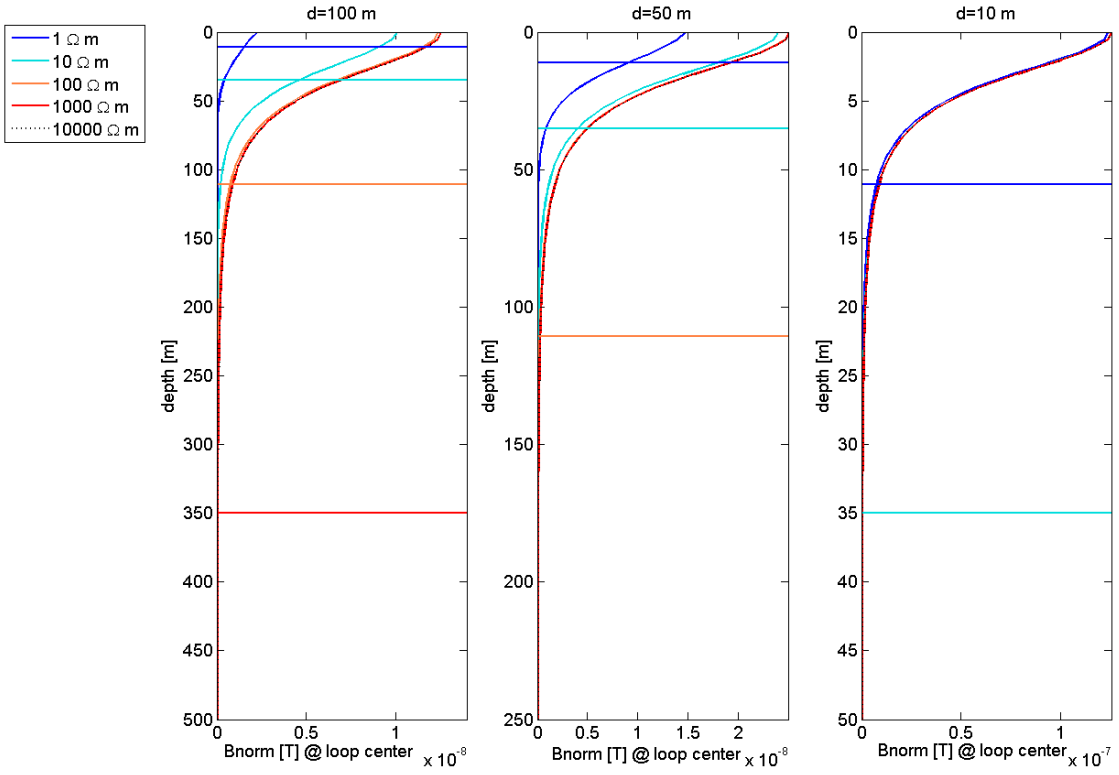

Figure 4.12.: Norm B_{norm} of the magnetic field at the loop centre versus depth for several resistivities of a homogeneous half-space between 1 and 10000 Ωm compared to the corresponding electromagnetic skin depths drawn as line in the same colour. The data are calculated using a current of $I = 1$ A and a magnetic field intensity of 48000 nT (corresponding to $f = 2043$ Hz). The circular loops have diameters of $d = 100$ m, $d = 50$ m and $d = 10$ m.

are corrected to produce a smoother phase plot; multiples of 360° are added in case of absolute jumps in the phase greater than 180°.

The effect of the resistivity is strongest for a loop of $d = 100$ m. There is still an impact on the sounding curve up to a resistivity greater than 1000 Ωm. For a loop of $d = 10$ m, resistivities greater than 100 Ωm do not affect the sounding curve. As it can be seen for a loop of $d = 50$ m, the impact of the resistivity depends also on the numbers of turns. The penetration volume is increased having a greater number of turns and therefore, the resistivity impact increases, too. Doubling the number of turns results in a doubled effective pulse moment. In this synthetic study, the pulse moment vector remains the same for all loop configurations. However, under field conditions, the maximum pulse moment decreases for a greater number of turns due to the changed loop impedance.

The resistivity effect is stronger than expected by the norm of the magnetic field (Figure 4.12). This can be explained by the increased value of the current and by the increased volume that is considered in the calculation of the MRS curve.

4.2.3. MRS kernel function and estimation of the penetration depth

Exemplary for a loop with $d = 100$ m, Figure 4.14 shows contour plots of the amplitude of the 1D MRS kernel function for several resistivities of a homogeneous half-space between 1 and 10000 Ωm. The contour plots demonstrate the increased penetration depth with increasing pulse moment. However, the penetration depth also depends on the resistivity of the subsurface due to the electromagnetic attenuation. The penetration depth is approximately 25 m having a homogeneous half-space of 1 Ωm and about 100 m for the quasi insulating case (10000 Ωm).

Rearranging the 1D kernel function for various half-space resistivities yields Figure 4.15. For a maximum pulse moment of 18 As, the 1D kernel function is displayed versus resistivity.

In addition, Figure 4.16 shows the dependency of the penetration depth on the resistivity for various pulse moments. Each plot of the figure represents an image of the amplitude of the 1D kernel function calculated for various resistivities between 1 and 1000 Ωm. The respective pulse moment is indicated in the title of each plot of the figure. The penetration depth increases linearly with the logarithmic of the resistivity until an upper limit of approximately 200 Ωm for a loop with $d = 100$ m. However, the penetration depth does not depend on the resistivity for smaller pulse moments. Anal-

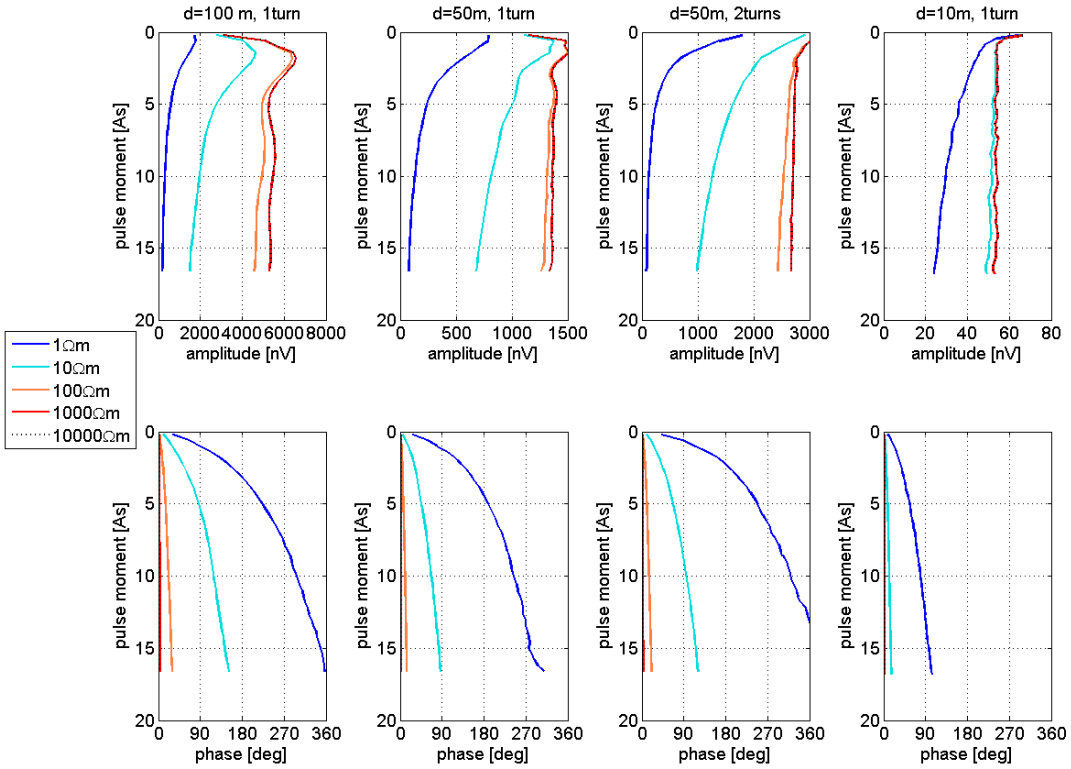

Figure 4.13.: MRS calibration soundings (100 vol.% water content) for several resistivities of an homogeneous half-space between 1 and 10000 Ωm. The data are calculated using circular loops (d = 100 m; d = 50 m; d = 50 m, 2 turns; d = 10 m) and magnetic field intensity of 48000 nT and 60°N inclination.

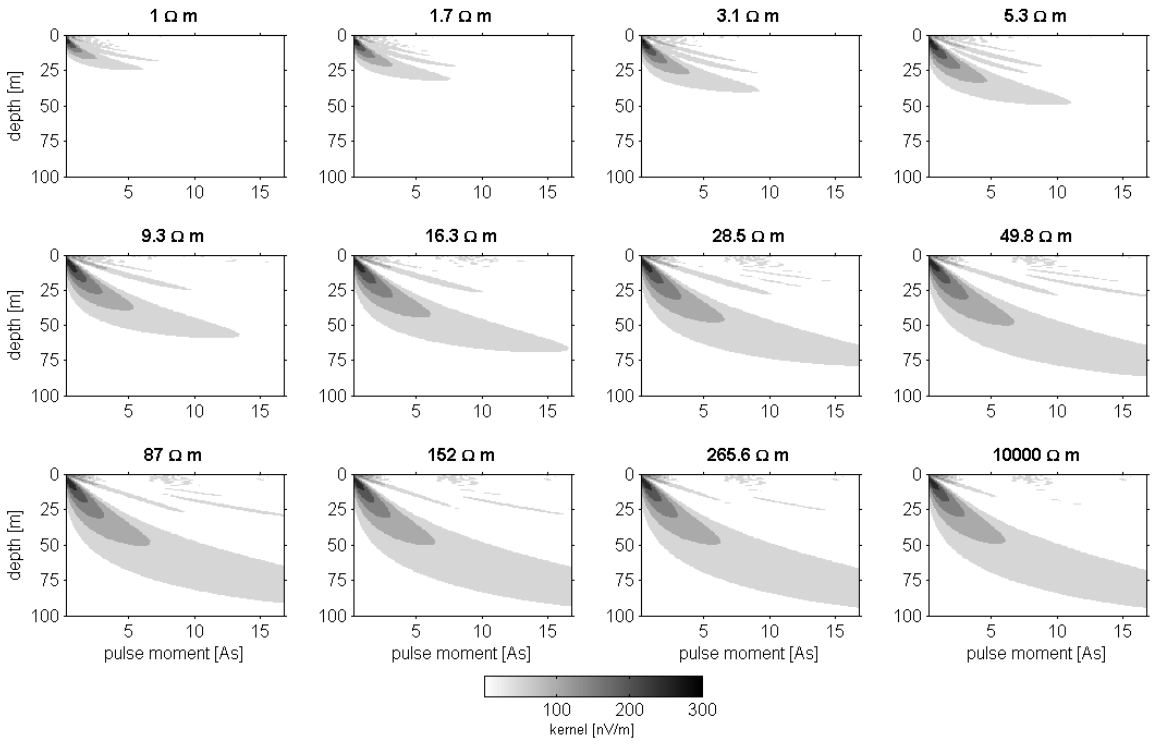

Figure 4.14.: Contour plots of the amplitude of the 1D MRS kernel function for several resistivities of a homogeneous half-space between 1 and 10000 Ωm (shown in the title of each plot). The data are calculated using a circular loop ($d =$ 100 m) and a magnetic field intensity of 48000 nT and 60°N inclination.

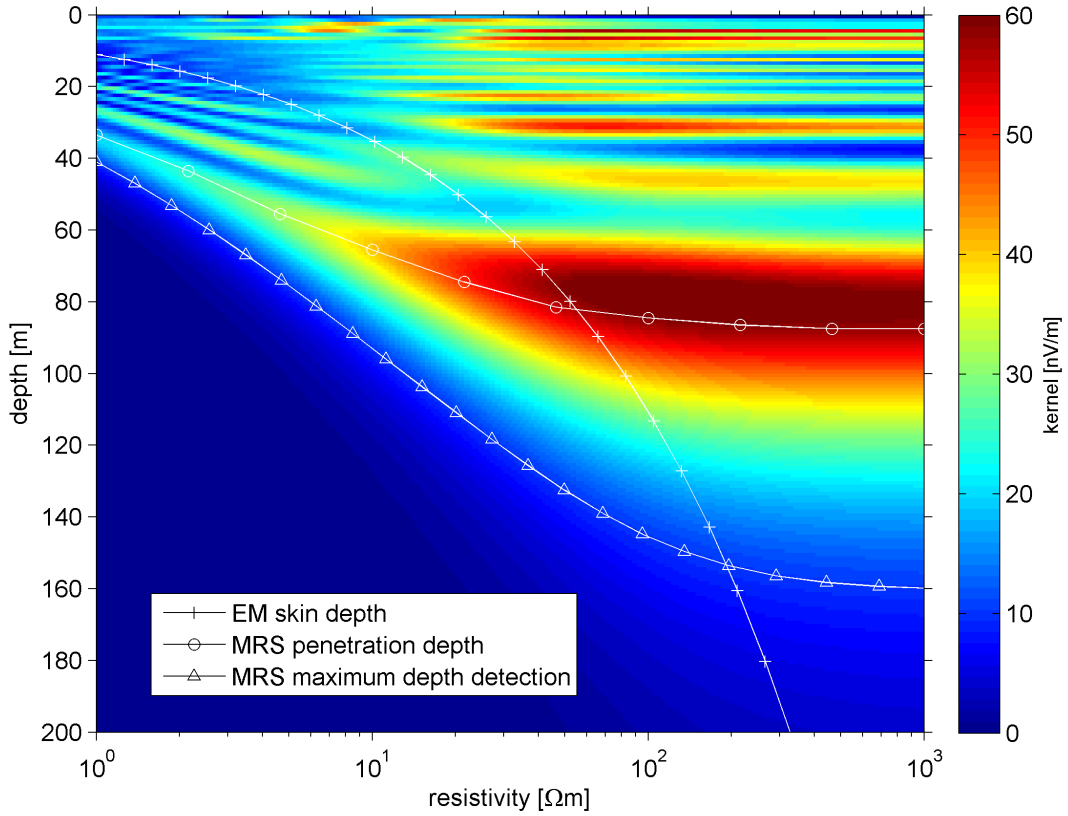

Figure 4.15.: Image of the amplitude of the 1D MRS kernel function of a pulse moment $q = 18$ As for homogeneous half-spaces with resistivities between 1 and 1000 Ωm. The calculated electromagnetic skin depth, MRS penetration depth and MRS maximum detection depth are superimposed.

ogous figures for loop diameters of $d = 50$ m (1 turn and 2 turns) as well as $d = 10$ m are in the appendix (Figs. B.1 - B.3).

Several ways have been presented in order to calculate the MRS penetration depth. Legchenko and Shushakov (1998) and Legchenko et al. (2002) define the maximum depth detection as the depth of the top of a 1 m thick water layer (100 vol.% water) that gives an MRS signal over a threshold value of 10 nV.

Vouillamoz et al. (2007) estimate the MRS penetration depth up to a depth limit of one loop size by the electromagnetic skin depth $\delta = 503\sqrt{\rho/f}$, where ρ is the half-space resistivity and f is the frequency. The electromagnetic skin depth δ describes the distance, where a plane wave will be reduced by a factor of $1/e$, i.e. it falls to 37 % of its original value. However, the MRS method uses a loop as an active source. Thus, there is also a geometrical attenuation dependent on the inhomogeneity in horizontal direction: the more the field is inhomogeneous in horizontal direction, the more the field is attenuated in vertical direction (Weidelt, 2005).

Müller-Petke et al. (2007) calculate the MRS penetration depth using the singular value decomposition (SVD) approach.

In Figure 4.15 the three approaches of the estimation of the MRS penetration depth are superimposed on the image of the 1D kernel function versus depth and homogeneous half-space resistivity. It is clearly visible that an estimation via the skin depth is not useful for MRS application, not even for depths smaller than one loop size. However, the intersection point of the EM skin depth and the MRS maximum depth detection can be used to estimate the maximum effective resistivity, i.e. resistivity above this value of approximately 200 Ωm can be neglected. This cut-off value depends on loop size and pulse moment. The maximum effective resistivity is studied in detail in Section 6.2.1.

The MRS maximum depth detection follows the contour line of 10 nV/m. Below this depth limit, the water content does not contribute to the measured MRS signal. This is the depth down to which the kernel function should be calculated when inverting the data.

The MRS penetration depth using the SVD approach follows approximately the maximum sensitivity. This can be regarded as confidence depth limit down to which the inversion can give a reliable result.

Further studies on the MRS penetration depth depending on loop size and resistivity are presented in Müller et al. (2006) and Hertrich et al. (2006).

It is necessary to point out that the MRS penetration depth depends on various parameters such as loop size, number of turns, resistivity structure of the subsurface, earth's

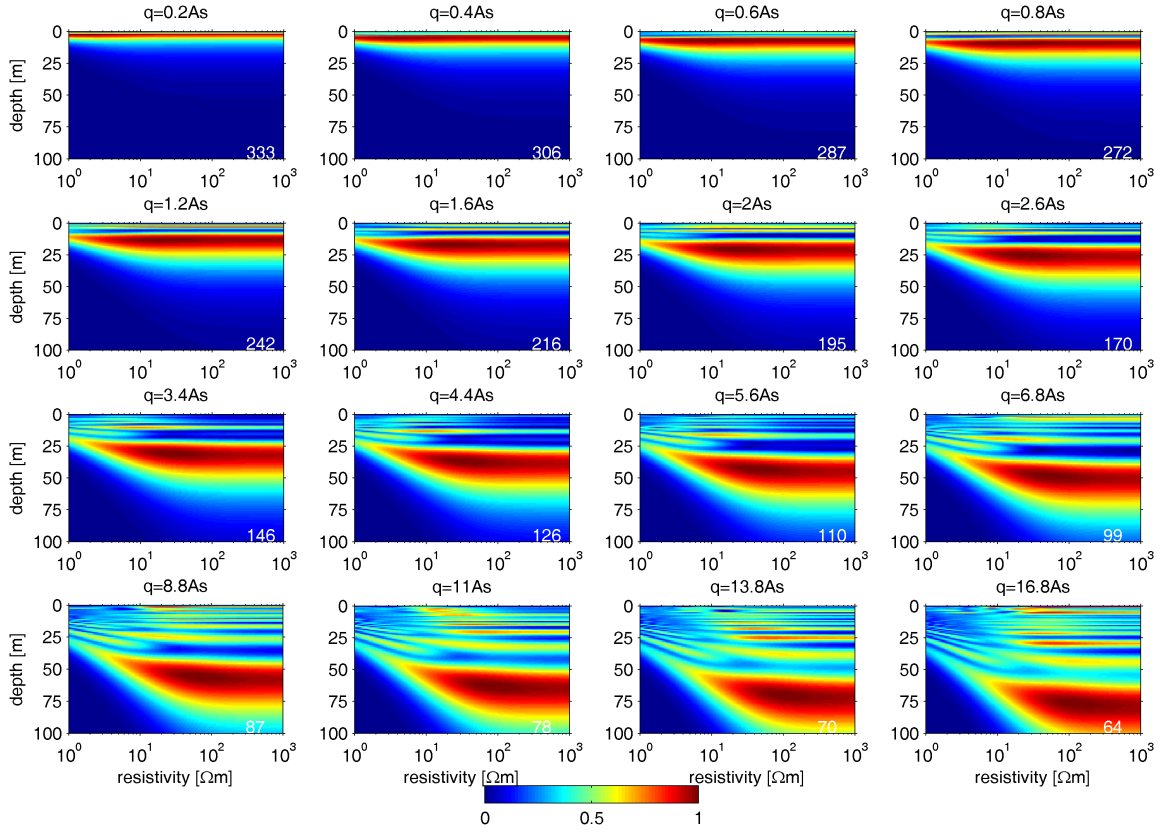

Figure 4.16.: Homogeneous half-space - Image of the amplitude of the 1D MRS kernel function of selective pulse moments for homogeneous half-spaces with resistivities between 1 and 1000 Ωm. The amplitudes are normalised on their maximum value [nV/m], that is indicated in the lower right corner of each plot. The data are calculated using a circular loop ($d = 100$ m) and magnetic field intensity of 48000 nT and 60°N inclination.

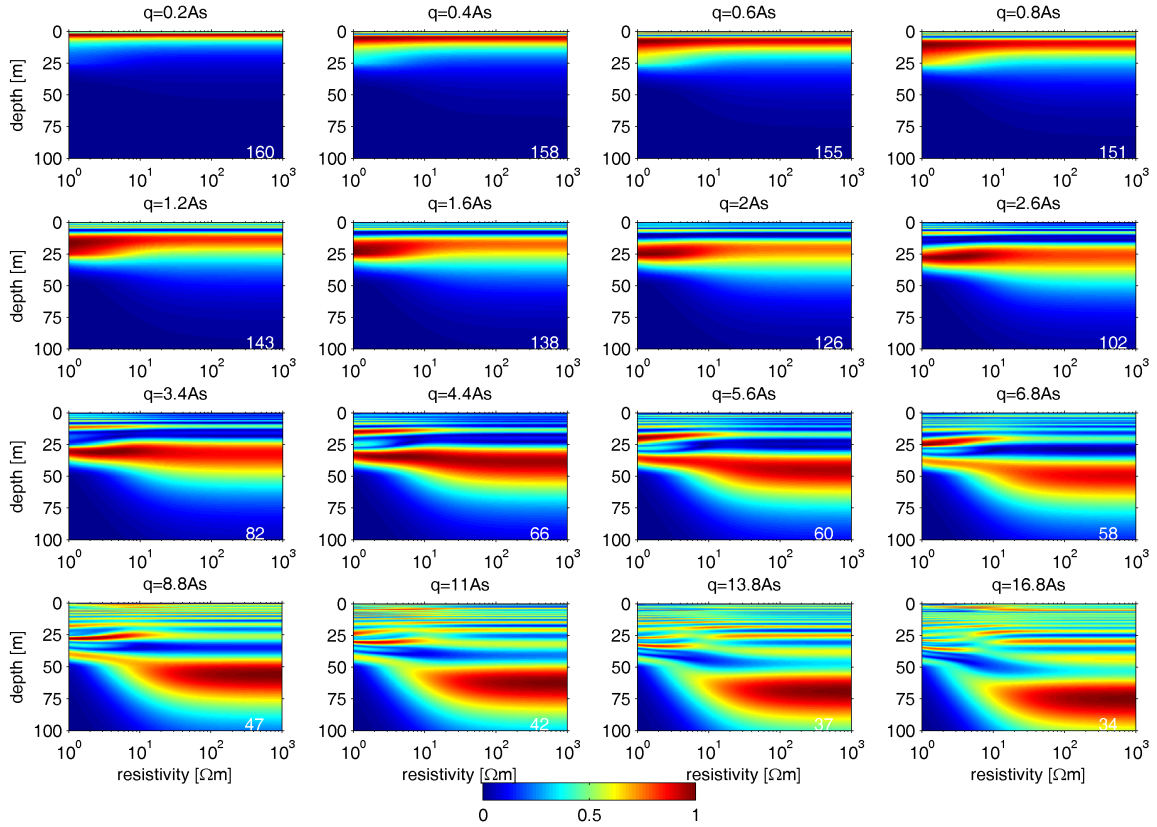

Figure 4.17.: 3-layer model - Image of the amplitude of the 1D MRS kernel function of selective pulse moments for a 3-layer model with resistivities of 50 Ωm of the 1st and 3rd layer and resistivities between 1 and 1000 Ωm of the 2nd layer between 25-50 m. The amplitudes are normalised on their maximum value [nV/m], that is indicated in the lower right corner of each plot. The data are calculated using a circular loop ($d = 100$ m) and magnetic field intensity of 48000 nT and 60°N inclination.

magnetic field strength and inclination. Therefore, the MRS penetration depth must be calculated for each site using the appropriate kernel function.

Figure 4.17 shows analogously to Figure 4.16 the image of the 1D MRS kernel function, but now for a 3-layer model: The resistivity of the first and third layer is 50 Ωm, whereas the resistivity of the second layer between 25 and 50 m is varied in a range of 1 to 10000 Ωm. The corresponding figures of the MRS sounding curves (100 vol.% water content as well as realistic water content) and of the contour plots of the 1D MRS kernel function for various resistivities of the second layer are shown in the appendix (Figs. B.4 and B.5).

In Figure 4.17 it is clearly visible that an increase of the resistivity of a deeper layer yields an increase of the penetration depth if the focus depth is smaller than the low resistive layer, i.e. for pulse moments smaller than 2 As for the given configuration. However, if the focus depth is within the low resistive layer, the penetration depth is decreased. Having a very low resistive layer (1 Ωm), the penetration depth is limited by this layer even for the maximum possible pulse moment.

In this section I have shown the influence of the resistivity of homogeneous as well as layered subsurface on MRS for loop sizes of $d = 100$ m, $d = 50$ m and $d = 10$ m. The resistivity effect is more prominent for greater loop sizes and for greater pulse moments.

4.2.4. Effect of neglecting the resistivity in the inversion

Figure 4.18 shows the importance of the resistivity in the subsurface with synthetic data (Braun and Yaramanci, 2003). The MRS signals were calculated for a quasi-insulating (10000 Ωm) and for electrically conductive half-spaces with resistivities of 100 Ωm, 50 Ωm, 10 Ωm, and 1 Ωm, but they were inverted using the insulating kernel in order to estimate the error in determining the water content caused by the non-consideration of the resistivity in the subsurface. The model grid is 0.5 m with a maximum depth of 200 m. The maximum inversion depth is 100 m, the water content between 100 m and 200 m is set to 5 vol.%. The data were modelled with a water content of 30 vol.% between 20 and 45 m and 5 vol.% elsewhere. Figure 4.18a displays the amplitudes of the respective kernel function. The second row (Fig. 4.18b) presents the modelled and fitted MRS amplitudes with the data misfit as relative rms error in percent, and the third row (Fig. 4.18c) shows the modelled and the inverted water content with the model misfit as rms error.

In Figure 4.18 the subsurface is an electrically homogeneous half-space. The MRS amplitudes decrease with decreasing resistivity. Since the values of the kernel function

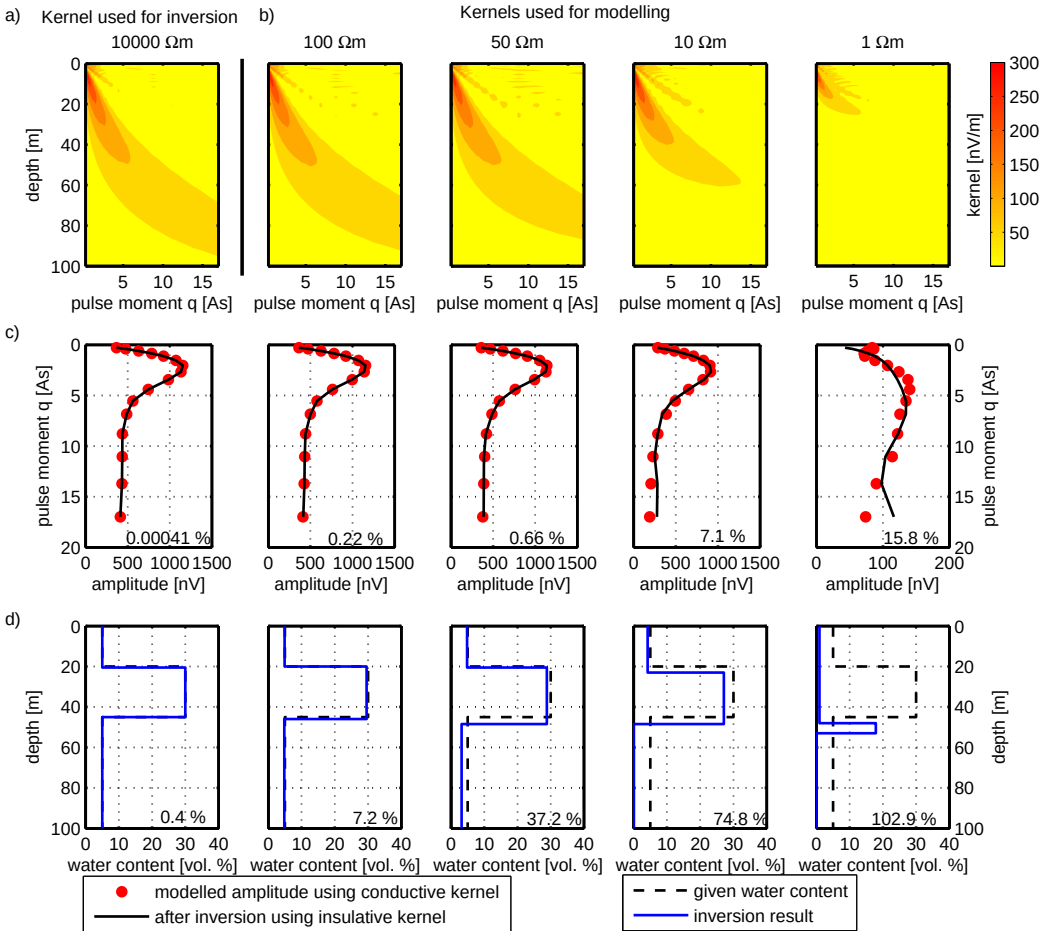

Figure 4.18.: Homogeneous half space, circular loop ($d = 100$ m), earth's magnetic field 48000 nT, inclination 60°N. Amplitudes were modelled for electrically conductive half space, but they were inverted using an insulating half space.

decrease with increasing depth, the inversion algorithm shifts the aquifer down and calculates lower water contents.

Not considering the resistivity of the subsurface in the inversion yields a biased water content distribution. The subsurface with resistivities higher than 100 Ωm can be regarded as insulating using a loop size of 100 m. As it will been shown in Section 6.2.1, this cut-off value depends on the loop size.

5. Evaluation of the influence of 2D resistivity on MRS

Previously, the MRS technique has been used as pure depth sounding method, and so the influence of the resistivity has been considered only for laterally stratified subsurface, i.e. 1D conditions, changes are allowed only in depth direction. Nowadays, MRS is also used to investigate 2D water content distributions, i.e. changes of the water content are allowed in depth and in one lateral direction (Hertrich, 2005; Hertrich et al., 2005b,a; Rommel et al., 2006; Rommel, 2006; Yaramanci and Hertrich, 2006). However, the resistivity is still considered as 1D or as homogeneous half space. But, generally, a change in the water content also affects a variation in the resistivity. Therefore, also the resistivity should be taken into account as 2D or even 3D.

5.1. Calculation of the excitation magnetic field

The main task when computing the kernel function is the calculation of the applied external magnetic field of the transmitter loop, which depends also on the resistivity of the subsurface.

In case of an electrically homogeneous or horizontally stratified subsurface, the excitation magnetic field of a circular loop is radially symmetric and can be analytically calculated. However, I consider the electromagnetic field over a 2D or 3D resistivity structure and use COMSOL Multiphysics as a commercially available finite element algorithm to calculate the excitation magnetic field numerically.

I show the modelling procedure exemplary for an electrically homogeneous subsurface and for a 2D structure of a discontinuous layer. For the calculations I used the Electromagnetics Module, 3D quasi-static case with a frequency of 2043 Hz (COMSOL, 2005). This resonance frequency corresponds to a magnitude of the earth's magnetic field of 48000 nT.

Figure 5.1 shows slices and isosurfaces of the calculated magnitude B_{norm} of the excitation field

$$B_{norm} = \sqrt{|\mathbf{B}_x|^2 + |\mathbf{B}_y|^2 + |\mathbf{B}_z|^2}, \tag{5.1}$$

where $\mathbf{B}_x$, $\mathbf{B}_y$ and $\mathbf{B}_z$ are the x-, y-, and z- component of the excitation magnetic field of the transmitter loop. The loop is placed on the x-y plane for $z = 0$ m, which is defined as the earth's surface. For the numerical calculation also the air-half space has to be considered for $z > 0$ m with an electrical conductivity of 0 S/m.

Figure 5.1 shows the excitation field for an electrical homogeneous subsurface with 50 Ωm. The isosurfaces show clearly the axis-symmetry. For an electric insulator the isosurfaces would be even spherical shells.

Now considering a discontinuous layer (25 m deep, 25 m thick) in the subsurface with a lower resistivity (5 Ωm), the excitation field is distorted (Figure 5.2), and there is no symmetry any more. The attenuation due to the low resistive body can be clearly seen (Braun et al., 2005b). The distortion due to the conductive body propagates also into the air-half space.

5.2. 2D models

The influence of a 2D resistivity are studied using geological scenarios of a discontinuous layer, a dipping layer and blocks with varying widths. The case of a discontinuous layer is studied in very detail including a change of the geographical location as well as layer depth and resistivity. All the data are calculated for a coincident receiver and transmitter loop with a diameter of $d = 100$ m. The earth's magnetic field is taken as 48000 nT, 60°N inclination.

5.2.1. Discontinuous layer

The 3D kernel function can be calculated for a given excitation field. Figure 5.3 shows slices and isosurfaces of the amplitude of the complex valued 3D kernel function for a pulse moment of q =1.1 As corresponding to the excitation field shown in Figure 5.2. The distortion of the excitation field due to the low resistive discontinuous layer affects also the kernel function. Therefore, the affected volume decreases in vertical and lateral direction around the low resistive discontinuous layer.

Since I consider a subsurface structure that changes only in two directions (x and z), the kernel function can be integrated over the third direction (y). Figures 5.4 and 5.5

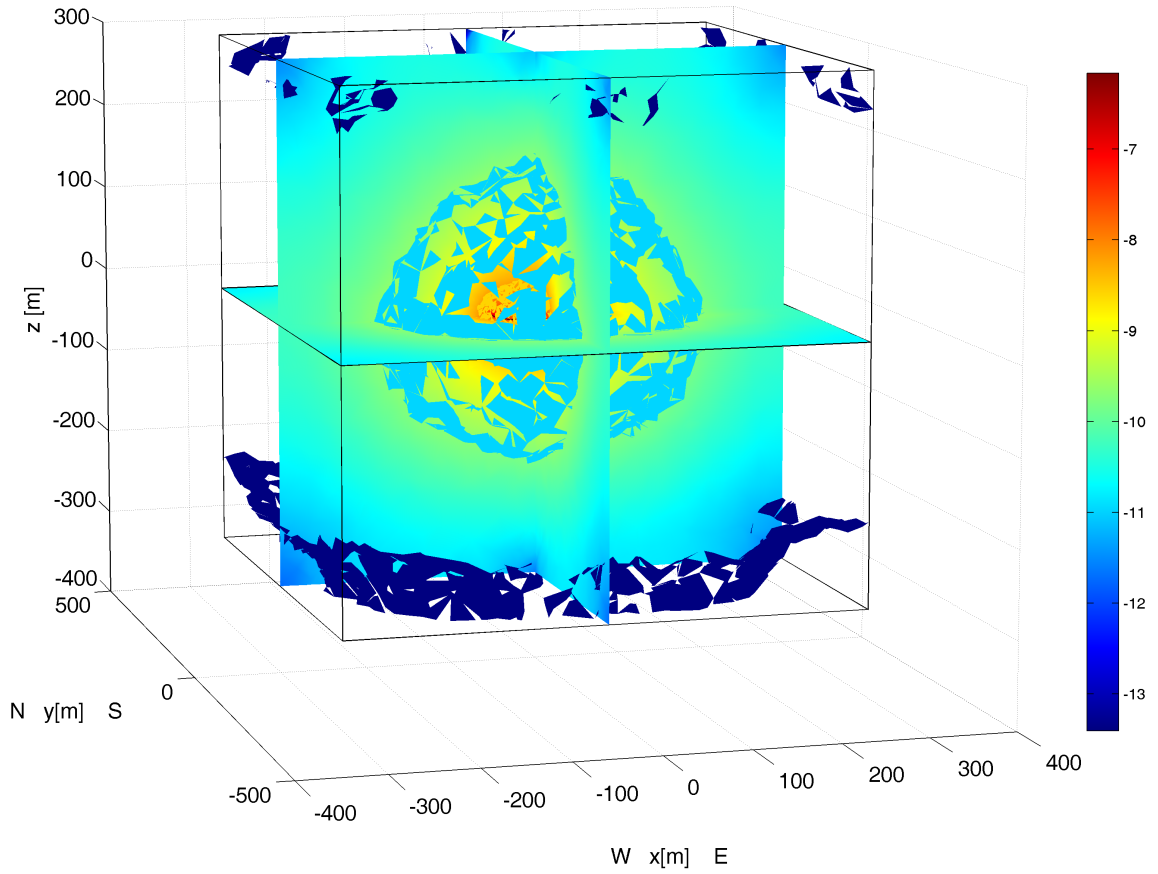

Figure 5.1.: Magnitude $\log_{10}(B_{norm})$ of the transmitted magnetic field of a circular loop ($d = 100$ m, loop centre at the origin of the coordinate system) using $f = 2043$ Hz. Electrical conductivity of the air half-space ($z > 0$ m) is 0 S/m. The subsurface ($z < 0$ m) is electrically homogeneous with 50 Ωm.

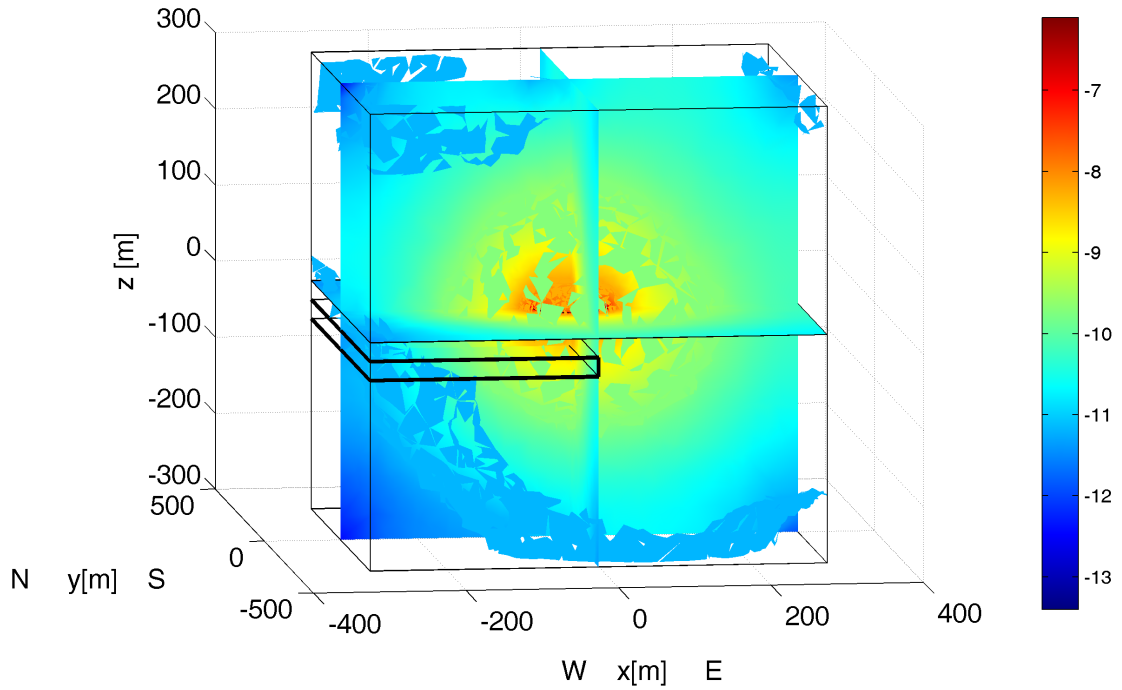

Figure 5.2.: Magnitude $\log_{10}(B_{norm})$ of the transmitted magnetic field of a circular loop ($d = 100$ m, loop centre at origin of the coordinate system) using 2043 Hz. Electrical conductivity of the air half-space ($z > 0$ m) is 0 S/m. The subsurface consists of a 25 m thick discontinuous layer at 25 m depth with 5 Ωm in a surrounding of 50 Ωm.

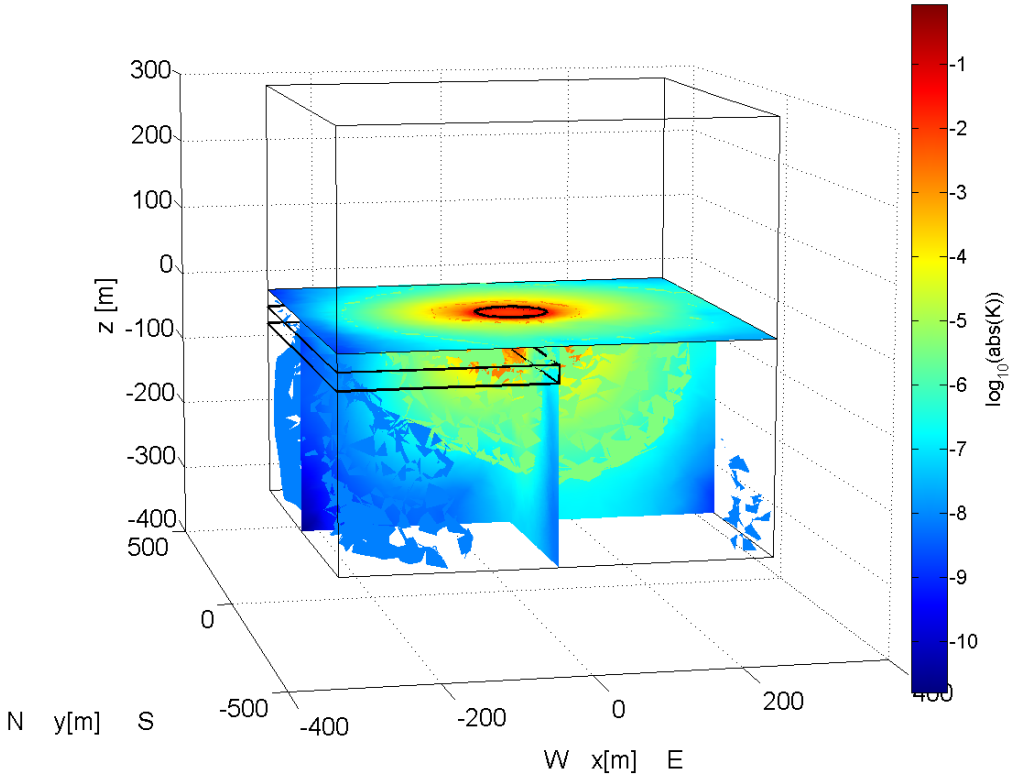

Figure 5.3.: Amplitude of the 3D kernel function for a pulse moment of q =1.1 As using a circular loop (d = 100 m, loop centre at the origin of the coordinate system) with f = 2043 Hz. Electrical conductivity of the subsurface ($z <$ 0 m) is 5 Ωm for the discontinuous layer and 50 Ωm for the surrounding. The earth's magnetic field is taken as 48000 nT, 60°N inclination.

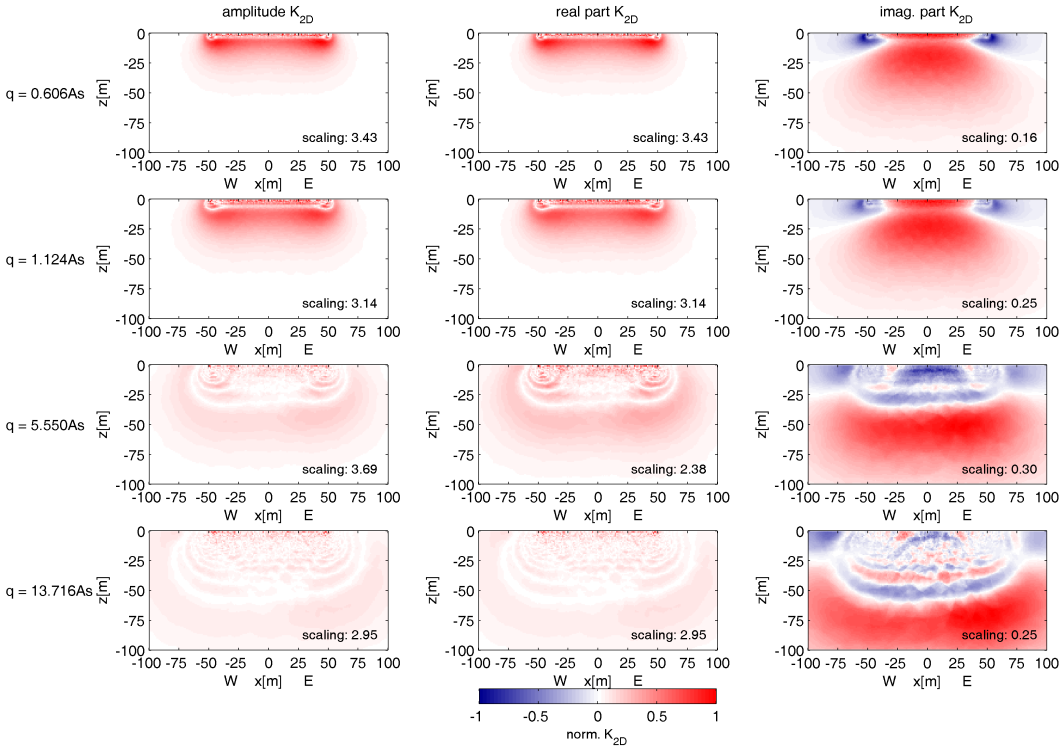

Figure 5.4.: Homogeneous half-space - 2D kernel function for selected pulse moments using a circular loop (d = 100 m, loop centre at origin of the coordinate system). The data are normalised on their maximum value [nV/m^2] as indicated the lower right corner of each plot of the figure. Electrically homogeneous subsurface with a resistivity of 50 Ωm. The earth's magnetic field is taken as 48000 nT, 60°N inclination.

show amplitude, real and imaginary part of the 2D kernel function for selected pulse moments (see Eq. 3.30). The 2D kernel function is normalised by their maximum value, which is indicated in each plot of the figure. The 2D kernel function for an electrically homogeneous subsurface (Figure 5.4) demonstrates the increasing penetration depth for increasing pulse moments. They are slightly distorted in the shown west-east direction due to the electrical conductive subsurface (Weichman et al., 2000).

Additionally to the 3D kernel function shown for one pulse moment in Figure 5.3, the 2D kernel function for four selected pulse moments is depicted in Figure 5.5 considering a low resistive discontinuous layer in a depth of 25 m and 25 m thickness. The low resistive body affects especially the imaginary part of the kernel function. The kernel function is distorted below and above the body as well as in the near vicinity in the lateral direction. The distortion decreases for increasing lateral distances. The distortion in the real part is less visible but still significant.

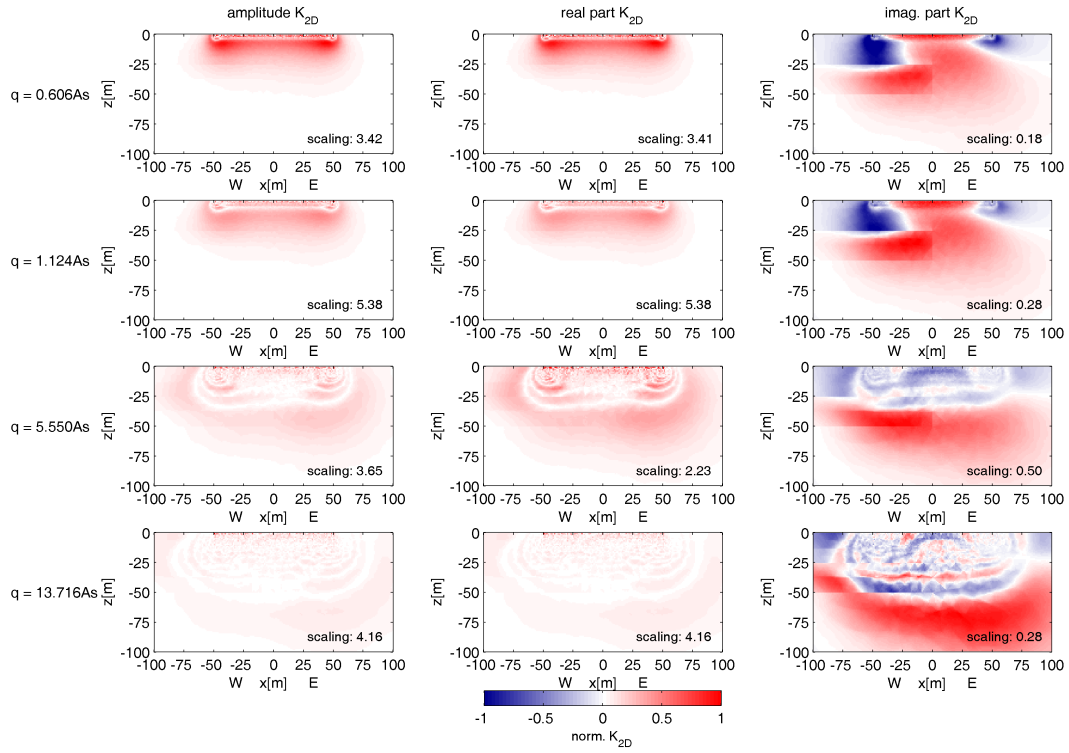

Figure 5.5.: Discontinuous layer - 2D kernel functions for selected pulse moments using a circular loop (d = 100 m, loop centre at the origin of the coordinate system). The data are normalised on their maximum value [nV/m^2] as indicated the lower right corner of each plot of the figure. The subsurface consists of a discontinuous layer (25 m thick, 25 m deep) with a resistivity of 5 Ωm in a surrounding of 50 Ωm. The earth's magnetic field is taken as 48000 nT, 60°N inclination.

The final aim of an MRS modelling are the sounding curves. In order to show the pure resistivity influence, a hypothetical water content of 100 vol.% is assumed in the subsurface. Successively integrating the kernel function over the subsurface volume for each pulse moment yields a complex valued calibration sounding curve.

Shifting loop

I assess the influence of the low resistive discontinuous layer with 5 Ωm in a surrounding of 50 Ωm on the MRS calibration curve (100 vol.% water content) by shifting the loop centre over the discontinuity (Braun et al., 2005b). Figure 5.6 shows the MRS amplitudes and phases calculated for various loop positions over the 2D structure in comparison to the data calculated over a homogeneous half space of 50 Ωm (solid line) and over a layer with 5 Ωm in a surrounding of 50 Ωm at the same depth and with the same thickness as the discontinuous layer (dashed line).

Having a loop centre position of 100 m west to the discontinuity, the MRS data approaches the 1D condition of a layered subsurface. Being in a loop centre distance of 50 m, i.e. the border of the loop is located over the edge of the discontinuity, the MRS data approaches the 1D condition of a layered subsurface only for small pulse moments, i.e. small penetration depths. When the loop centre is directly over the edge of the discontinuity, the MRS data show the strongest 2D effects. The sounding curves approach the conditions of a homogeneous half-space in a distance of one loop diameter to the discontinuity.

Geographical orientation

The influence of the geographical orientation of the discontinuous layer is shown in Figure 5.7. Figure 5.7a shows the MRS data assuming a homogeneous water content of 100 vol.%, whereas in Figure 5.7b MRS data are displayed assuming a realistic 2D water content (30 vol.% water content in the discontinuous layer and 5 vol.% in the surrounding). In each case, the centre of the loop is located over the edge of the discontinuous layer, whereas the geographical orientation of the body is changed as sketched in Figures 5.7c-f.

Assuming a hypothetical water content of 100 vol.% (Fig. 5.7a) to show the pure resistivity effect, there are minor differences in the amplitudes, whereas there are significant differences in the phases. The differences in the phases increase with increasing pulse moments, corresponding to increasing investigation volumes. Considering a realistic 2D water content distribution (Fig. 5.7b), there are significant differences in the ampli-

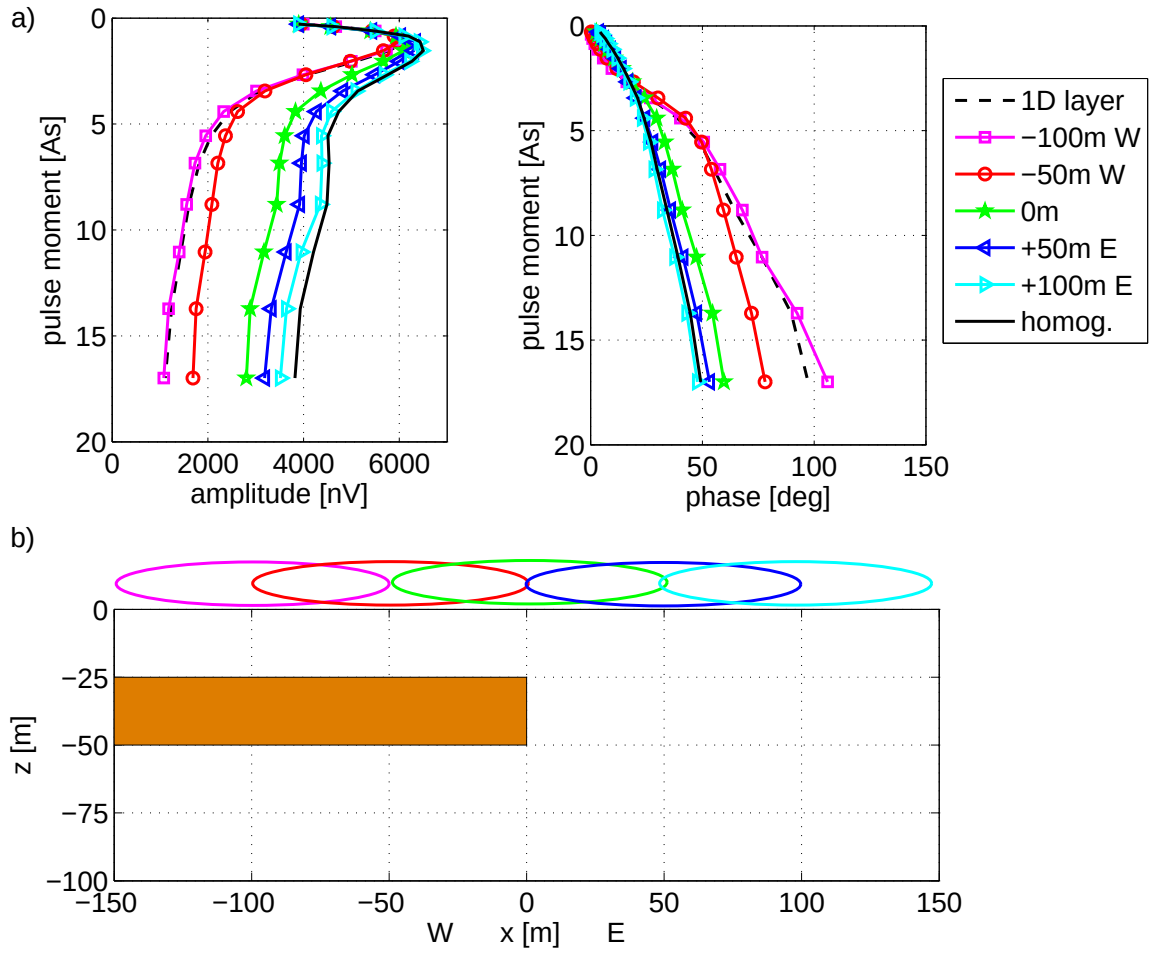

Figure 5.6.: a) Calibration MRS curves for various centre loop positions using a circular loop ($d = 100$ m). Electrical resistivity of the subsurface is 5 Ωm for the discontinuous layer and 50 Ωm for the surrounding. The earth's magnetic field is taken as 48000 nT, 60°N inclination. b) Sketch of the loop layouts.

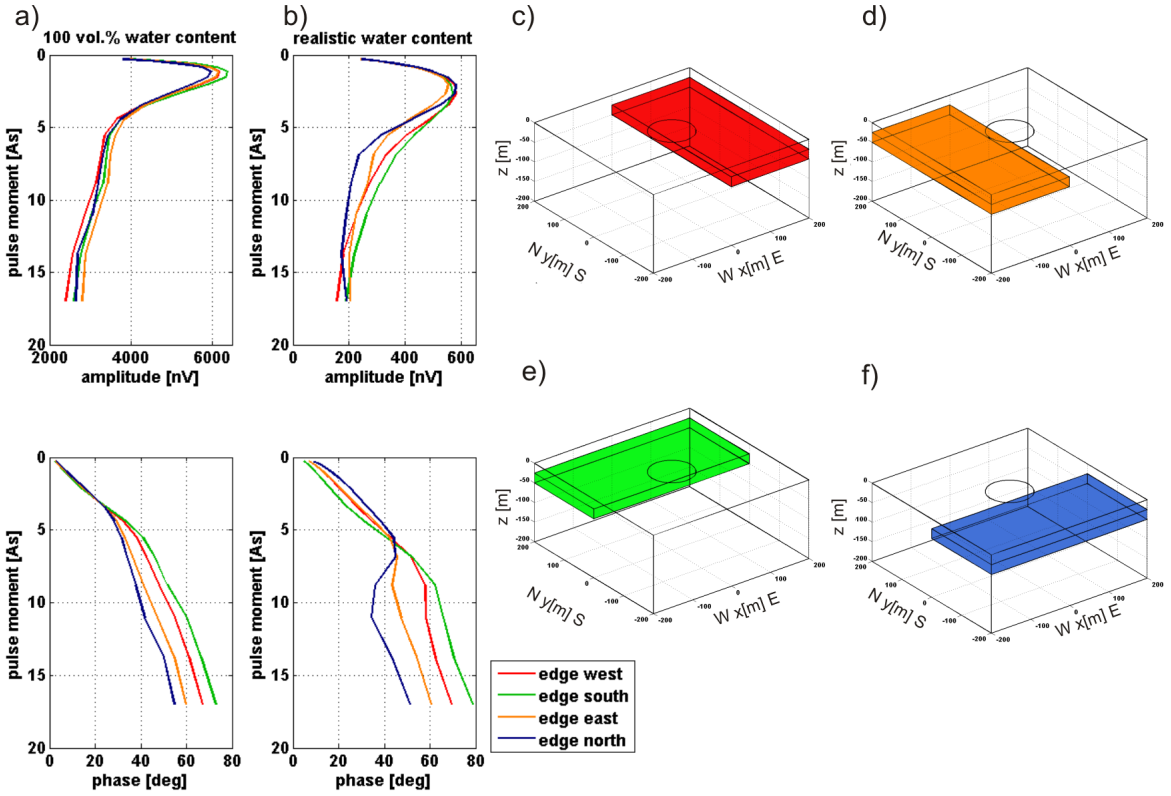

Figure 5.7.: Influence of the geographical orientation of the discontinuous layer. The discontinuous layer has a resistivity of 5 Ωm and the surrounding of 50 Ωm. The top of the layer is at 25m, the thickness is 25 m. a) Calibration MRS sounding curves (100 vol.% water content), b) MRS sounding curves using a realistic 2D water content distribution (30 vol.% in the discontinuous layer, 5 vol.% in the surrounding). The earth's magnetic field is taken as 48000 nT, 60°N inclination. Sketch of the loop layout (d = 100 m) and subsurface c) edge west, d) edge south, e) edge east and f) edge north.

tudes and phases. The 2D water content distribution emphasises the differences in the 2D sensitivities due to the geographical orientation of the low resistive discontinuous layer.

Depth and resistivity

Figure 5.8 shows the influence of the layer depth and resistivity on the MRS data for a discontinuous layer, that extends in east, north and south direction. Analogously to the investigations shown in Figure 5.6, the loop positions are shifted over the discontinuity in 50 m steps. The loop layouts and the subsurface conditions are sketched in the first row in Figure 5.8.

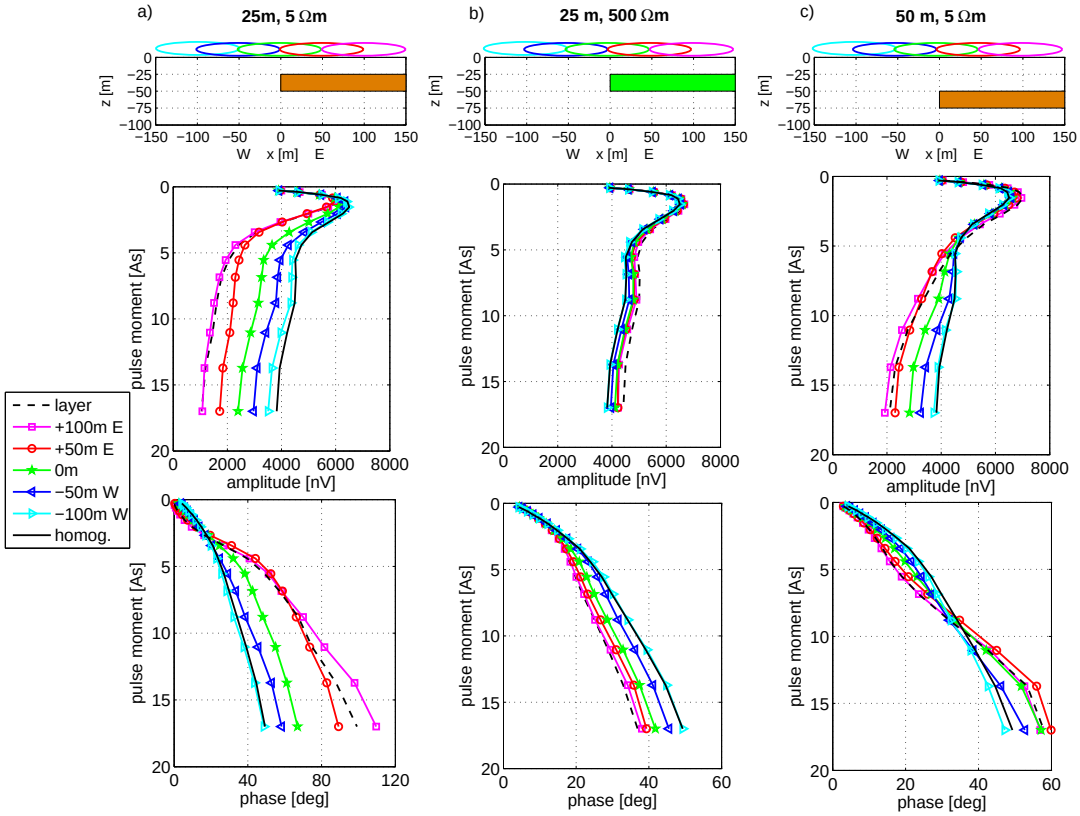

Figure 5.8.: Influence of resistivity and depth of the discontinuous layer. Calibration MRS sounding curves (100 vol.% water content) using a circular loop ($d =$ 100 m). The earth's magnetic field is taken as 48000 nT, 60°N inclination. a) Top of the layer at 25 m with a resistivity of 5 Ωm, b) top of the layer at 25 m with a resistivity of 500 Ωm, c) top of the layer at 50 m with a resistivity of 5 Ωm. The surrounding has a resistivity of 50 Ωm.

The MRS data for a discontinuous layer in 25 m depth with a resistivity of 5 Ωm are displayed in Figure 5.8a. In Figure 5.8b, the resistivity of the subsurface is changed to 500 Ωm. Figure 5.8c shows the MRS data for a discontinuous layer with a resistivity of 5 Ωm, now the top of the body is at 50 m depth. In all cases, the discontinuous layer has a thickness of 25 m and the surrounding has a resistivity of 50 Ωm. Additionally, the corresponding 1D extreme cases are displayed, i.e. the MRS data assuming a homogeneous subsurface with 50 Ωm as well as the data for a corresponding horizontal layer.

The 2D effect of the discontinuous layer is most significant for the case of a low resistivity at a small depth (Fig. 5.8a). The 2D effect decreases for a high-resistive layer (Fig. 5.8b). Shifting the discontinuous layer down to 50 m, the resistivity effect is prominent for pulse moments greater than 5 As (Fig. 5.8c).

5.2.2. Dipping layer

Furthermore, I assess the influence of the dip of a layer exemplary for 0° (horizontal layer), 15° and 30° (Fig. 5.9). The layer has a resistivity of 5 Ωm and the surrounding of 50 Ωm. Figure 5.9a shows the MRS data assuming a hypothetical water content of 100 vol.%. A realistic water content distribution (30 vol.% for the layer and 5 vol.% for the surrounding) is used for the calculated data shown in Figure 5.9b. The layers are sketched in Figures 5.9c (15° dip) and 5.9d (30° dip). The distance from the loop centre to the top of the layer is 37.5 m.

Assuming a homogeneous water content of 100 vol.%, the differences are less visible for the amplitudes. However, there are strong differences for the phases (Fig. 5.9a). The differences are more prominent considering a realistic water content distribution with the layer as aquifer. Then, the amplitudes as well as the phases are significantly affected by the dip of the layer (Fig. 5.9b).

5.2.3. Blocks with varying widths

As next example, I assess the influence on the MRS sounding curves considering 2D blocks (5 Ωm, surrounding 50 Ωm) symmetrically located under the loop centre with varying widths (12.5 m - 200 m). The corresponding MRS calibration curves (circular loop, $d = 100$ m) are shown in Figure 5.10 assuming a hypothetical water content of 100 vol.% to show the pure resistivity effect.

The MRS data calculated for a 200 m wide block approximate those of a horizontally stratified subsurface with a layer at the same depth as well as the same thickness and resistivity as the block. For small pulse moments, corresponding to small penetration depths, a 100 m wide block evokes the same signal as the corresponding layer model. The 2D effect is strongest having a width of 50 m, i.e. half a loop diameter. A block smaller than 25 m, i.e. a quarter of the loop diameter, can be approximated with a homogeneous subsurface.

1D equivalent model

Considering 2D resistivity structures demands a more time consuming forward calculation compared to the previously used 1D layered subsurface models. Therefore, I examine the possibility to replace the true 2D models with 1D equivalent resistivity models in order to reduce the computation time of the forward model.

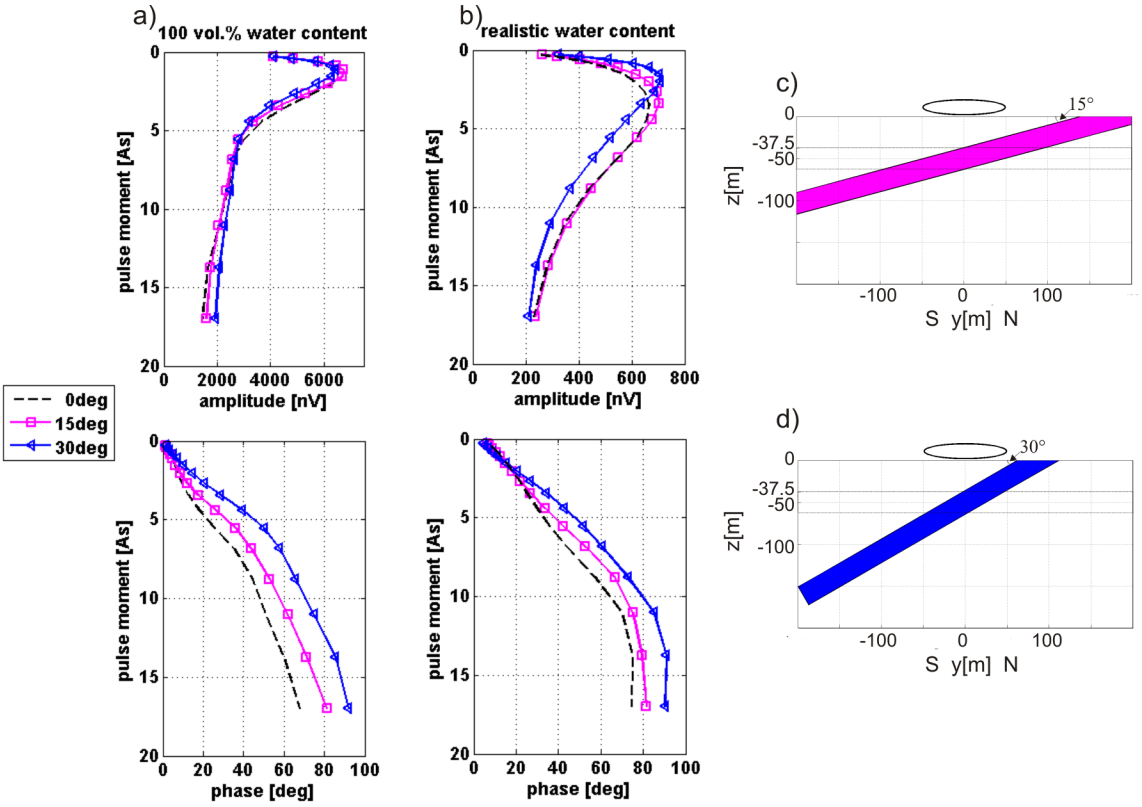

Figure 5.9.: Influence of a dipping layer (15° and 30°) compared to a horizontal layer (0°) at a depth of 37.5 m. a) Calibration MRS sounding curves (100 vol.% water content), b) MRS sounding curves using a realistic water content distribution (30 vol.% in the layer, 5 vol.% in the surrounding), c) Sketch of the layer with a dip of 15° and d) dip of 30° to the south. The layers are 25 m thick. The depth under the loop centre is 37.5 m. The resistivity of the layer is 5 Ωm and 50 Ωm of the surrounding. The data are calculated using a circular loop ($d = 100$ m) and magnetic field intensity of 48000 nT and 60°N inclination.

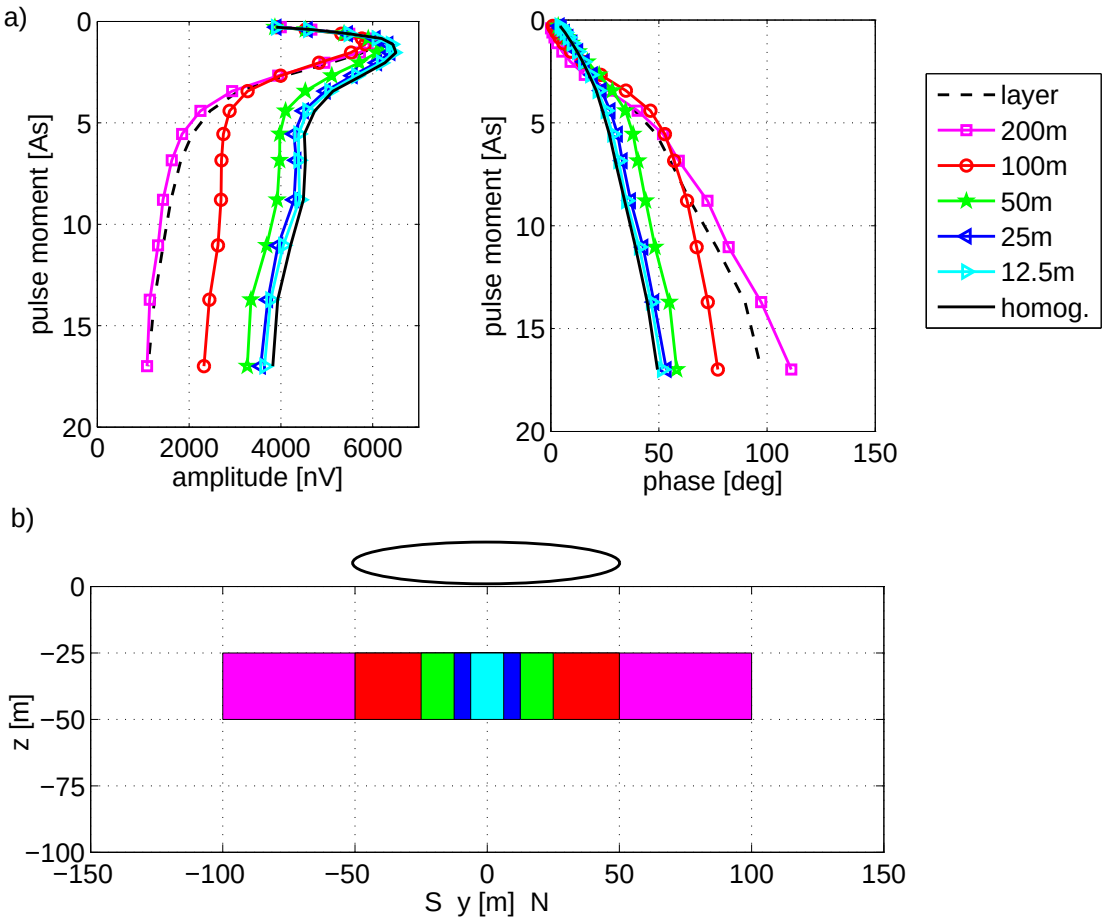

Figure 5.10.: a) Calibration MRS curves (100 vol.% water content) for various 2D block sizes as well as a homogeneous subsurface (50 Ωm) and a horizontal layer at the same depth and with the same thickness as the blocks. Resistivity of the blocks is 5 Ωm and 50 Ωm for the surrounding. The data are calculated using a circular loop (d = 100 m) with an earth's magnetic field of 48000 nT and 60°N inclination. b) Sketch of the blocks.

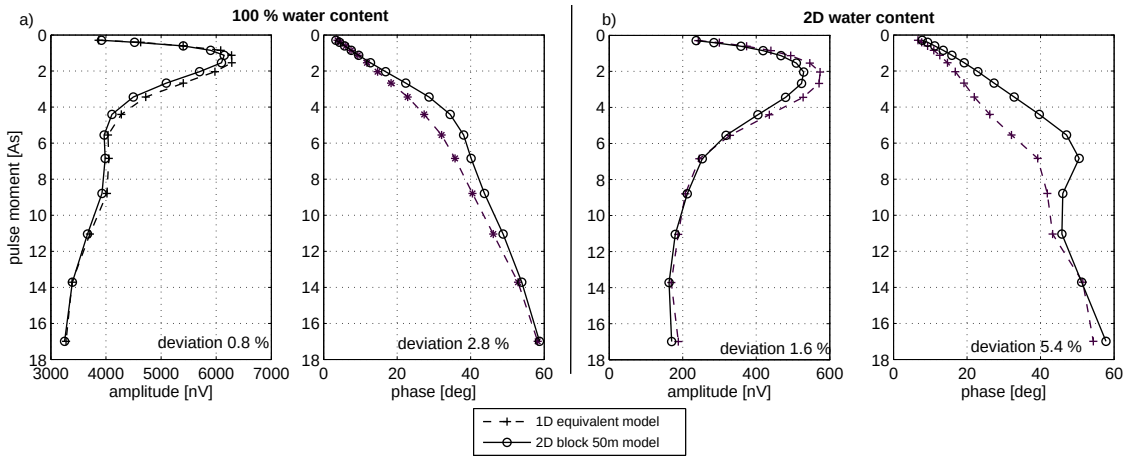

Figure 5.11.: Comparison between the data of a 2D block (50 m width, 25 m thick at 25 m depth, 5 Ωm, see Fig. 5.10) and a 1D equivalent model of a thin layer (2 m thick layer at 36.5 m depth, 5 Ωm). The surrounding has a resistivity of 50 Ωm. a) 100 vol.% water content, b) realistic 2D water content distribution (30 vol.% in the block, 5 vol.% elsewhere). The data are calculated using a circular loop ($d = 100$ m) with an earth's magnetic field of 48000 nT and 60°N inclination.

Exemplary for the case of a 50 m wide block, I looked by manually trial and error for a 1D thin layer equivalent resistivity model. The found 1D equivalent resistivity model is a 2 m thick layer at 36.5 m depth. The corresponding data for a hypothetical water content of 100 vol.% are displayed in Figure 5.11a. The amplitudes are quite the same, but the phases differ.

However, in MRS the water content distribution is the target of investigation. Under reasonable field conditions, there is a 2D water content distribution along with a 2D resistivity distribution. Having now corresponding to a 2D electrical resistivity also a 2D water content (30 vol.% in the block, 5 vol.% in the surrounding), the 1D conductivity model cannot explain the 2D modelled amplitude and especially the phases (Fig. 5.11b).

Hence, even if a 1D equivalent resistivity model can be found replacing a 2D resistivity distribution using a hypothetical homogeneous water content, this is no longer valid using a reasonable 2D water content distribution. So it is absolutely necessary to take a 2D resistivity distribution into account along with a 2D water content distribution.

Looking at the 2D sensitivity function for a pulse moment of e.g. 1.1 As (Fig. 5.12) clarifies this: The real part is attenuated and the imaginary part is amplified in the area of the block. Multiplying this sensitivity function with the 2D water content yields the calculated amplitude and phase value for this particular pulse moment (see Eq. 3.30).

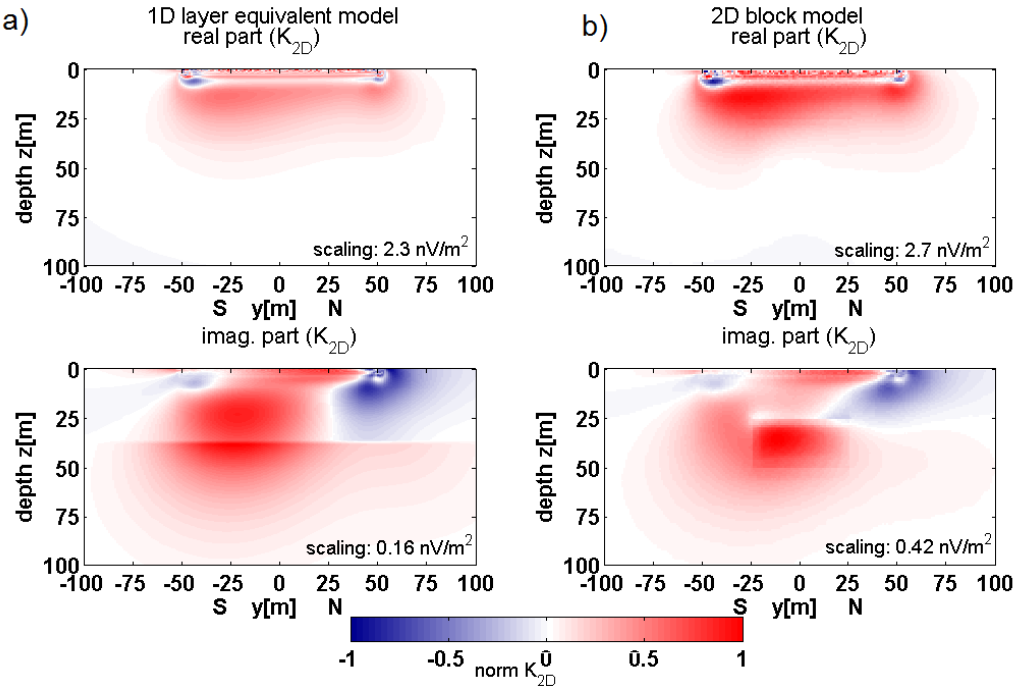

Figure 5.12.: Real and imaginary part of the 2D kernel functions of a pulse moment of $q = 1.1$ As. The data are normalised on their maximum value as indicated in the lower right corner of each plot. a) 1D equivalent layer (2 m thick layer at 36.5 m depth, 5 Ωm), b) 2D block (50 m width, 25 m thick at 25 m depth, 5 Ωm). The surrounding has a resistivity of 50 Ωm.

Thus, the water content scales the lateral and vertical impact of the sensitivity function on the MRS amplitude and phase value. Therefore, differences in the sensitivity function due to differences in the resistivity model are reflected in the MRS signal using a 2D water content distribution.

To conclude, 1D equivalent models can be found for a certain water content distribution. However, there is no general rule to substitute a 2D resistivity with an equivalent 1D resistivity. Moreover, one must be aware that the used resistivity distribution affect the kernel function. Thus, the water content distribution determined by the inversion depends on the used resistivity distribution. This has been shown for the 1D case in Section 4.2.4.

Having a 2D data set to be interpreted, there are three possibilities concerning the resistivity distribution used in the 2D water content inversion:

1. The resistivity can be neglected; an insulating half-space is used.

2. The resistivity contrast is negligible, and a homogeneous resistivity model is used. Or, the resistivity structure is very small, and that is the reason, why a homogeneous subsurface model is used.
3. The resistivity cannot be neglected. Then the 2D resistivity should be used, because the sensitivity of the water content distribution depends on the used resistivity distribution.

Up to now, option 1 or 2 is chosen in a 2D water content distribution. The effects of an inappropriate 2D resistivity on 2D water content determination will be shown in future studies.

6. Development of a 1D MRS inversion scheme deriving resistivity and water content

Since the resistivity affects the MRS signal in the forward modelling, I assess how to extract this information from the MRS measurements. The resistivity of the subsurface must be taken into account when analysing MRS data. Conventionally, this is done by a priori information obtained from additional geophysical methods such as geoelectric or time domain electromagnetic, from borehole measurements or from an estimation based on the geology.

In case of unavailable a priori information or to prove the assumed resistivity, it is very useful to determine the resistivity as an inversion parameter when analysing the MRS data. Therefore, a new inversion scheme for determining 1D water content and 1D resistivity from coincident loop MRS measurements is developed.

As the applied magnetic field depends on the resistivity of the subsurface, the complete forward problem must be recalculated in each iteration. Hence, I developed a 1D inversion scheme, that combines the stability of a well proven block inversion using the guided random search algorithm simulated annealing (SA) with the fast convergence of a least square (LS) algorithm (Braun et al., 2006; Braun and Yaramanci, 2006).

6.1. The forward calculation of the excitation field

The calculation of the excitation field is the most demanding part of the forward problem. I used the finite element programme COMSOL Multiphysics 3.2 with the following settings:

- Axial symmetry (2D) → Electromagnetic Module → Quasi-Statics Magnetic → Azimuthal Induction Current → Time-harmonic analysis → Application mode name: emqa

- Drawing the geometry: air half-space and subsurface with layers as rectangles, the loop is represented as a point at a distant of one loop radius. The air-ground-interface is at $z = 0$ m. The geometry must be sufficiently great that the boundary condition "magnetic insulation" is valid.
- Physics:
  - Changing the electric parameters of the subdomains
  - Axial symmetry as boundary condition along $r = 0$ m and magnetic insulation for the other boundaries
  - Assigning a value of 1 A to the point representing the loop
  - The frequency as scalar variable must be adjusted (e.g. 2000 Hz)
- Initialising mesh
- Solving with adaptive mesh refinement

As long as the subsurface geometry is axial symmetric, as it is the case of a horizontally layered subsurface, the problem can be solved in the 2D axial symmetry mode. This reduces the computation time as well as the required memory. The field is calculated for one slice of the 3D volume in vertical and radial direction; there are no variations in the angular direction. When the full 3D solution is required for further calculations, the 2D axial symmetric solution is rotated by 360°.

Since the plane of the geometry represents one section through the 3D model, the loop is represented by a point at the surface ($z = 0$ m) at the distance of one loop radius ($r_L = 50$ m for a loop with a diameter of $d = 100$ m).

The mesh is initialised using the default parameters of the program (Fig. 6.1a). In case of a 3-layer model with resistivities of 50 Ωm in the first and third layer and 5 Ωm in the second layer between 25 and 50 m, the initial mesh consists of 884 elements and the number of degree of freedom is 1833. Using the adaptive mesh refinement for solving, the number of elements is 9139 and the number of degree of freedom is 18358 after two refinements (Fig. 6.1b). The solution time is 3.4 s using a standard PC.

Adaptive mesh generation identifies the regions where high resolution is needed and produces an appropriate mesh (COMSOL, 2005). The mesh is finer around the loop, the mesh size increases for distant regions (Fig. 6.1).

Figure 6.2 shows the norm of the magnetic flux density B_{norm} for the initial mesh and the mesh after adaptive mesh refinement

$$B_{norm} = \sqrt{|\mathbf{B}_r|^2 + |\mathbf{B}_z|^2}, \tag{6.1}$$

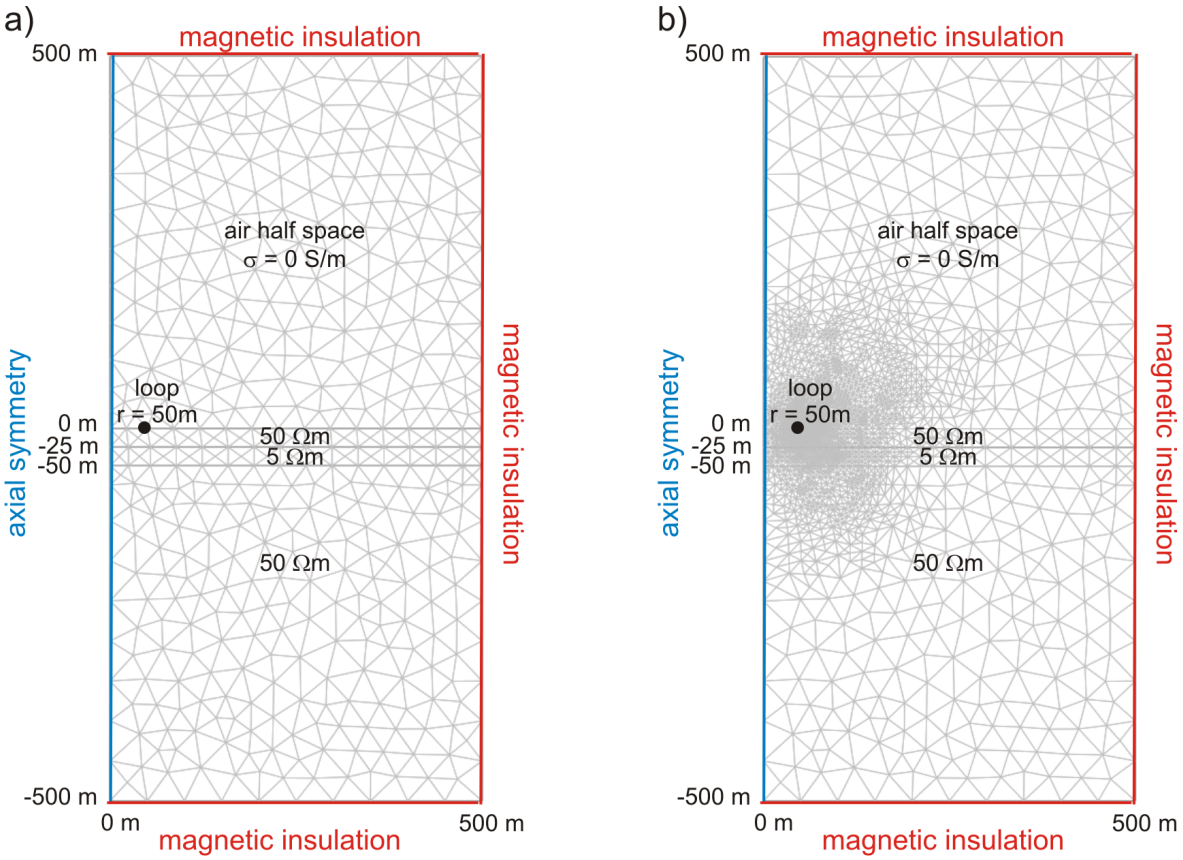

Figure 6.1.: a) Initial mesh and b) mesh after adaptive mesh refinement for a 2D axial symmetric problem.

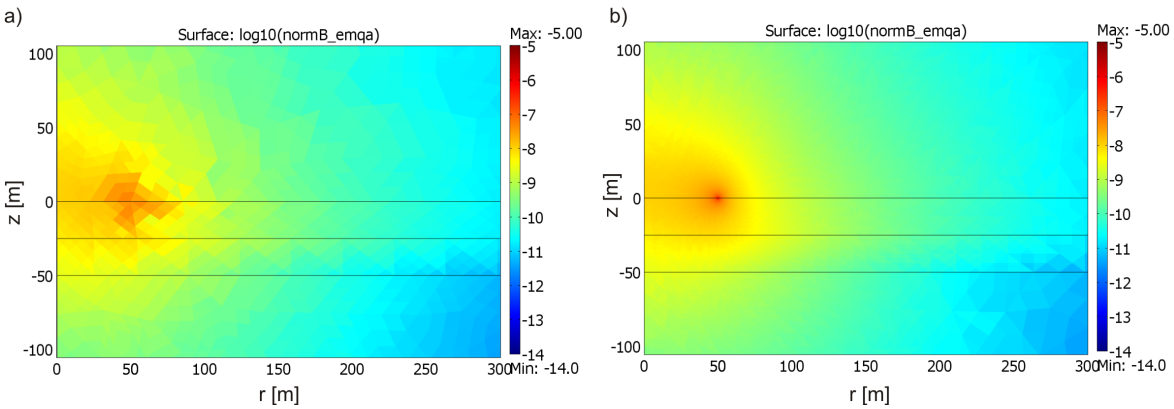

Figure 6.2.: Norm of the magnetic flux density B_{norm} [$\log_{10}$(T)] a) initial mesh, b) after mesh refinement during solving process. The loop has a radius of $r_L = 50$ m and its centre is at $z = 0$ m and $r = 0$ m.

where $\mathbf{B}_r$ is the radial component and $\mathbf{B}_z$ is the vertical component of the magnetic flux density. The need of the refinement in the vicinity of the loop is immediately obvious.

6.2. Sensitivity analyses

The aim of computing the sensitivities is to evaluate quantitatively how a change of one model parameter affects the data. The sensitivities are calculated using the perturbation approach (McGillivray and Oldenburg, 1990). This is the most straightforward approach to calculate the differential sensitivities by approximating them using the one-sided finite difference formula

$$\frac{\partial F_j(m)}{\partial m_k} \approx \frac{F_j(m + \Delta m_k) - F_j(m)}{\Delta m_k}. \tag{6.2}$$

The perturbed forward response $F_j(m+\Delta m_k)$ is obtained by recalculating the forward problem after perturbing the kth parameter by an amount Δm_k. Since the model must be altered to compute the perturbed response, each sensitivity requires the solution of the complete forward problem. So this method is time consuming, but it is a simple method suitable for complicated forward problems.

6.2.1. Homogeneous subsurface

Figure 6.3 shows MRS calibration sounding curves (100 vol.% water content) for several resistivities (1, 10, 100, 1000, 10000 Ωm) and various loop sizes (d = 100 m, 50 m, 10 m). The number of loop turns (1 turn and 2 turns) is varied for a loop size of d = 50 m. The phase values are corrected to produce a smoother phase plot. Multiples of 360° are added in case of absolute jumps in the phase greater than 180°. This figure is the same as Figure 4.13, already described in Section 4.2. The influence of the resistivity on the sounding curves and the dependence of the loop size is immediately obvious.

In order to further investigate the effects of resistivity, loop size and number of turns, I calculated the arithmetic mean of one MRS sounding curve for amplitude and phase as well as the gradient of the arithmetic mean as sensitivity using various resistivities of the homogeneous subsurface. Following equations are used:

$$\overline{E_0}(\rho) \quad = \quad \frac{1}{N} \sum_{i=1}^{N} E_0(\rho, q_i) \tag{6.3}$$

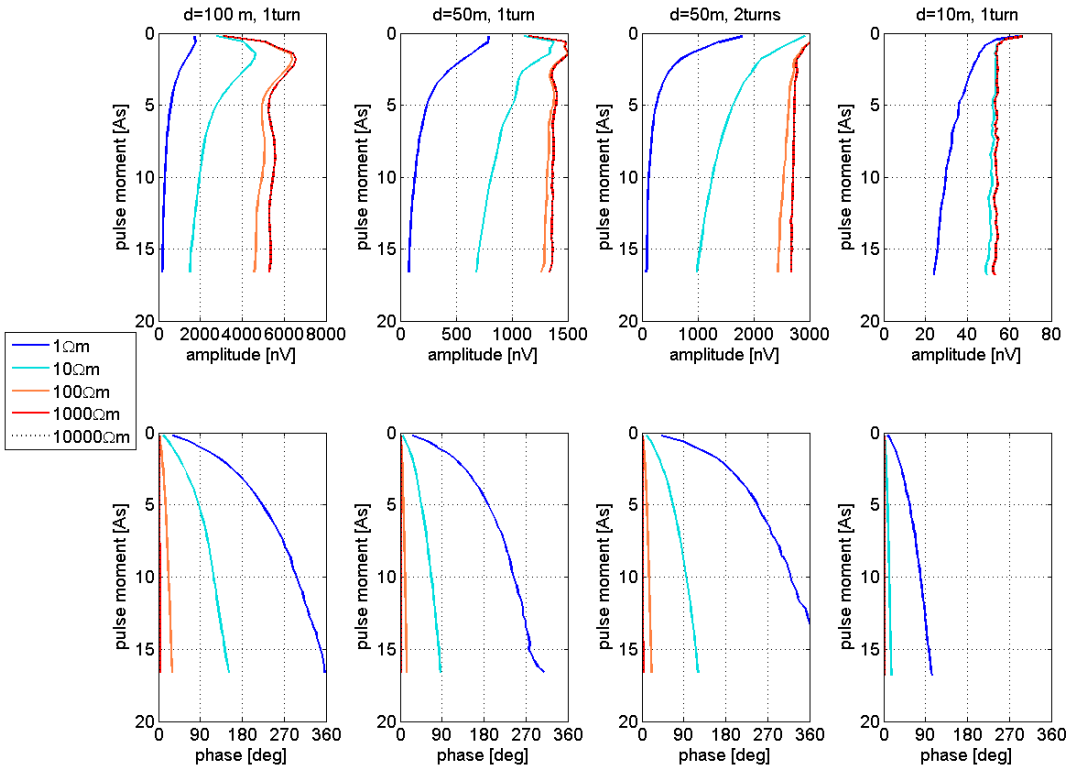

Figure 6.3.: Homogeneous half-space - MRS calibration soundings (100 vol.% water content) for several resistivities of an homogeneous half-space between 1 and 10000 Ωm. The data are calculated using circular loops with diameters of $d = 100$ m, 1 turn; $d = 50$ m, 1 turn; $d = 50$ m, 2 turns; $d = 10$ m, 1 turn and magnetic field intensity of 48000 nT and 60°N inclination.

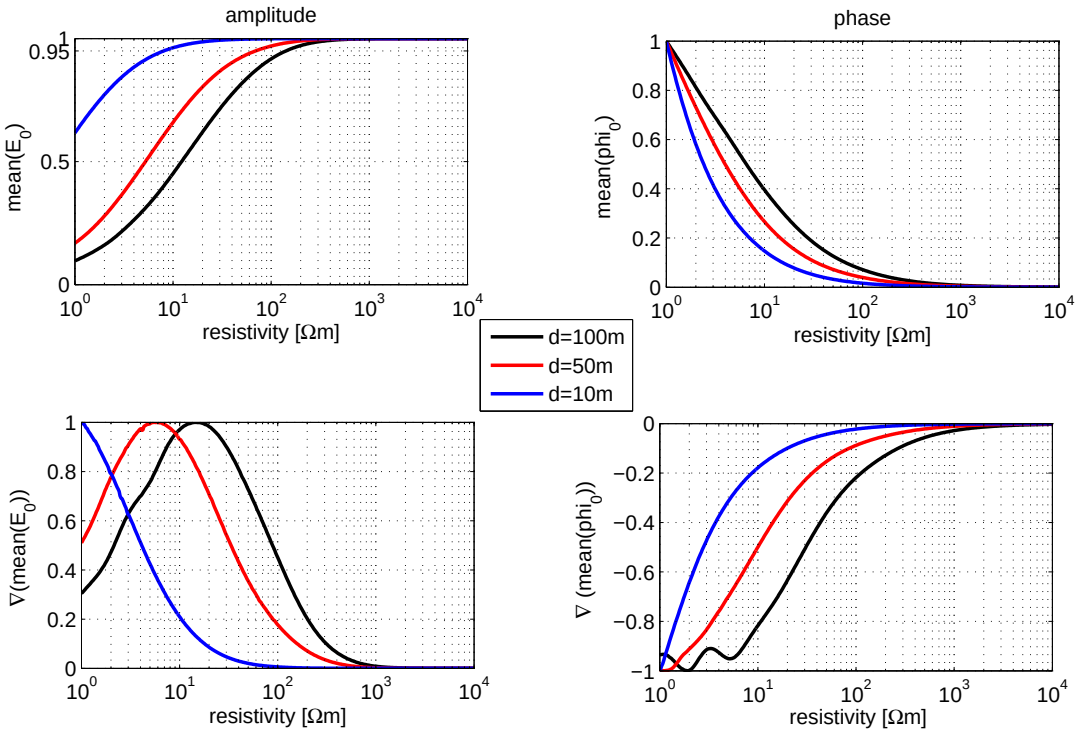

Figure 6.4.: Homogeneous half-space - Arithmetic mean (top) and gradient of the arithmetic mean (bottom) of the amplitude and phase of the MRS calibration curve (100 vol.% water content) for homogeneous half-spaces with resistivities between 1 and 10000 Ωm. For convenience of comparison, the data are normalised on their maximum value. Circular loops are used with diameters of $d = 100$ m, 50 m, 10 m (each 1 turn), and magnetic field intensity of 48000 nT and 60°N inclination.

$$\nabla\left(\overline{E_0}(\rho)\right) = \frac{\partial\left(\overline{E_0}(\rho)\right)}{\partial \log_{10}(\rho)} \tag{6.4}$$

$$\overline{\varphi}_0(\rho) = \frac{1}{N}\sum_{i=1}^{N}\varphi_0(\rho, q_i) \tag{6.5}$$

$$\nabla\left(\overline{\varphi_0}(\rho)\right) = \frac{\partial\left(\overline{\varphi_0}(\rho)\right)}{\partial \log_{10}(\rho)}, \tag{6.6}$$

where N is the number of pulse moments q_i. So I obtain a relationship between the arithmetic mean $\overline{E_0}(\rho)$ of the amplitude and $\overline{\varphi}_0(\rho)$ of the phase as well as the gradient of the arithmetic mean $\nabla\left(\overline{E_0}(\rho)\right)$ of the amplitude and $\nabla\left(\overline{\varphi_0}(\rho)\right)$ of the phase and the resistivity of the homogeneous subsurface ρ.

Figure 6.4 top illustrates the dependence of the arithmetic mean of one sounding curve for amplitude and phase on the resistivity of a homogeneous subsurface using a virtual

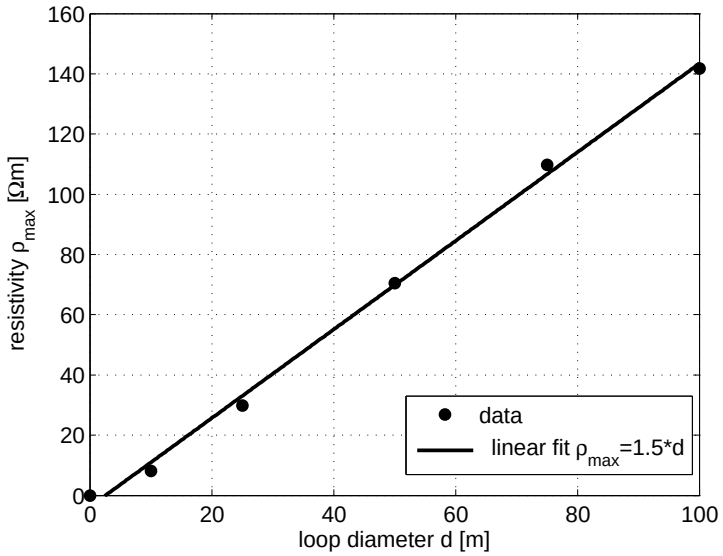

Figure 6.5.: Maximum effective resistivity as deduced from the amplitudes of the arithmetic means shown in Figure 6.4.

water content of 100 vol.%. Analogously to Figure 6.3, the data are calculated for loop sizes of $d = 100$ m, $d = 50$ m and $d = 10$ m. Figure 6.4 bottom shows the gradient of the curves in Figure 6.4 top. For convenience of comparison, all the data are normalised on their maximum value.

As expected from the sounding curves in Figure 6.3, the arithmetic mean of the amplitudes of the sounding curves converges to an upper limit for higher resistivities. Consequently, the sensitivity, i.e. the gradient of the arithmetic mean, converges to zero.

The arithmetic mean of the phases decreases for increasing resistivities. For higher resistivities, the arithmetic mean as well as the gradient of the arithmetic mean converges to zero. Thus, the amplitude as well as the phase is not sensitive for changes of the resistivity if the half-space resistivity is greater than a specific cut-off value depending on the loop size.

Figure 6.5 shows the dependence of the maximum effective resistivity ρ_{max} on the loop diameter d, where ρ_{max} is defined as the resistivity value at 95 % of the maximum arithmetic mean value. Additionally to the data shown in Figure 6.4, the maximum effective resistivity is also calculated for $d = 25$ m and $d = 75$ m. The relationship between the maximum effective resistivity and the loop diameter, as deduced from Figure 6.4, can be approximated using a linear fit with $\rho_{max} = 1.5 \cdot d$.

Table 6.1.: Subsurface parameters of model 1 and model 2

	model 1			model 2		
layer number	1	2	3	1	2	3
water content [vol. %]	5	30	5	5	30	5
resistivity [Ωm]	50	**5**	50	50	**500**	50
layer thickness [m]	25	25	∞	25	25	∞
layer depth [m]	0-25	25-50	50-∞	0-25	25-50	50-∞

6.2.2. 3-layer model

The previous investigations have been conducted using an electrically homogeneous subsurface with a virtual water content of 100 vol.%. Table 6.1 shows the subsurface parameters of two 3-layer models. They differ only in the resistivity of layer 2: model 1 has a low resistive aquifer with 5 Ωm and model 2 represents a high resistive aquifer with 500 Ωm. A 3-layer model can be described by eight parameters: water content and resistivity for layer 1, 2 and 3 as well as layer thickness of layer 1 and 2; layer 3 is the underlying half-space.

The sensitivities are calculated using Equation 6.2 regarding water content, resistivity and layer thickness. Thus, only one parameter is changed at a time, the other eight parameters remain the same.

Figures 6.6 (model 1) and 6.7 (model 2) show the arithmetic mean of the sounding curves for amplitude and phase when changing one of the eight subsurface parameters at a time. Figures 6.8 (model 1) and 6.9 (model 2) display the sensitivities in terms of the gradient of the arithmetic mean.

For convenience of comparison, the axis limits are the same for the corresponding diagrams of model 1 and model 2. The sensitivities of model 1 and model 2 differ for all parameters even if only the resistivity of the second layer is changed.

Water content

The amplitude increases linearly with the water content (Figs. 6.6a and 6.7a), therefore, the sensitivity is constant for each layer (Figs. 6.8a and 6.9a). The sensitivity increases with decreasing layer depth, i.e. a change of the water content in the first layer has a greater impact on the sounding curve than the same change of the water content in the second or third layer. This reflects the reduced resolution with increasing depth. Due to the higher resistivity of layer 2 in model 2, the penetration depth increases

and consequently, the sensitivity regarding the water content is greater, especially for layer 2 and 3 (Fig. 6.9a).

Generally, the sensitivity of the phase is smaller in model 2 compared to model 1 (Figs. 6.8b and 6.9b). This is caused by the higher resistivity of layer 2 in model 2 and the corresponding smaller phase effects. The phase decreases with increasing water content of layer 1 and it remains constant for a water content greater than 30 vol.% (Figs. 6.6b and 6.7b). The sensitivity of layer 1 is negative for small water contents, and it converges to a constant value close to zero for water contents greater than 30 vol.%. Also the sensitivity of the phases of layer 2 and 3 approximate a constant value close to zero for water contents greater than 30 vol.% (Figs. 6.8b and 6.9b). However, the sensitivity of the phase of layer 2 is positive for model 1 (Fig. 6.8b), but negative for model 2 (Fig. 6.9b). For layer 3, the sensitivities of model 1 and model 2 are positive. In contrary to the sensitivities of the amplitudes, the water content of the underlying half-space (layer 3) has the greatest effect on the phase (Figs. 6.8b and 6.9b).

Resistivity

The shape of the sensitivity of the resistivity is the same for model 1 and model 2 (Figs. 6.8c,d and 6.9c,d). Obviously, the sensitivity of layer 2 must be the same for both models. The resistivity of layer 1 has the main impact on the sounding curve (Figs. 6.6c,d and 6.7c,d) and therefore, the sensitivities are highest for layer 1, and they decrease for increasing layer depth. The sensitivities converge to zero for resistivity values greater than 100 Ωm.

Due to the larger resistivity in layer 2 of model 2, the amplitudes are higher for resistivities greater than 5 Ωm in layer 1 (Figs. 6.6c and 6.7c) and consequently, the maximum of the amplitude of the sensitivity curve of layer 1 is higher and shifted to a greater value for model 2 (Fig. 6.9c). The sensitivities of the phase are negative (Figs. 6.8d and 6.9d), i.e. the phases decrease for increasing resistivities (Figs. 6.6d and 6.7d). Again, the resistivity of the first layer affects the sounding curve the most.

Layer thickness

The sensitivities of the amplitudes regarding the thickness of layer 1 are negative (Figs. 6.8e and 6.9e). Due to the small water content (5 vol.%) in layer 1, the amplitudes decrease for increasing layer thickness (Figs. 6.6e and 6.7e). In contrary, the sensitivities are positive regarding the thickness of layer 2. The amplitudes increase for increasing layer thickness of the aquifer (30 vol.% water content). The sensitivity of

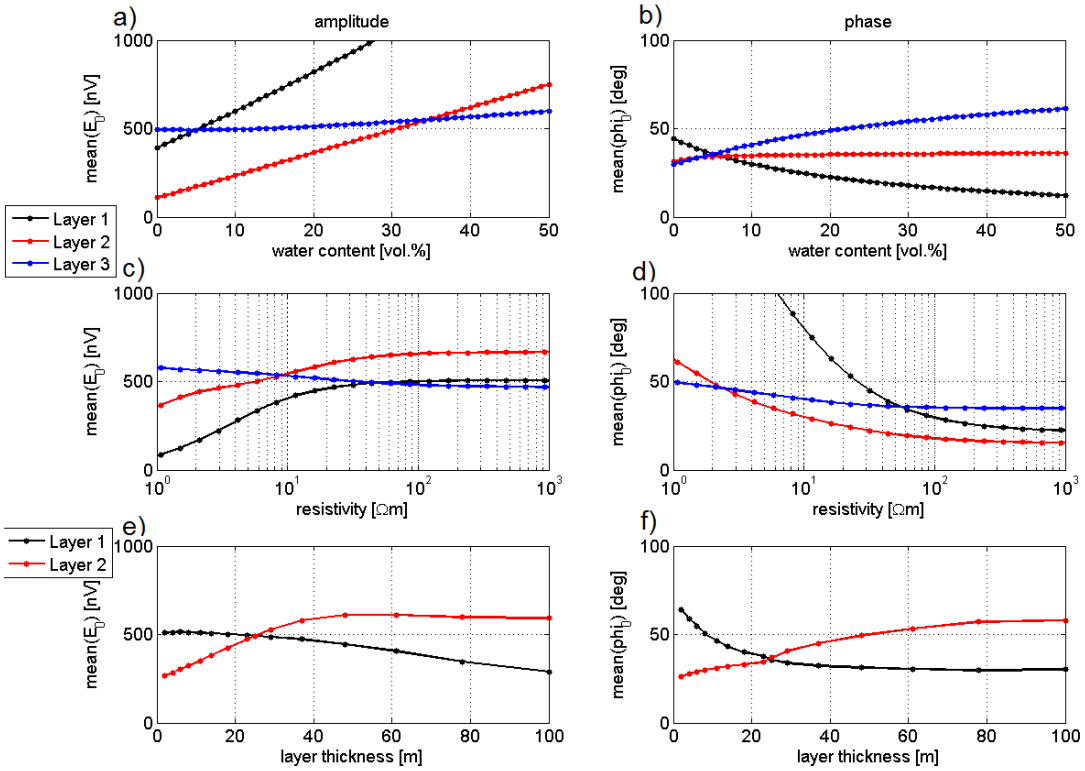

Figure 6.6.: Model 1 - Arithmetic mean of the amplitude and phase of the MRS curve using the subsurface parameters of model 1. The data are calculated using a circular loop ($d = 100$ m) and magnetic field intensity of 48000 nT and 60°N inclination.

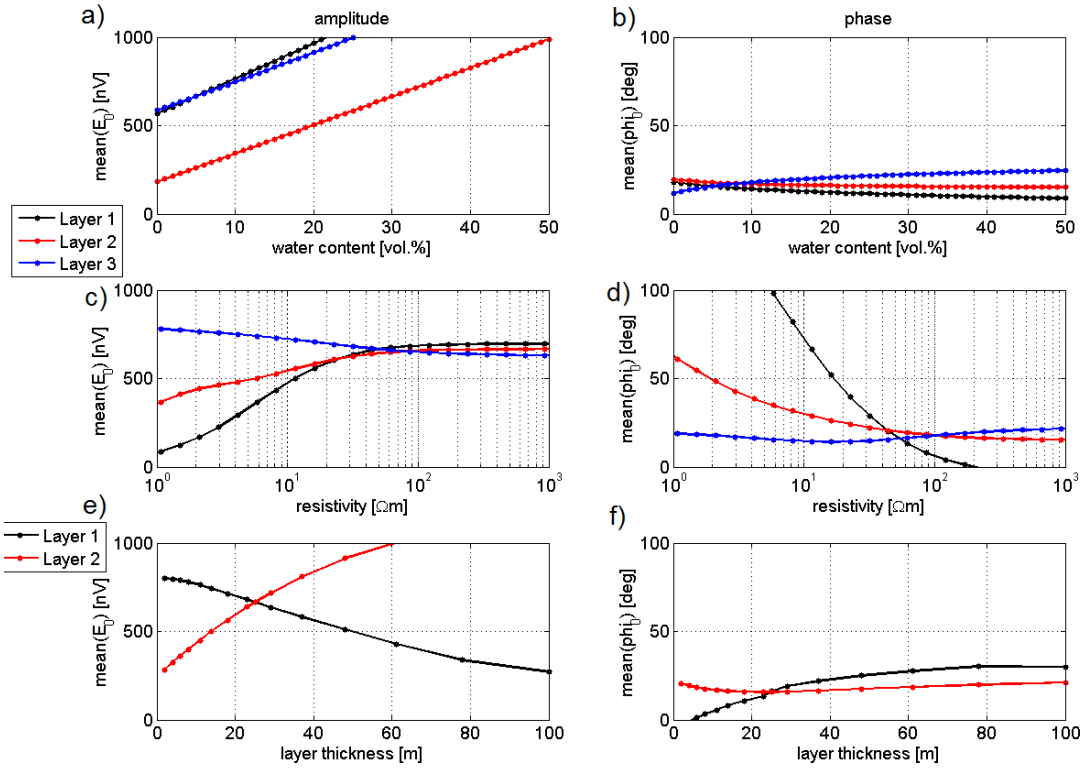

Figure 6.7.: Model 2 - Arithmetic mean of the amplitude and phase of the MRS curve using the subsurface parameters of model 2. The data are calculated using a circular loop ($d = 100$ m) and magnetic field intensity of 48000 nT and 60°N inclination.

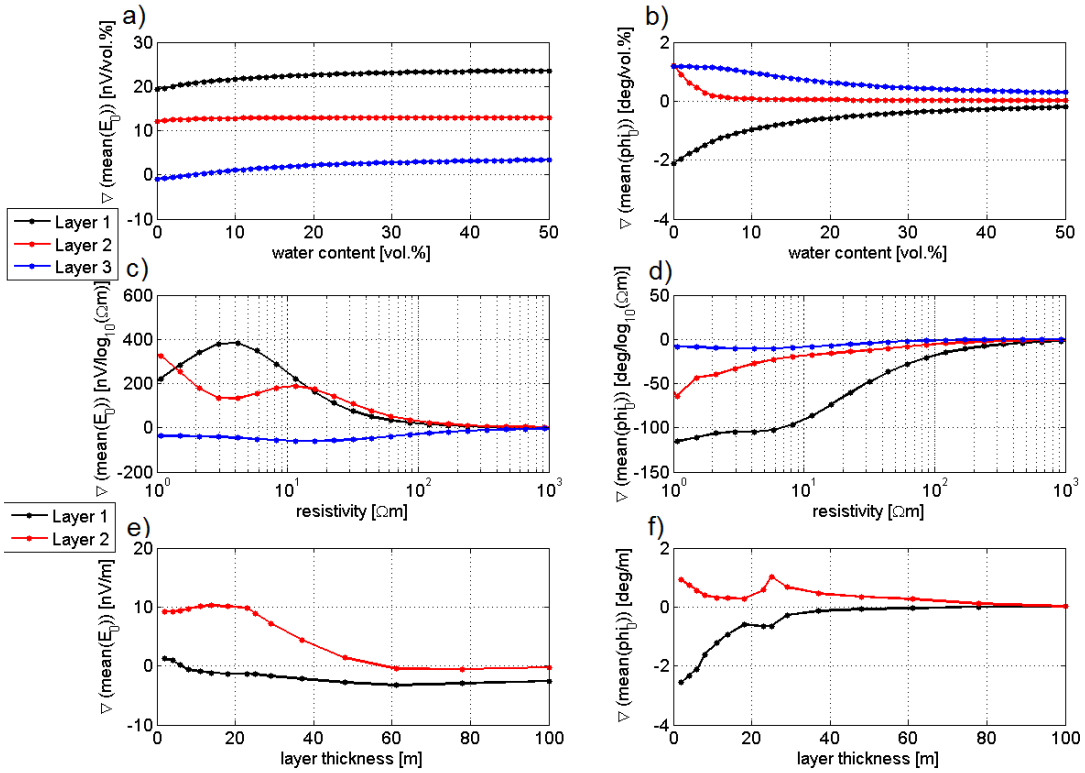

Figure 6.8.: Model 1 - Sensitivity of amplitude and phase of the MRS curve using the subsurface parameters of model 1. The data are calculated using a circular loop (d = 100 m) and magnetic field intensity of 48000 nT and 60°N inclination.

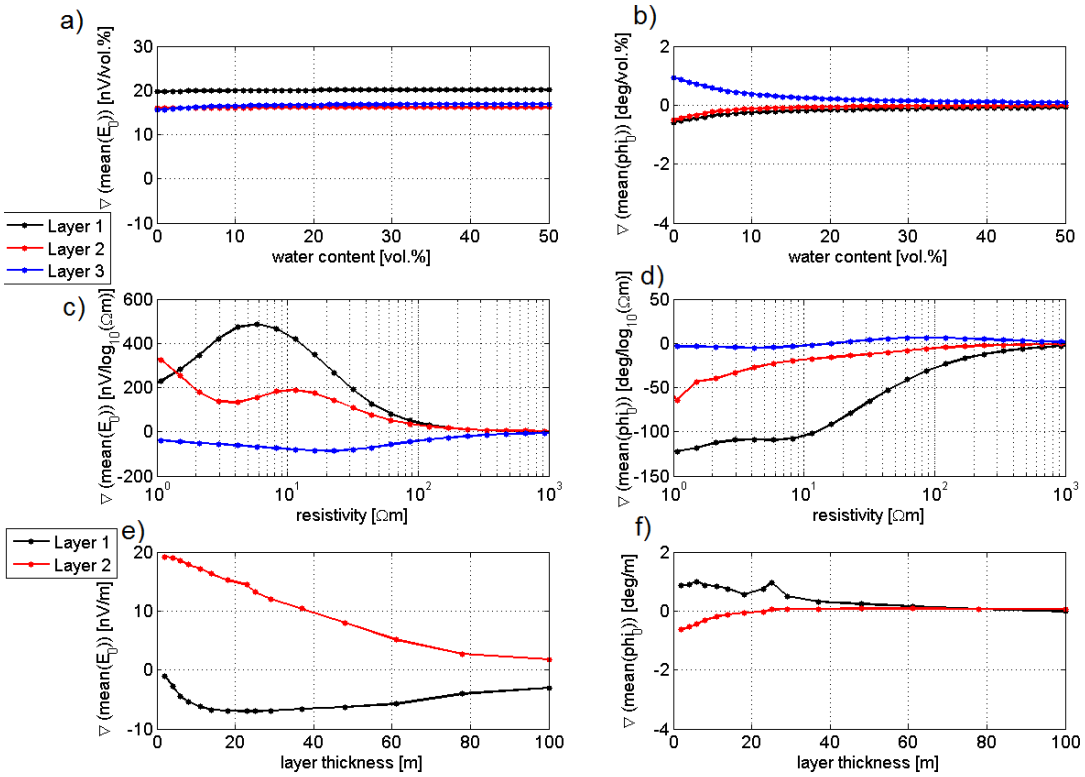

Figure 6.9.: Model 2 - Sensitivity of amplitude and phase of the MRS curve using the subsurface parameters of model 2. The data are calculated using a circular loop (d = 100 m) and magnetic field intensity of 48000 nT and 60°N inclination.

layer 1 converges to zero for model 1 (Fig. 6.8e). The penetration depth is limited due to the lower resistivity (5 Ωm), thus, an increase of the thickness of the aquifer does not result in an increase of the amplitude of the sounding curve for a layer thickness greater than 60 m (Fig. 6.6e). Due to the higher resistivity of model 2, the amplitudes still increase in the considered range of layer thickness (Fig. 6.7e). However, the sensitivity decreases for increasing layer thicknesses.

The sign of the sensitivity of the phase is opposite for model 1 and model 2 (Figs. 6.8f and 6.9f). In model 1, the phase increases for increasing layer thicknesses of the low resistive layer 2 (Fig. 6.6f). In model 2, the resistivity of layer 1 (50 Ωm) is lower than the resistivity of layer 2 (500 Ωm). Thus, the phase increases for increasing layer thicknesses of layer 1 (Fig. 6.7f). In both models, the sensitivities converge to zero for a layer thickness greater than 60 m.

The study of the sensitivities for homogeneous subsurface and for two 3-layer models has shown that the sensitivities strongly depend on the whole subsurface model. The sensitivities must be calculated for each individual case.

6.3. Numerical implementation

6.3.1. Sketch of the inversion scheme

The inversion scheme is based on well proven inversion algorithms: the guided random search algorithm simulated annealing (SA), described in Corona et al. (1987), as well as the least square algorithm "lsqnonlin" (LS) from the MATLAB optimisation toolbox (MATLAB, 2007a).

Since the excitation magnetic field depends on the resistivity of the subsurface, the forward problem must be solved in each iteration step. Because this is a time consuming calculation, a fast converging algorithm is demanded. Therefore I chose the algorithm "lsqnonlin" from the MATLAB optimisation toolbox for determining the resistivity. The finite element programme COMSOL Multiphysics calculates the excitation field, transmitted from a circular loop (see Section 6.1).

The drawback of the "lsqnonlin" algorithm lies in the instability when used as block inversion. This may be due to the high variations of the kernel functions especially for small depths. Therefore, I decided to combine the SA block inversion and the "lsqnonlin" algorithm.

Figure 6.10 describes the inversion scheme. The SA inversion needs an initial guess (e.g. 100 Ωm) for the resistivity, then it determines in run 1 the water content and depths

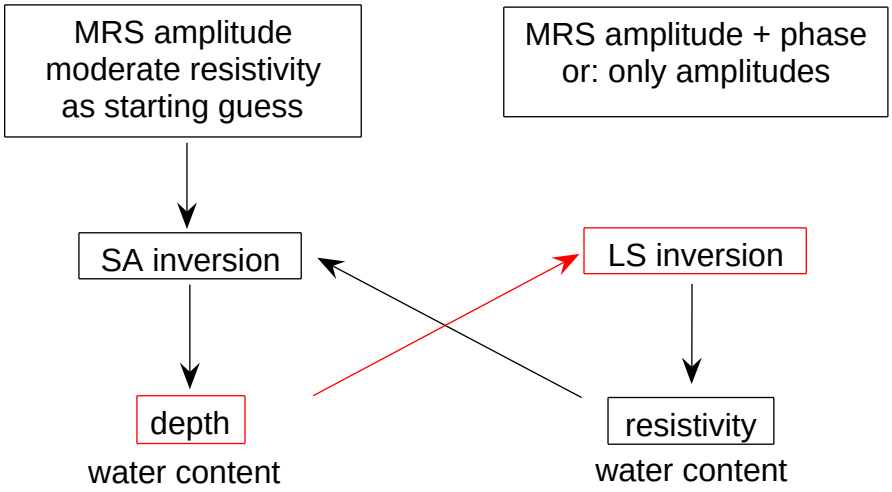

Figure 6.10.: Inversion scheme for coincident circular loop measurements to determine 1D resistivity, depth and water content using a combination of simulated annealing (SA) block inversion and least square (LS) algorithm with fixed layer boundaries.

fitting the MRS amplitude. The LS inversion uses these depths as fixed layer boundaries and determines for the layers resistivity and water content fitting amplitude and phase. One can choose to fit only the amplitude (amplitude inversion) or amplitude and phase (complex inversion). From the inversion run 2, the SA inversion uses the resistivity distribution of the LS inversion, but the depths for the water content determination are again free inversion parameters. So there is an iterative process converging to an inversion result.

If the number of layers in a block inversion is too high, the block inversion produces very thin layers ($<$ 1 m thickness), that are geologically inappropriate. These very thin layers are ignored by the LS inversion. This reduces the computation time without any loss of information. However, in the next run of the block inversion the initial number of layers is allowed. The LS inversion determines water content and resistivity using fixed boundaries. The SA inversion needs the resistivity distribution as a priori information, but it determines the depths from the water content distribution independently from the depths of the resistivity distribution.

6.3.2. The inversion algorithm

The equations necessary for calculating MRS data are described in Chapter 3. For the numerical implementation, Equation 3.28 must be discretised

$$E_0(q,\rho(V)) = \omega_0 M_0 \frac{2}{I_0} \sum_{0}^{z_{max}} \sum_{y_{min}}^{y_{max}} \sum_{x_{min}}^{x_{max}} f(x,y,z) \sin\left(\gamma \frac{q}{I_0} \left|\mathbf{B}_T^+(x,y,z;\omega_0,\rho(V))\right|\right) \times \left|\mathbf{B}_T^-(x,y,z;\omega_0,\rho(V))\right| \cdot e^{i2\zeta_T(x,y,z;\omega_0,\rho(V))} \Delta x \Delta y \Delta z. \quad (6.7)$$

The parameters have been explained in Chapter 3. The lower and upper boundary of the sum in horizontal direction x_{min}, x_{max}, y_{min}, y_{max} are chosen as $6 \cdot r_L$, where r_L is the loop radius. Thus, for a loop diameter $d = 100$ m, corresponding to a loop radius $r_L = 50$ m, $x_{min} = x_{max} = y_{min} = y_{max} = 300$ m. The upper boundary in vertical direction z_{max} is chosen as 200 m in case of a loop with $d = 100$ m. The subsurface is divided into basis layers with the thickness Δz. For a loop diameter $d = 100$ m, $\Delta z = 1$ m is chosen. However, the layer boundaries in the block inversion are not bound by the thickness of the basis layers used for discretisation of the subsurface. The components of the excitation magnetic field are calculated in the subroutine "forward B-field" (see Section 6.1).

In case of 1D conditions, Equation 6.7 can be decomposed in a kernel function $K_{1D}(q,z)$ (see Chapter 3) and a water content distribution $f(z)$

$$E_0(q) = \sum_{0}^{z_{max}} K_{1D}(q,\rho(V),z) \cdot f(z)\,\Delta z. \quad (6.8)$$

Equation 6.8 is used in the subroutine "forward MRS data". The 1D kernel function $K_{1D}(q,z)$ is calculated in the subroutine "forward kernel" as

$$K(q,\rho(V),z) = \omega_0 M_0 \frac{2}{I_0} \sum_{y_{min}}^{y_{max}} \sum_{x_{min}}^{x_{max}} \sin\left(\gamma \frac{q}{I_0} \left|\mathbf{B}_T^+(x,y,z;\omega_0,\rho(V))\right|\right) \times \left|\mathbf{B}_T^-(x,y,z;\omega_0,\rho(V))\right| \cdot e^{i2\zeta_T(x,y,z;\omega_0,\rho(V))} \Delta x \Delta y. \quad (6.9)$$

Finally, the algorithm minimises f_{opt} calculated as

$$f_{opt} = \frac{1}{\sqrt{N}} \sqrt{\sum_{i=1}^{N} \left(E_{0meas,i} - E_{0cal,i}\right)^2}, \quad (6.10)$$

where the vector E_{0meas} contains the measured data and E_{0cal} the forward calculated data using Equation 6.8. Two inversion algorithms are used. The guided random search algorithm simulated annealing (SA) is used in the block inversion for determining water content and layer boundaries using a fixed number of layers. Thus, the inversion is

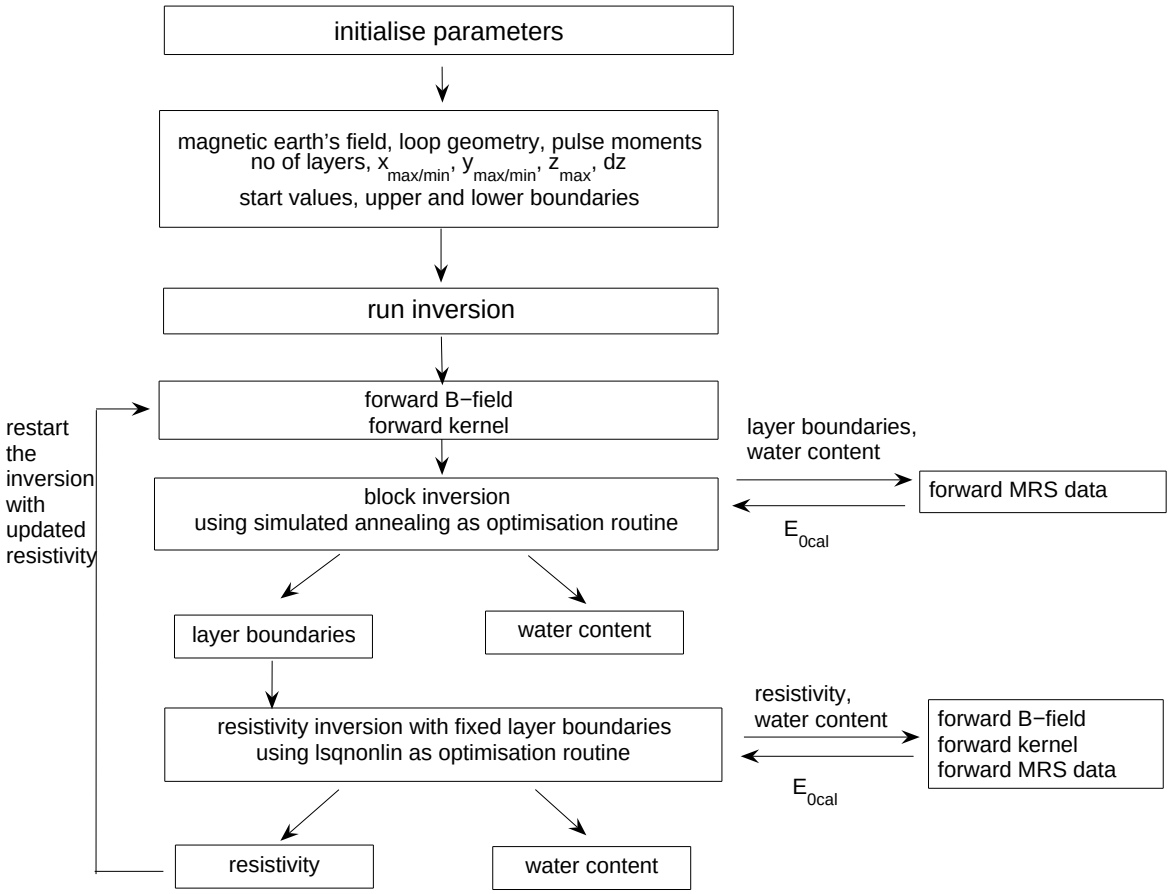

Figure 6.11.: Flowchart of the MRS resistivity inversion.

stabilised by the fixed number of layers. The SA inversion uses only the amplitudes of the complex MRS signal. Therefore, the parameter N is the number of pulse moments.

The least square algorithm "lsqnonlin" from the MATLAB Optimisation Toolbox is used for determining water content and resistivity using fixed layer boundaries determined by the block inversion using SA. Thus, the inversion is stabilised by the fixed layer boundaries. It is preferable to use the amplitude and phase of the MRS data for the resistivity inversion. Then, the vectors E_{0meas} and E_{0cal} contain real and imaginary parts of the MRS sounding curve. Consequently, the parameter N (Eq. 6.10) is twice the number of pulse moments.

The flowchart in Figure 6.11 recapitulates the used inversion algorithm.

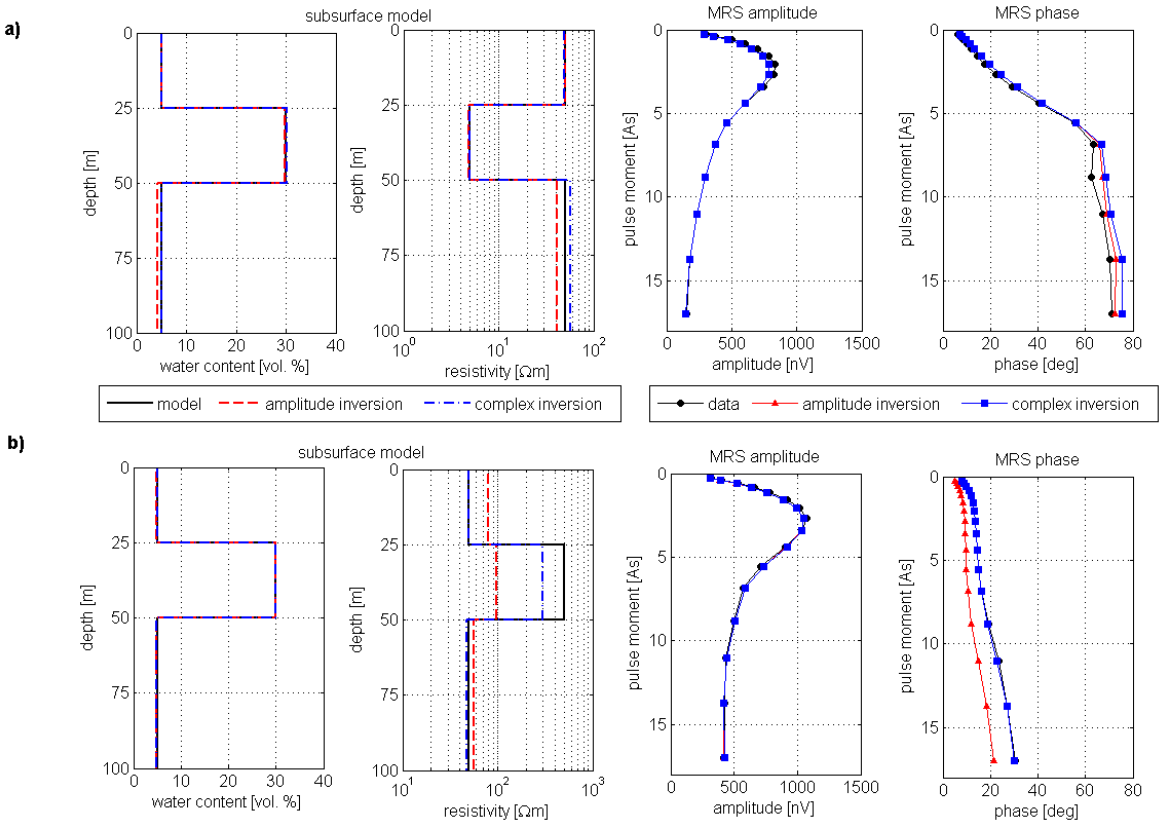

Figure 6.12.: Inversion results for synthetic noise free data using a 3-layer model with the aquifer (5 Ωm (a) and 500 Ωm (b), 30 vol.%; surrounding 50 Ωm, 5 vol.%) between 25 and 50 m. The data are calculated using a circular loop (d =100 m) and magnetic field intensity of 48000 nT and 60°N inclination. Comparison of inversion results using only the amplitude (red) inversion and using amplitude and phase (complex inversion, blue) for the LS inversion.

6.4. Verification and tests with synthetic data

6.4.1. Tests using the layer thickness as a priori information

The principal feasibility was tested having the layer thickness as a priori information using only the LS inversion. Layer thicknesses of 5 m, 10 m, 25 m and 50 m were used to create 3-layer models. Calculating all possible permutations, 16 models were generated (Appendix Tab. C.1). The principal water content distribution remains for all models the same: 5 vol.% for the first and third layer and 30 vol.% for the second layer. The resistivity for the first and third layer is 50 Ωm. The resistivity of the second layer was changed from 5 Ωm to 500 Ωm.

The results for 3-layer models with different thicknesses (Appendix Fig. C.1 and C.2) show that the resistivity of a low resistive (5 Ωm) aquifer can be determined better than the resistivity of a medium resistive (500 Ωm) aquifer. Having a low resistive aquifer, a pure amplitude inversion is sufficient. Fitting amplitude and phase of the MRS signal, the inversion results are improved.

Figure 6.12 shows exemplary the inversion results for a 3-layer model with the aquifer between 25 and 50 m. It shows the comparison between an amplitude inversion and a complex inversion with the layer thickness as a priori information (fixed true layer boundaries) using two resistivities of the aquifer: 5 Ωm (Fig. 6.12a) and 500 Ωm (Fig. 6.12b).

Having a low resistive aquifer (5 Ωm) and the layer thickness as a priori information (Fig. 6.12a), water content and resistivity can be revealed by a pure amplitude inversion. Considering also the phase in the inversion process improves the result slightly.

Using only the amplitude in the case of a high resistive aquifer (500 Ωm), the inversion result shows the modelled water content distribution even if the determined resistivity distribution is not correct (Fig. 6.12b). However, the trend of the resistivity distribution is adequate. The determination of the resistivity distribution can be significantly improved by using also the MRS phase in the inversion.

6.4.2. Tests without a priori information

After showing the principal feasibility having the layer thickness as a priori information, the inversion scheme, as described in Section 6.3.1, is applied exemplary on two 3-layer subsurface models: the resistivity of the aquifer is 5 Ωm in model 1 and 500 Ωm in model 2; all other parameters remain the same (see Tab. 6.1).

Model 1 - low resistive aquifer

Model 1 consists of a 25 m thick layer with 50 Ωm and 5 vol.%, the aquifer has 5 Ωm and 30 vol.%, and the third layer again 50 Ωm and 5 vol.% (Tab. 6.1). The calculated amplitude and phase values are drawn as black circles in Figures 6.13 and 6.14 using a circular loop ($d = 100$ m) as coincident transmitter and receiver.

Since the amplitude is a more stable measurement parameter than the phase, it is preferable to use only the amplitude during the inversion. Figure 6.13 shows the inversion result using only the amplitude also for the LS inversion. A moderate resistivity of 100 Ωm is used as start value for the SA inversion.

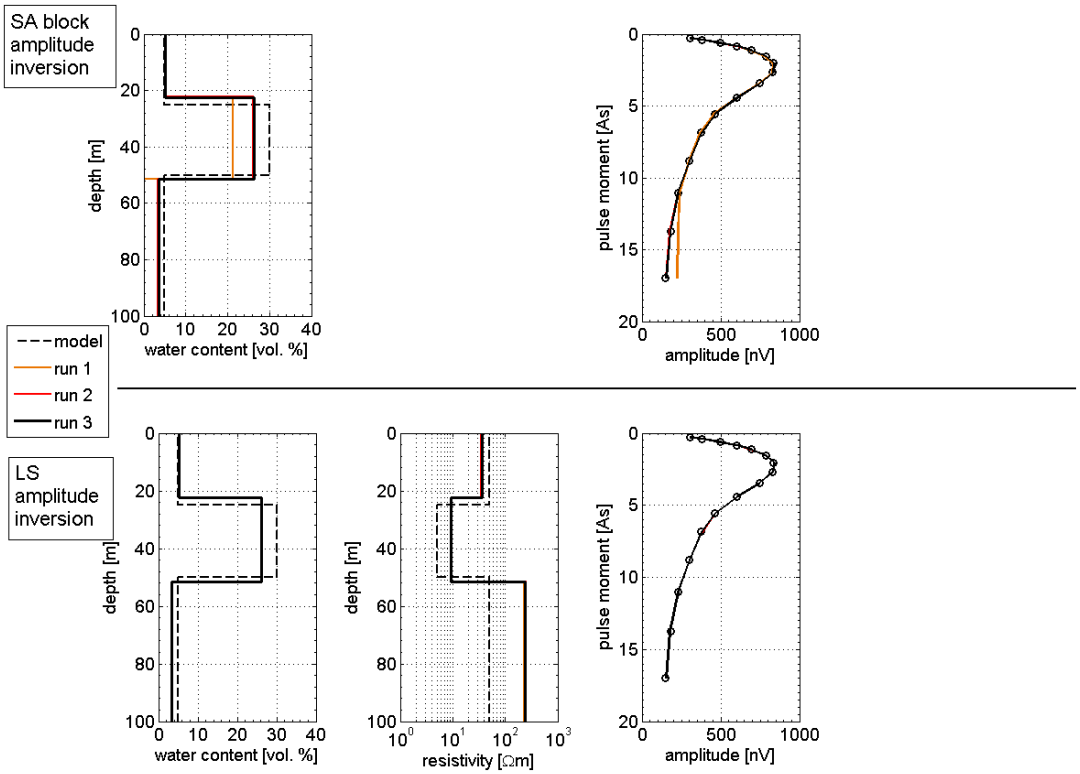

Figure 6.13.: Model 1 - Inversion scheme is applied on synthetic noise free data using a 3-layer model with the aquifer (5 Ωm, 30 vol.%; surrounding 50 Ωm, 5 vol.%) between 25 and 50 m. The data are calculated using a circular loop (d = 100 m) and magnetic field intensity of 48000 nT and 60°N inclination. Inversion results using only the amplitude for SA and LS inversion.

A water content distribution is determined by fitting the amplitude (Fig. 6.13 top, run 1). The boundaries of the aquifer are quite well determined, but the water content is underestimated. The LS inversion uses these depths as fixed layer boundaries and determines water content and resistivity for them by fitting the amplitude (Fig. 6.13 bottom, run 1). The SA inversion run 2 uses the adapted resistivities of the LS inversion. Due to the improved values of the resistivity, the SA inversion is superior in resolving the water content of the aquifer. However, the thickness of the aquifer does not change significantly. Therefore, the LS inversion run 2 and 3 do not differ from run 1. The trend of the resistivity distribution, determined by the LS inversion, reflects the modelled values. The resistivity of the aquifer is overestimated, but still in the right order of magnitude. As consequence, the water content is underestimated.

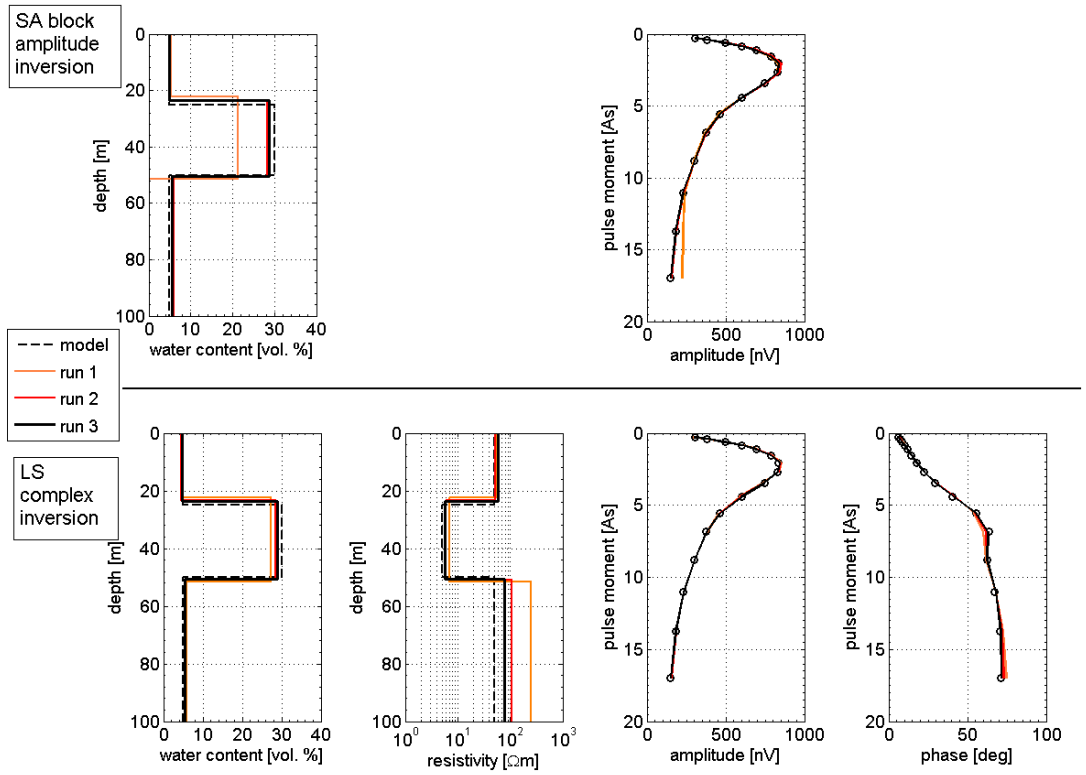

Figure 6.14.: Model 1 - Inversion scheme is applied on synthetic noise free data using a 3-layer model with the aquifer (5 Ωm, 30 vol.%; surrounding 50 Ωm, 5 vol.%) between 25 and 50 m. The data are calculated using a circular loop (d = 100 m) and magnetic field intensity of 48000 nT and 60°N inclination. Inversion results using only the amplitude for SA inversion, but using amplitude and phase (complex inversion) for the LS inversion.

Since the MRS phase contains valuable information about the resistivity, it can be incorporated into the inversion process. Figure 6.14 shows the inversion result for the same subsurface model as in Figure 6.13, now using amplitude and phase for the LS inversion. Actually, real and imaginary parts are used in the inversion.

Again, a moderate resistivity of 100 Ωm is used as start value for the SA inversion. A water content distribution is determined by fitting the amplitude (Fig. 6.14 top, run 1). Obviously, the result is the same as in Figure 6.13 top, run 1. The boundaries of the aquifer are quite well determined, but the water content is underestimated. The LS inversion uses these depths as fixed layer boundaries and determines water content and resistivity for them by fitting amplitude and phase (Fig. 6.14 bottom, run 1). The SA inversion run 2 uses the adapted resistivities of the LS inversion. Due to the improved

values of the resistivity, the SA inversion is better in resolving thickness and water content of the aquifer. Using the improved depth values, the LS inversion can better estimate the resistivity in run 2. Resistivity and water content distribution estimated in run 3 approximate the given model.

Figure 6.15 shows the sensitivity of the inversion result in terms of the root-mean-square (rms) error with respect to the MRS data of the original model for amplitude, phase as well as real and imaginary part of the eight inversion parameters. The rms error is calculated for amplitude, phase as well as real and imaginary part as:

$$\mathrm{rms}_{Ampl} = \frac{1}{\sqrt{N}} \sqrt{\sum_{i=1}^{N} \left(|E_{0mod,i}| - |E_{0cal,i}|\right)^2} \tag{6.11}$$

$$\mathrm{rms}_{phase} = \frac{1}{\sqrt{N}} \sqrt{\sum_{i=1}^{N} \left(\arg\left(E_{0mod,i}\right) - \arg\left(E_{0cal,i}\right)\right)^2} \tag{6.12}$$

$$\mathrm{rms}_{ReIm} = \frac{1}{\sqrt{2N}} \cdot \sqrt{\sum_{i=1}^{N} \left(\mathfrak{Re}\left(E_{0mod,i}\right) - \mathfrak{Re}\left(E_{0cal,i}\right)\right)^2 + \sum_{i=1}^{N} \left(\mathfrak{Im}\left(E_{0mod,i}\right) - \mathfrak{Im}\left(E_{0cal,i}\right)\right)^2} \tag{6.13}$$

where N is the number of pulse moments, E_{0mod} are the MRS data calculated for the eight parameters of the original model and E_{0cal} are the MRS data using seven parameters of the original model but changing one parameter. Equation 6.11 is used in the amplitude inversion and Equation 6.13 is used in the complex inversion.

For example in Figure 6.15 (top, black line) the rms is drawn versus the change of the water content in the first layer using Equations 6.11 (Fig. 6.15 left), 6.12 (Fig. 6.15 middle) and 6.13 (Fig. 6.15 right); all other parameters (water content for layer 2 and 3 as well as resistivity for layer 1-3 and layer thickness for layer 1-2) remain the same. The other diagrams can be understood analogously.

Figure 6.15 shows immediately which parameters have the main impact on the rms of amplitude and phase. For convenience of comparison, the axes limits are the same for all diagrams. The absolute minimum is located at the original value of the model.

There is a linear relationship for the water content for all layers with respect to the rms error of real and imaginary parts. However, the linear relationship is not valid for the rms of amplitude and phase.

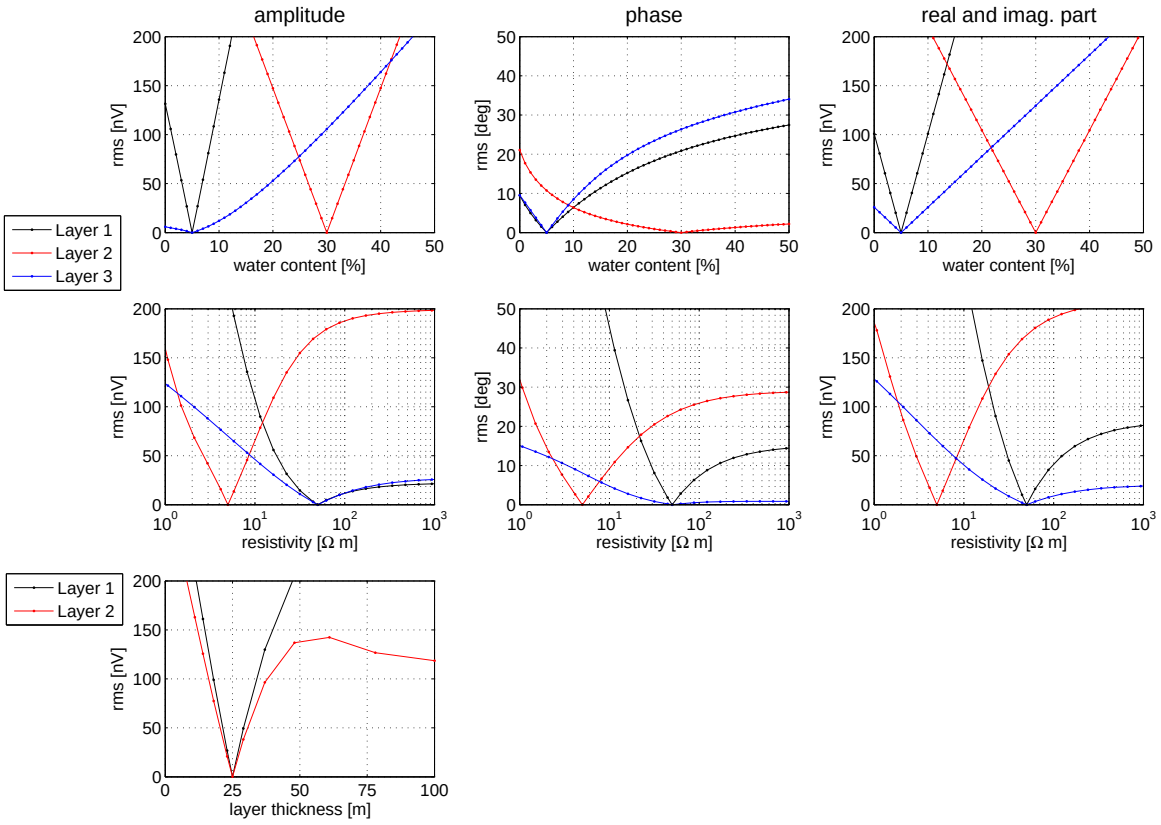

Figure 6.15.: Model 1 - Sensitivity of the inversion result in terms of rms for amplitude, phase as well as real and imaginary part of the eight inversion parameters. Model parameters are: 5 vol.% (Layer 1), 30 vol.% (Layer 2), 5 vol.% (Layer 3) for the water content; 50 Ωm (Layer 1), 5 Ωm (Layer 2), 50 Ωm (Layer 3) for the resistivity and 25 m layer thickness for the 1st and 2nd layer.

The rms regarding the resistivity remains constant for larger resistivities, i.e. the MRS data do not change if the resistivity is larger than a certain value. This cut-off value depends on the layer depth, i.e. on the layer number, but also on the water content as a scaling factor. Additionally, the cut-off value is different for amplitude and phase of the MRS data. The resistivity of the first layer causes the largest influence on the rms, especially on the rms of the phase. The resistivity of the underlying half-space (3rd layer) is less effective, i.e. it is less reliably determined than the resistivities of the first and second layer.

The layer thickness is determined in the SA amplitude inversion, therefore only the values for rms_{Ampl} are depicted. A wrong layer thickness of the first layer causes a larger rms error than the same layer thickness used for the second layer.

To investigate equivalence models, Figure 6.16 shows contour plots of the rms, now changing water content and resistivity of each layer. Thus, two parameters are changed while the other six parameters remain the same. Figure 6.16 shows that the equivalence models can be narrowed down by using real and imaginary part of the MRS data compared to using only the amplitude. The number of equivalence models depends on the layer depth and the layer resistivity.

Model 2 - high resistive aquifer

The inversion scheme was also successfully applied on data calculated for a high resistive (500 Ωm) aquifer. Analogously to model 1, model 2 consists of a 25 m thick layer with 50 Ωm and 5 vol.%, now the aquifer has 500 Ωm and 30 vol.%, and the third layer again 50 Ωm and 5 vol.% (see Tab. 6.1). The calculated amplitude and phase values are drawn as black circles in Figures 6.17 and 6.18 using a circular loop ($d = 100$ m) as coincident transmitter and receiver.

The inversion result using only the amplitude is shown in Figure 6.17. Water content and layer thickness are excellently revealed. The resistivity of the first layer is well determined, but the resistivities of layer 2 and 3 are only roughly estimated.

Again, the inversion result can be improved using amplitude and phase for determining water content and resistivity in the LS inversion (Fig. 6.18). Thereby, the water content distribution as well as the resistivity of the first and second layer are well determined. The estimated resistivity of the second layer is close to the original value.

The sensitivity of the MRS data in terms of rms for amplitude and phase is shown in Figure 6.19. The rms errors are calculated using Equations 6.11, 6.12 and 6.13. Again, only one parameter is changed when calculating the rms.

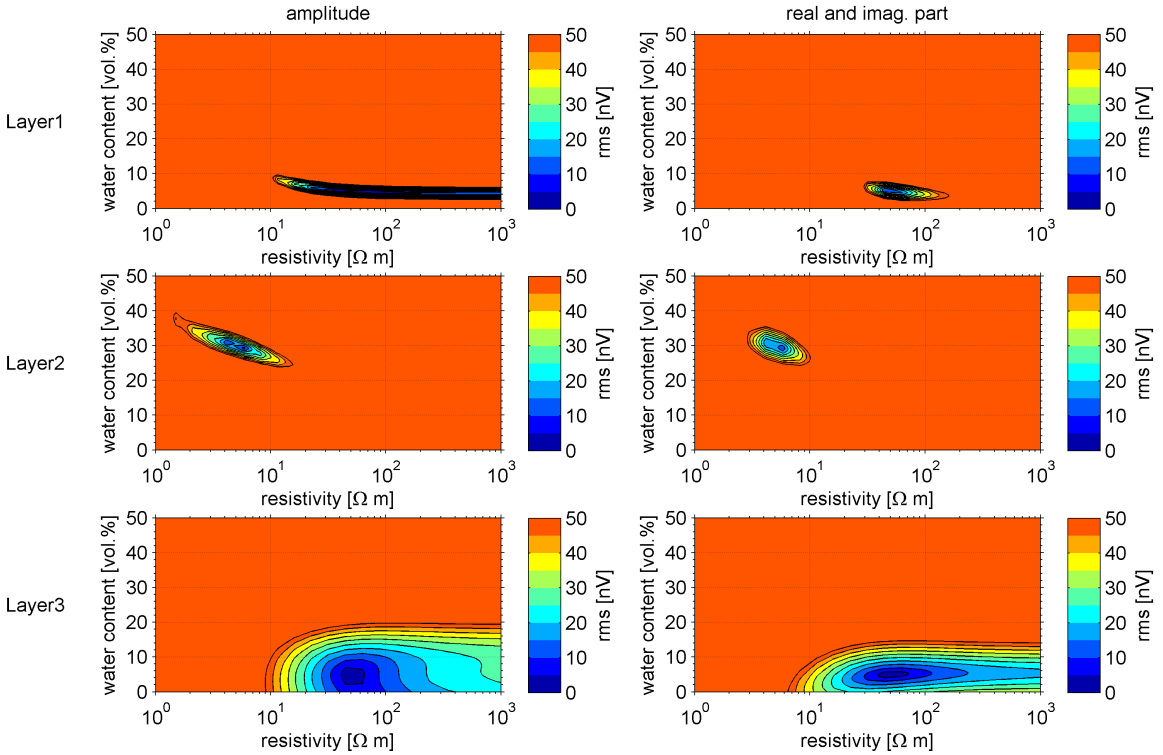

Figure 6.16.: Model 1 - Equivalence models of the inversion result in terms of rms for amplitude as well as real and imaginary part of the three layers. Model parameters are: Layer 1 (25 -50 m): 5 vol.%, 50 Ωm; Layer 2 (25 -50 m): 30 vol.%, 5 Ωm; Layer 3 (50 m - ?): 5 vol.% 50 Ωm.

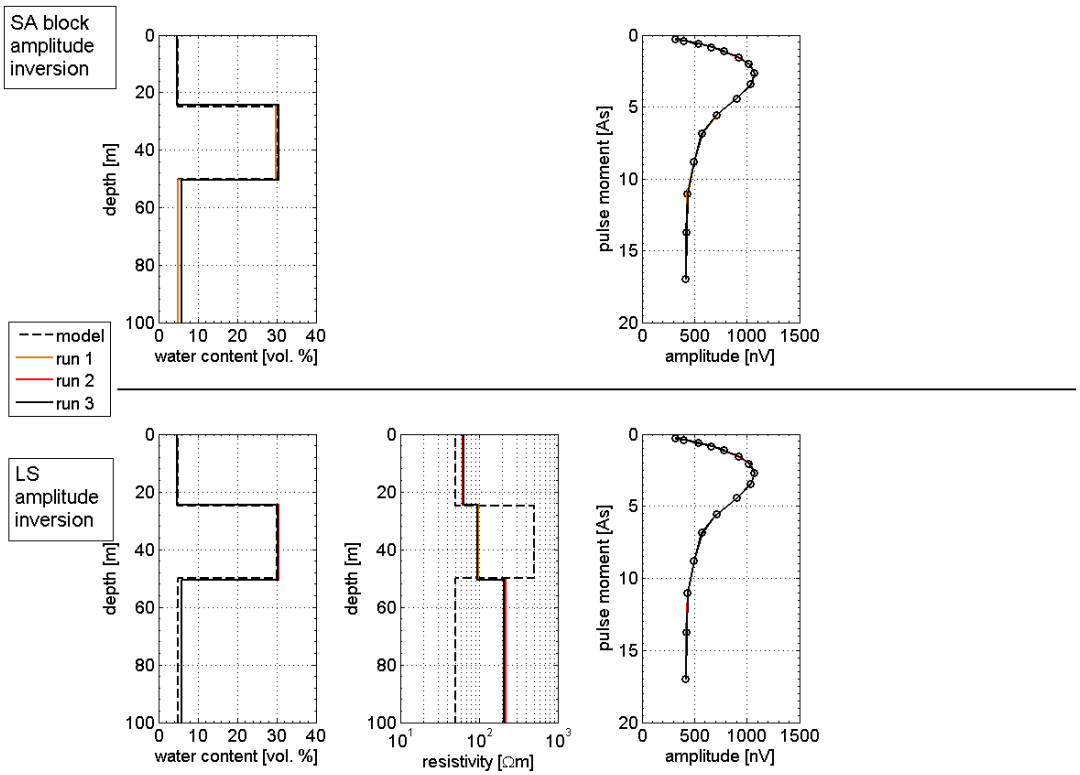

Figure 6.17.: Model 2 - Inversion scheme is applied on synthetic noise free data using a 3-layer model with the aquifer (500 Ωm, 30 vol.%; surrounding 50 Ωm, 5 vol.%) between 25 and 50 m. The data are calculated using a circular loop (d = 100 m) and magnetic field intensity of 48000 nT and 60°N inclination. Inversion results using only the amplitude for SA and LS inversion.

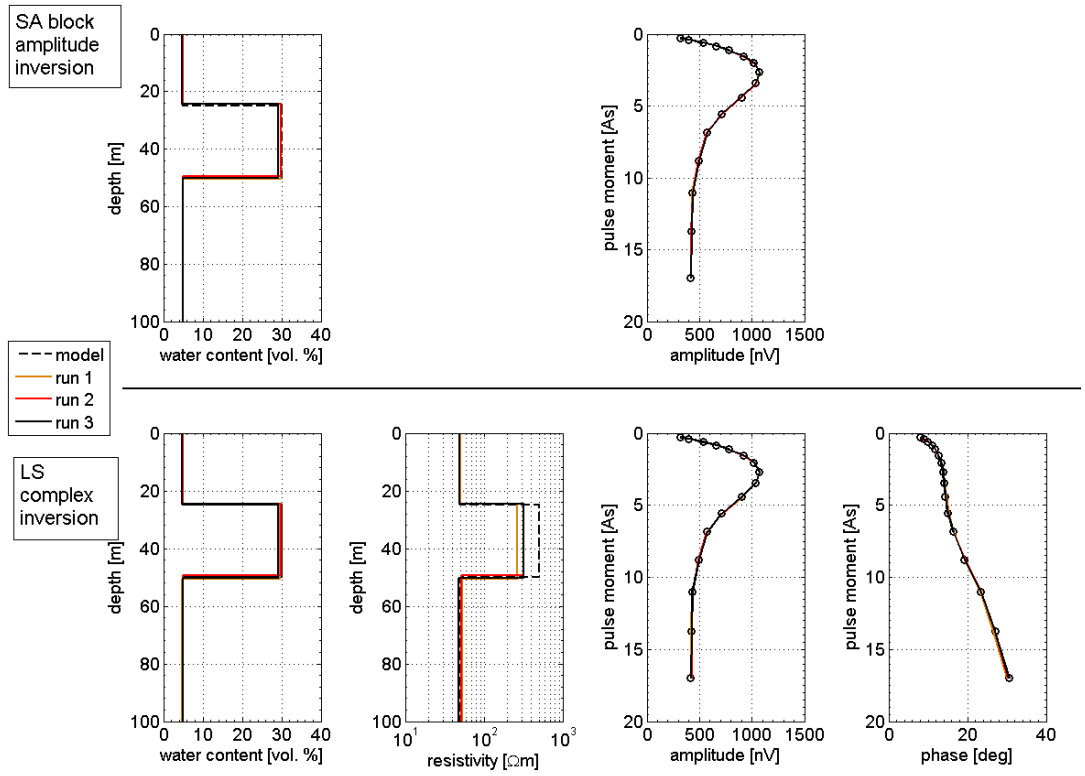

Figure 6.18.: Model 2 - Inversion scheme is applied on synthetic noise free data using a 3-layer model with the aquifer (500 Ωm, 30 vol.%; surrounding 50 Ωm, 5 vol.%) between 25 and 50 m. The data are calculated using a circular loop (d = 100 m) and magnetic field intensity of 48000 nT and 60°N inclination. Inversion results using only the amplitude for SA inversion, but using amplitude and phase (complex inversion) for the LS inversion.

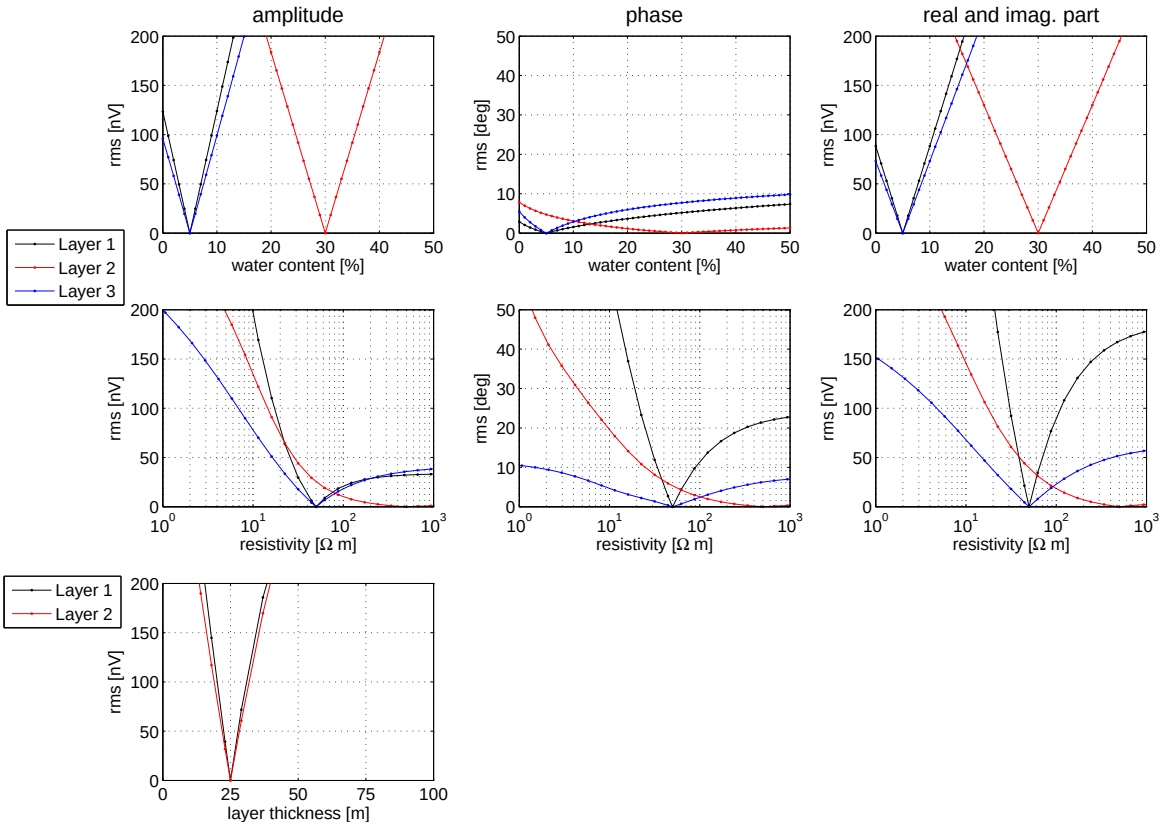

Figure 6.19.: Model 2 - Sensitivity of the inversion result in terms of rms for amplitude, phase as well as real and imaginary part for the eight inversion parameters. Model parameters are: 5 % (Layer 1), 30 % (Layer 2), 5 % (Layer 3) for the water content; 50 Ωm (Layer 1), 500 Ωm (Layer 2), 50 Ωm (Layer 3) for the resistivity and 25 m layer thickness for the 1st and 2nd layer.

Similar to model 1, the rms of the amplitude depends linearly on the water content. However, the rms for the same amount of water content of the third layer is significantly larger than in model 1.

The rms of the amplitude regarding the resistivity is the largest for the first layer. The rms of the phase has a clear minimum for the first and third layer at the modelled value. The rms curve changing the resistivity in the second layer has a broad minimum; the rms does not change for resistivities larger than 300 Ωm. So, using also the phase in the inversion, the resistivity of the first and third layer can be excellently resolved. The sensitivity regarding the highly resistive second layer is reduced (see inversion result in Fig. 6.18).

To investigate equivalence models, Figure 6.20 shows contour plots of the rms, now changing water content and resistivity of each layer. Thus, two parameters are changed while the other six parameters remain the same.

Figure 6.20 shows that the equivalence models can be narrowed down, especially concerning the resistivity, by using real and imaginary part of the MRS data compared to using only the amplitude. The number of equivalence models depends on the depth and the resistivity of the layer.

The sensitivities of model 2 differ significantly from those of model 1, i.e. the resistivity distribution affects also the sensitivity concerning water content and layer depth. This is due to the larger penetration depth having a resistivity of 500 Ωm in model 2. The contour plots of the 1D kernel function of model 1 (Fig. 6.21 top) and model 2 (Fig. 6.21 bottom) illustrate the different penetration depths. Due to the lower resistivity of model 1, the real part is attenuated but the imaginary part of the kernel function increases in the depth interval of between 25 and 50 m.

In this chapter, I have introduced a new inversion scheme for MRS soundings that can determine water content and resistivity for horizontal layers without any a priori information.

For model 1 (low resistive aquifer) the inversion using only the amplitude has shown that the determination of the water content is significantly improved when an appropriate resistivity distribution is used. This can be derived by an inversion without any a priori information. Having a more resistive aquifer (model 2), the resistivity distribution of the subsurface is less important for determining the water content using an amplitude inversion.

It is possible to use only the amplitude to derive water content and resistivity distribution. The inversion result of the resistivity is more reliable for a low resistive subsurface. The inversion result can be significantly improved by also using the phase

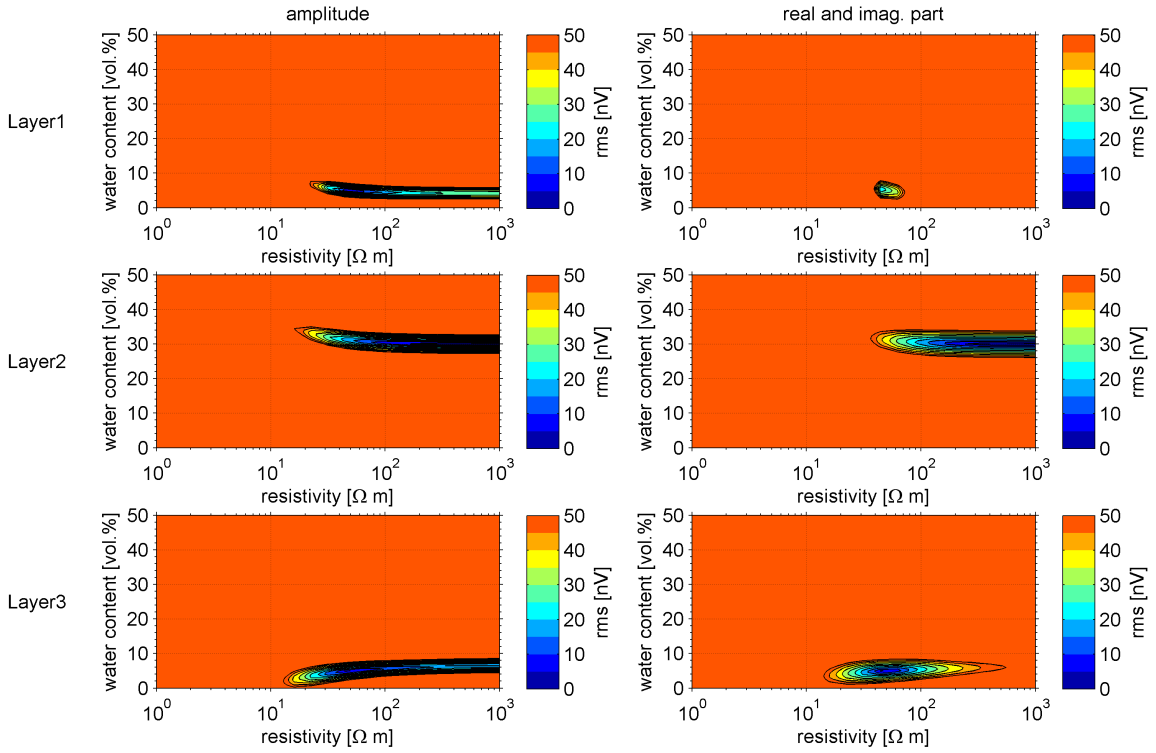

Figure 6.20.: Model 2 - Equivalence models of the inversion result in terms of rms for amplitude as well as real and imaginary part of the three layers. Model parameters are: Layer 1 (25 -50 m): 5 vol.%, 50 Ωm; Layer 2 (25 -50 m): 30 vol.%, 500 Ωm; Layer 3 (50 m - ?): 5 vol.% 50 Ωm.

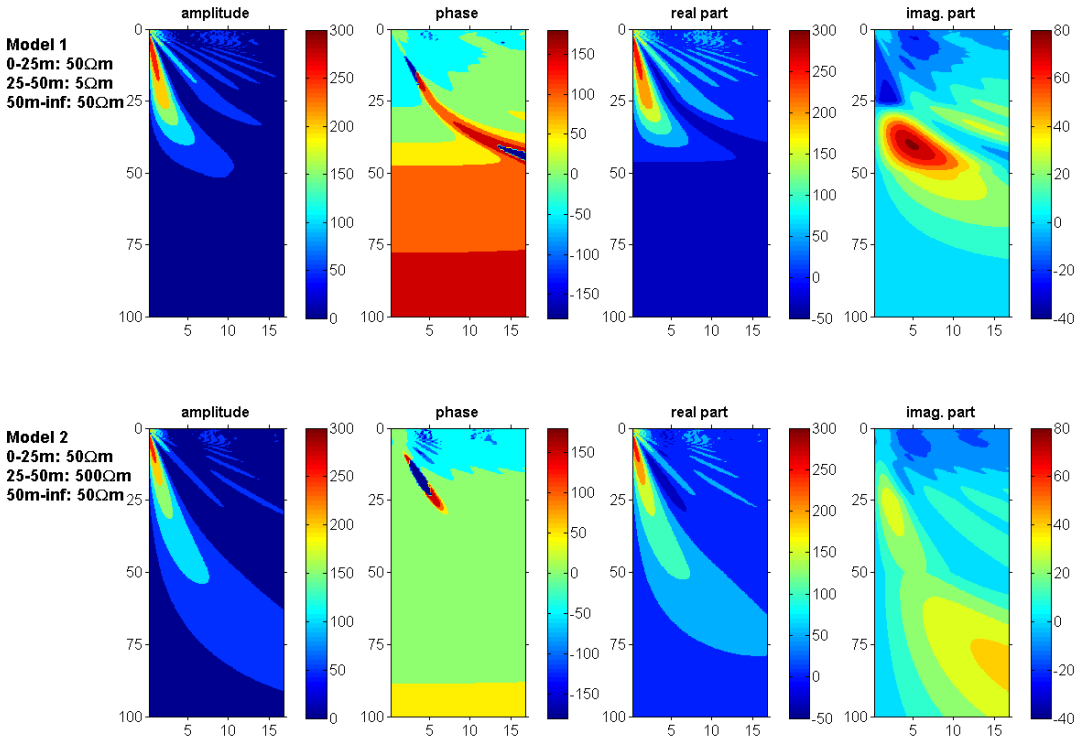

Figure 6.21.: Contour plot of the amplitude, phase, real part and imaginary part of the 1D MRS kernel function for model 1 (top) and model 2 (bottom). Units are nV/m for the amplitude, real part and imaginary part and deg/m for the phase, respectively. The data are calculated using a circular loop (d = 100 m) and magnetic field intensity of 48000 nT and 60°N inclination.

in the inversion. Thereby, the water content as well as the resistivity distribution is better and more reliable determined even for a more resistive subsurface.

7. Field data

After the assessment of the resistivity effect on modelling and inversion, the impact of the resistivity is demonstrated on field data.

7.1. France

In co-operation with the french geological survey (BRGM), MRS data, accompanied by DC resistivity measurements, were collected at the test site St-Cyr-en-Val near Orléans, France. The test site consists of an area where 1D conditions can be assumed as well as of an area with 2D or even 3D subsurface conditions.

7.1.1. Modelling of 2D resistivity and water content

Figure 7.1 shows the resistivity section at the 2D area at the French test site St-Cyr-en-Val. The subsurface is characterised by a low resistive zone (around 5 Ωm) in a medium resistive environment (around 50 Ωm). The geological interpretation is a clay lens in a sandy aquifer.

The measured MRS data are shown in Figure 7.2a. The data quality is limited due to a nearby gas pipeline. For convenience of comparison, the measured MRS phase is

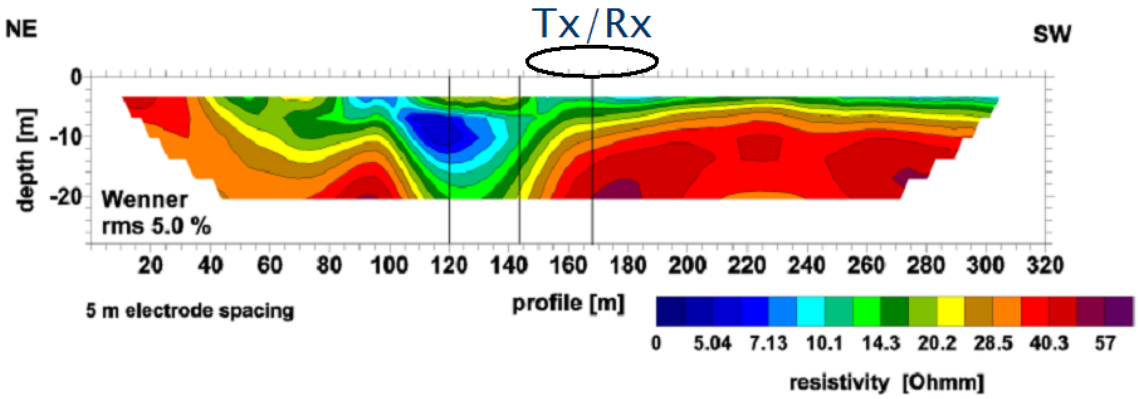

Figure 7.1.: Resistivity section at the 2D area of St-Cyr-en-Val near Orléans, France.

shifted and rotated by 180°. The subsurface models are deduced from the 2D resistivity section and from a priori information of this test site. I used two resistivity models for the forward calculation: electrically homogeneous with a medium resistivity of 50 Ωm and a 2D resistivity model (Fig. 7.2b). The 2D water content model remains the same for both forward calculations (Fig. 7.2c).

There is a significant deviation using the different resistivity models. Considering the 2D resistivity along with the 2D water content (diamonds in Fig. 7.2a) can explain much better the measured data compared to the data using an electrically homogeneous subsurface with a 2D water content distribution (triangles in Fig. 7.2a).

The remaining deviation between the measured and forward calculated data are due to the simplified subsurface models and due to effects resulting from a 3D geometry of the anomaly.

7.1.2. 1D inversion regarding resistivity and water content

The inversion scheme as introduced in Section 6 has been applied on field data. Analogously to the synthetic data, an electrically homogeneous half-space with a resistivity of 100 Ωm has been used as start value for the amplitude inversion.

The number of allowed layers is preset in the block inversion. Changing them allows to study their influence. Figure 7.3 shows the inversion results for a number of layers in the subsurface between two and seven. Each plot displays the inversion result after five inversion runs with the best fit of the amplitude of the LS inversion. The most significant change of the data fit, expressed by the relative rms error of the amplitude in the lower right corner of each plot, happens at a number of five layers. Using a greater number of layers, neither the data fit nor the inversion result changes significantly.

The relative rms error is calculated as

$$\mathrm{rms}_{rel} = \frac{1}{\sqrt{N}} \sqrt{\sum_{i=1}^{N} \left(\frac{E_{0meas,i} - E_{0cal,i}}{E_{0meas,i}} \right)^2} \cdot 100, \tag{7.1}$$

where the vector E_{0meas} contains the measured data, E_{0cal} the forward calculated data and N is the number of pulse moments. The measured and the forward calculated data can be expressed as amplitudes, phases, real or imaginary parts.

Figure 7.4 shows the measured MRS data as well as the MRS inversion result for water content and resistivity as well as the resistivity estimated from a 2D section of a DC

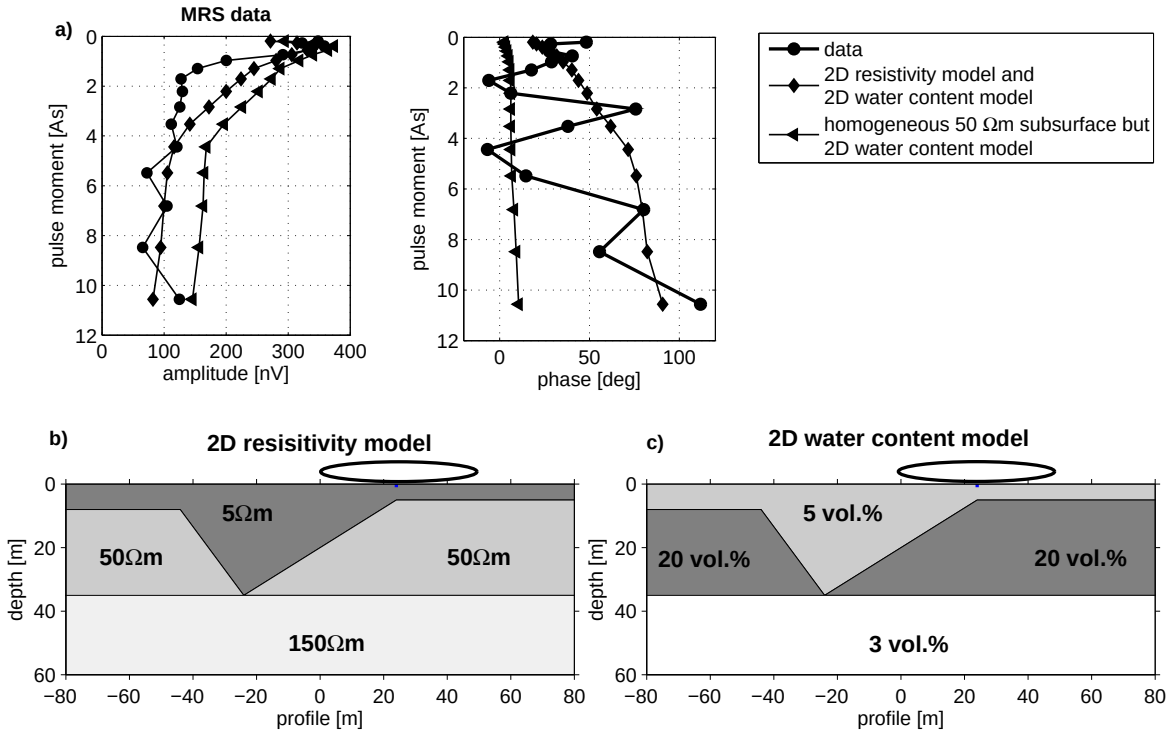

Figure 7.2.: a) Measured data (circles) and calculated data (diamonds) assuming a 2D electrical conductivity and water content distribution as well as calculated data (triangles) assuming an electrical homogeneous subsurface of 50 Ωm but a 2D water content distribution. MRS data are measured using a circular loop (d = 48 m, 2 turns), magnetic earth's field 47323.9 nT and 63°N inclination, test site St-Cyr-en-Val, France. b) 2D resistivity and c) 2D water content subsurface models used for the forward calculated data shown in a).

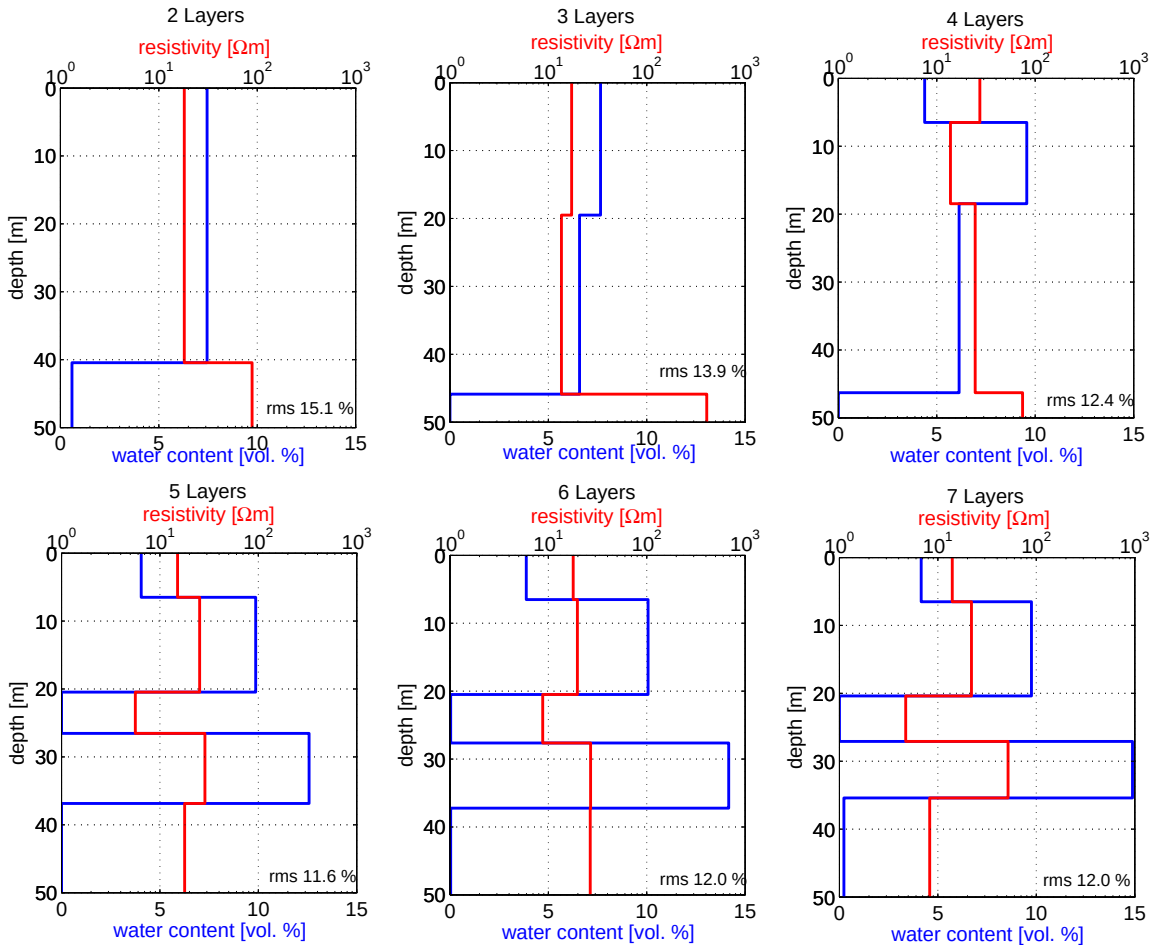

Figure 7.3.: Inversion results of the 1D block inversion of water content and resistivity between two and seven layers. Test site St-Cyr-en-Val, France.

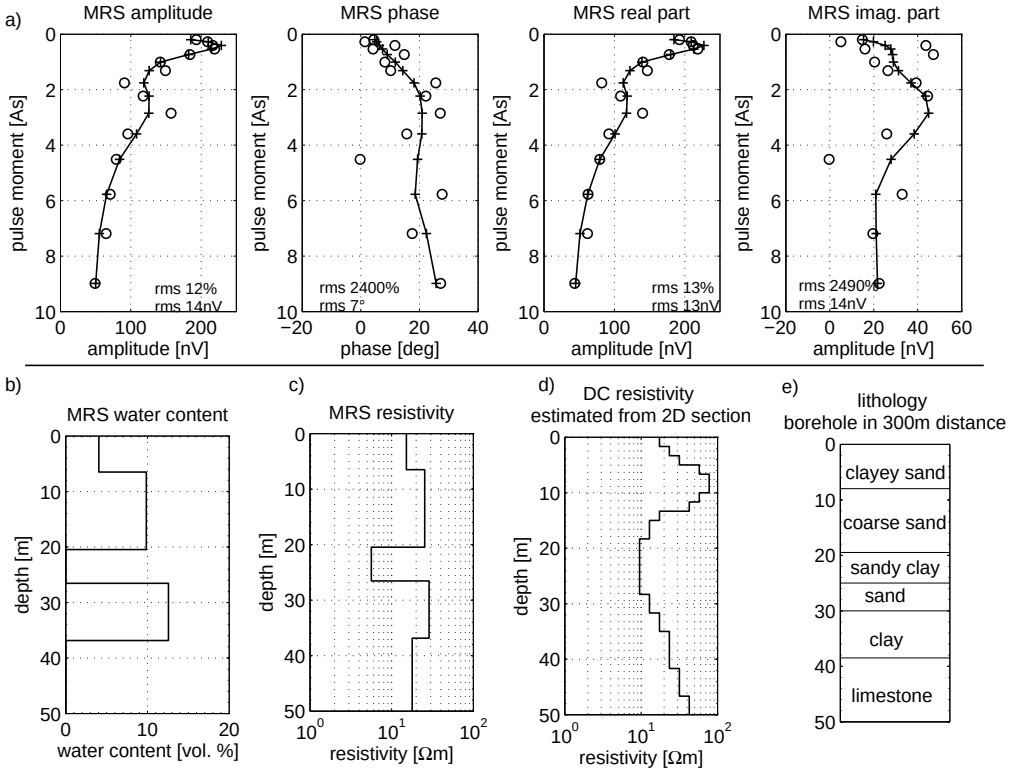

Figure 7.4.: a) MRS field data from the 1D area at the test site St-Cyr-en-Val (France). The data are measured with a circular loop ($d = 48$ m, 2 turns). Magnetic field intensity 47324 nT, 63°N inclination. Inversion result from the MRS data for b) water content and c) resistivity. d) Resistivity estimated from a 2D section of a DC geoelectric measurement. e) Lithology from a borehole in 300 m distance.

geoelectric measurement at the same site (Boucher et al., 2005). Additionally, there is the lithology from a borehole in 300 m distance.

The high relative rms error of the phase and the imaginary part is due to one outlier with a value close to zero. Therefore, also the absolute rms is depicted. The inversion determines a water content of 10 vol.% for the first aquifer and of 12 vol.% for the second aquifer. No water is determined neither for the intermediate sandy clay layer nor for the underlying half space. The resistivity determined from MRS is 25 Ωm for the aquifers. The sensitivity of the MRS is reduced for layers with a low water content. However, the resistivity of the sandy clay layer is reliable determined between 4 and 8 Ωm (see Fig. 7.3 bottom row). The resistivity of the underlying half-space cannot be determined reliable from MRS (see Figs. 7.5 and 7.6). The resistivities derived from MRS are comparable to those derived from DC geoelectric.

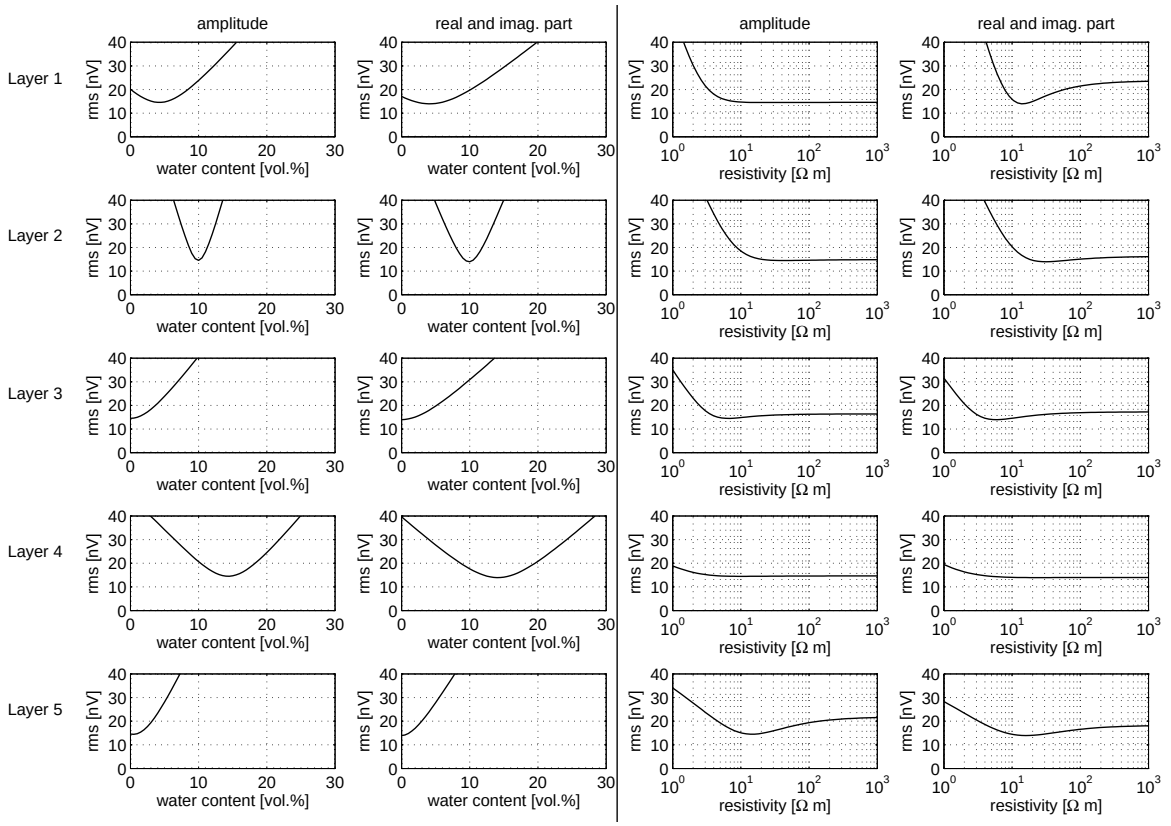

Figure 7.5.: Reliability of the inversion result in terms of rms for amplitude as well as real and imaginary parts. Inversion result (Fig. 7.4b) is: Layer 1 (0 - 6.5 m): 4 vol.%, 15 Ωm; Layer 2 (6.5 - 20.4 m): 10 vol.%, 25 Ωm; Layer 3 (20.4 - 26.5 m): 0.0 vol.%, 6 Ωm; Layer 4 (26.5 - 38.9 m): 13 vol.%, 29 Ωm; Layer 5 (38.9 m-?): 0.0 vol.%, 18 Ωm.

The reliability of the inversion result is estimated by calculating the rms of amplitude as well as real and imaginary parts (see Equations 6.11 and 6.13) for each layer.

In Figure 7.5 the rms is studied by changing one subsurface parameter (water content or resistivity) in the respective layer. In Figure 7.6, contour plots demonstrate the change of both subsurface parameters (water content and resistivity) in the respective layer.

Figure 7.5 and 7.6 indicate that the water content, as main target of investigation, is the more reliable determined subsurface parameter. However, the resistivity can be determined at least within one order of magnitude. The accuracy is better for shallow layers (Layer 1) and for a low resistive layer (Layer 3).

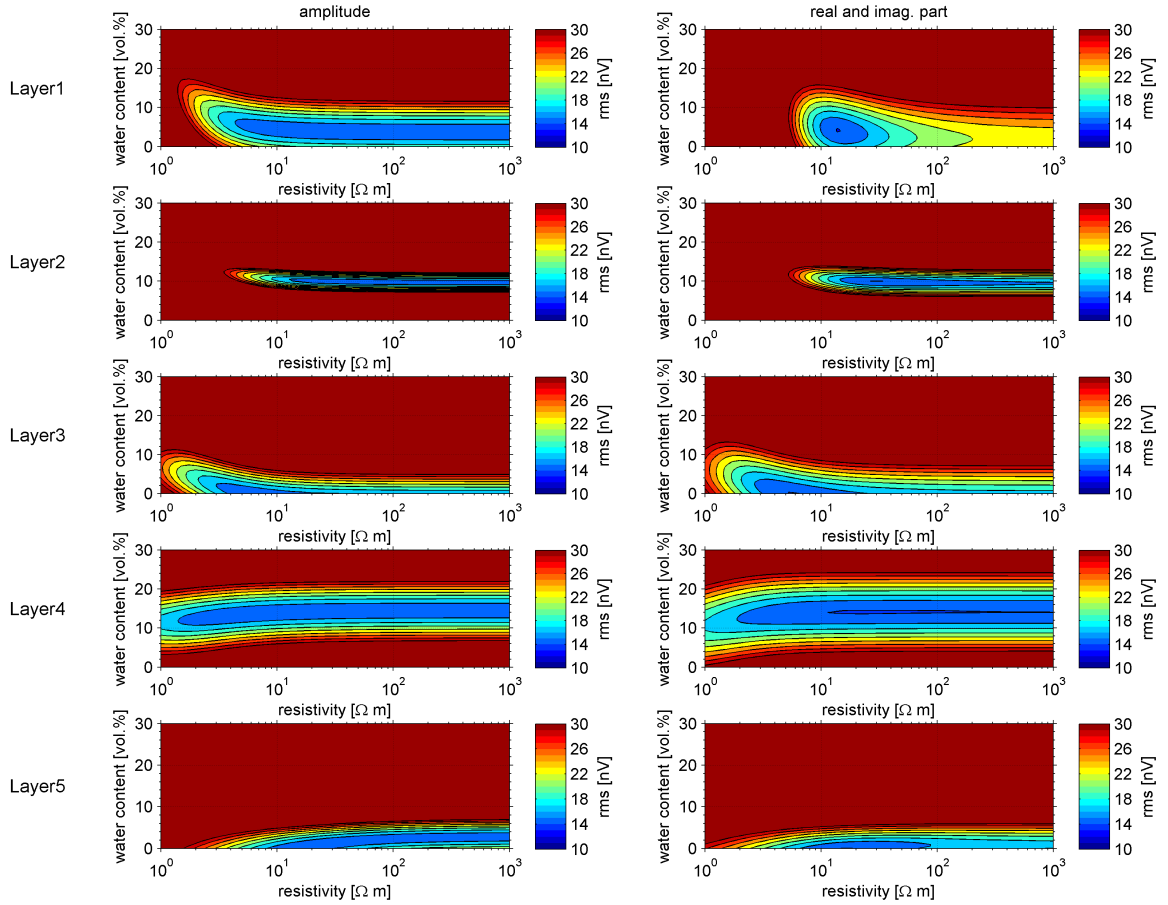

Figure 7.6.: Contour plots of the rms for amplitude as well as real and imaginary parts changing water content and resistivity of one layer. The inversion result (Fig. 7.4b) is: Layer 1 (0 - 6.5 m): 4 vol.%, 15 Ωm; Layer 2 (6.5 - 20.4 m): 10 vol.%, 25 Ωm; Layer 3 (20.4 - 26.5 m): 0.0 vol.%, 6 Ωm; Layer 4 (26.5 - 38.9 m): 13 vol.%, 29 Ωm; Layer 5 (38.9 m-?): 0.0 vol.%, 18 Ωm.

7.2. Israel

MRS data collected at the Dead Sea coastal area of Israel is used as second example for the successful implementation of the introduced inversion scheme. The goal of the geophysical survey was a better understanding of the process of sinkhole development caused by the fresh water flow towards the Dead Sea (Legchenko et al., 2006b; Ezersky et al., 2006). At the investigation area Nahal Hever south, the subsurface is composed of alluvial fan deposits down to a depth of about 20 m, then a 5 m thick clay layer and a 10 m thick salt layer. The salt layer is underlain by clay and gravel. Further investigations of the area have shown that the salt is partly dissolved. Thus, the aquifer is interpreted as water filled karst within the salt layer (Legchenko et al., 2006a).

Generally, the 3D effects of a karst structure must be taken into account when interpreting the MRS data. However, the station MRS 6 is located over the karst zone, and the karst can be approximated as 1D structure.

Figure 7.7 shows amplitude and phase of the MRS data along with the inversion result for water content and resistivity. Additionally, it displays the resistivity information obtained from a TEM measurement and the lithology from a borehole in 100 m distance to the midpoint of the MRS loop. A detailed map of the investigation area can be found in Legchenko et al. (2006a). The MRS data are measured using a square loop with an edge length of 100 m. For numerical reasons, the forward calculation in the inversion approximates a square loop with a circular loop using an equivalent area, i.e. a circular loop with a diameter $d = 112.8$ m.

The data are inverted as described in Section 6.3.1 using only the amplitude for determining the thickness of the layers and using amplitude and phase for determining water content and resistivity using the fixed layer depths. Five inversion runs are conducted with three layers. Start values of the resistivity of 1, 10 and 100 Ωm are used in the inversion. Figure 7.7 shows the inversion result with the smallest rms of the amplitude of the LS inversion for a start value of the resistivity of 1 Ωm.

The MRS inversion result is in excellent agreement with the lithology of the borehole. The resistivity of the MRS is comparable to those derived from TEM measurement. The resistivity of the third layer is less reliable due to the low water content and the reduced resolution with higher depths (see Figs. 7.8 and 7.9).

Again, the reliability of the inversion result is studied by changing one subsurface parameter (water content or resistivity) in the respective layer and calculating the resulting rms error (Fig. 7.8). In Figure 7.9, contour plots demonstrate the change of both subsurface parameters (water content and resistivity) in the respective layer.

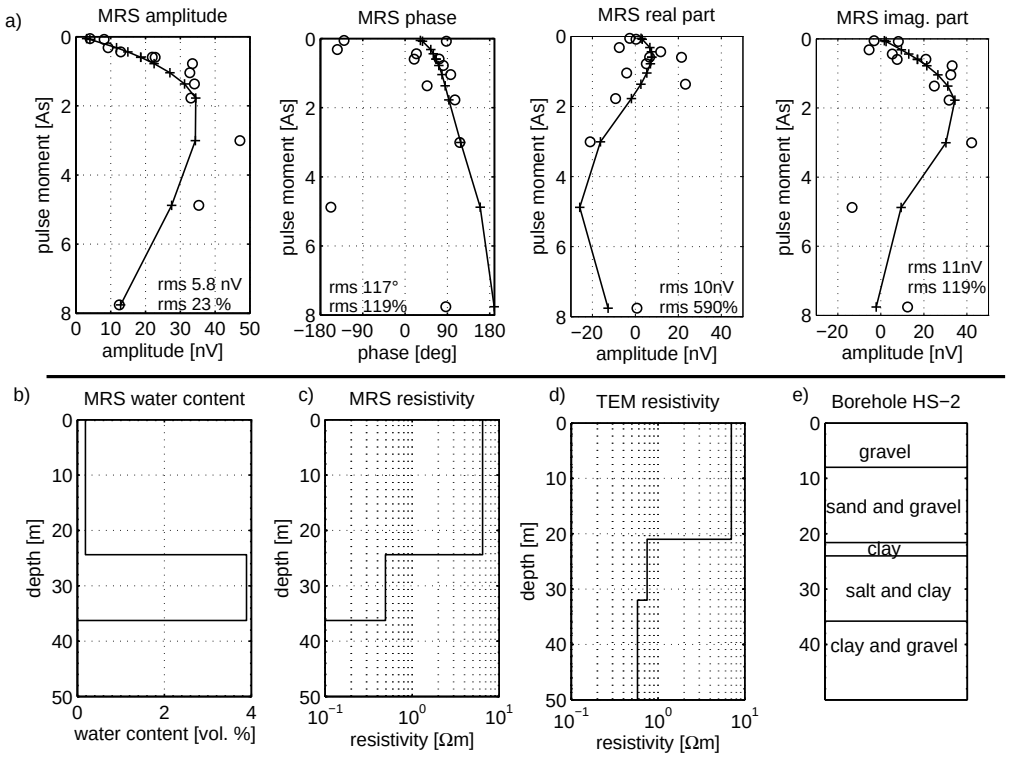

Figure 7.7.: a) MRS field data at station MRS 6 from Israel. The data are measured with a 100 x 100 m^2 square loop. Magnetic field intensity 44247 nT and 30°N inclination. Inversion result from the MRS data for b) water content and c) resistivity. d) Resistivity from TEM measurement. e) Lithology from a borehole in 100 m distance to the midpoint of the MRS loop.

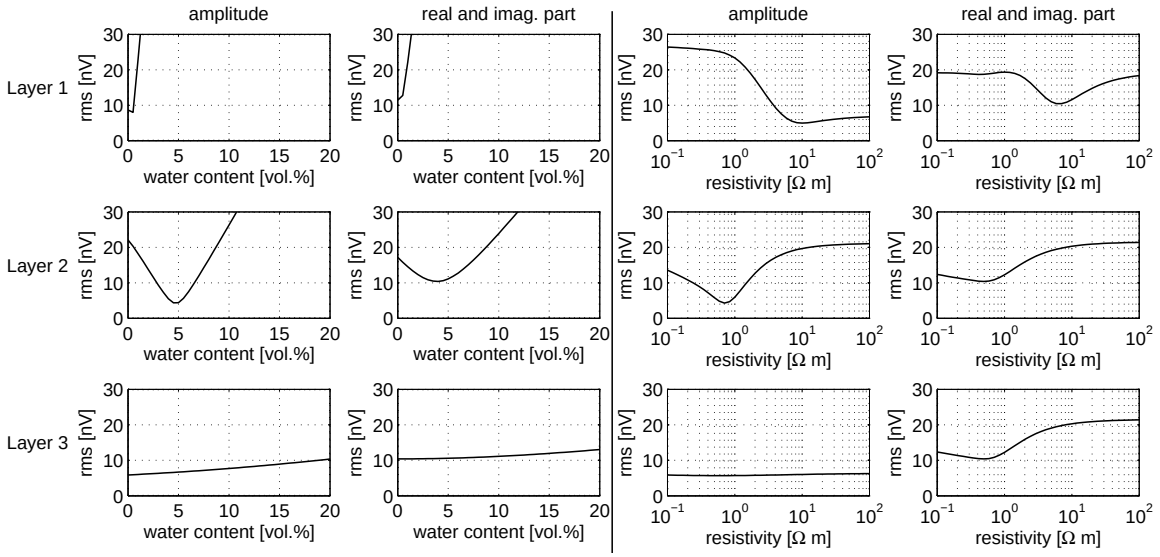

Figure 7.8.: Reliability of the inversion result in terms of rms for amplitude as well as real and imaginary parts. Inversion result (Fig. 7.7b) is: Layer 1 (0 - 24.4 m): 0.02 vol.%, 6 Ωm; Layer 2 (24.4 - 36.3 m): 4 vol.%, 0.5 Ωm; Layer 3 (36.3 m - ?): 0.0 vol.%, 0.1 Ωm.

The resistivity of the first layer can be reliable determined between 6 and 9 Ωm, the resistivity of the second layer is determined in the range of 0.2 and 1 Ωm. The water content of the aquifer is estimated between 3 and 5 vol.%. Due to the very low resistivity of the second layer, neither water content nor resistivity can be reliable determined for the third layer.

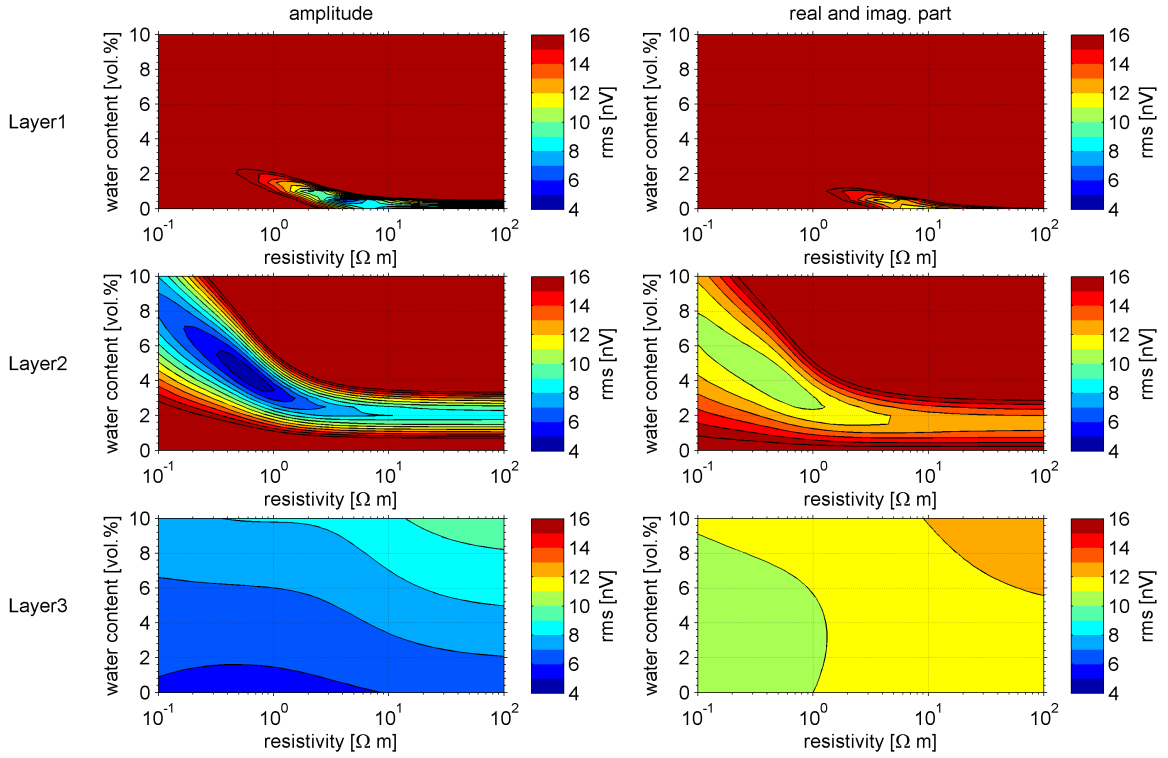

Figure 7.9.: Contour plots of the rms for amplitude as well as real and imaginary parts changing water content and resistivity of one layer. The inversion result (Fig. 7.7b) is: Layer 1 (0 - 24.4 m): 0.02 vol.%, 6 Ωm; Layer 2 (24.4 - 36.3 m): 4 vol.%, 0.5 Ωm; Layer 3 (36.3 m - ?): 0.0 vol.%, 0.1 Ωm.

8. Conclusions and Outlook

The main target of MRS investigation is the water content distribution in the subsurface. However, MRS is basically also an electromagnetic method in the frequency range of 800 - 3000 Hz. Thus, the resistivity of the subsurface has an important impact on the measured MRS data, too. Consequently, the resistivity must be considered when inverting the MRS data. Therefore, each MRS measurement must be accompanied by a geoelectric measurement, unless the a priori information suggests that the resistivity can be approximated as insulating with respect to the used loop size.

The extent of the resistivity impact depends on the MRS penetration depth. Using greater loop sizes or greater pulse moments, the penetration depth increases and thus, also the impact of the resistivity increases. There is an upper limit of the effective resistivity. Resistivities above this cut-off value do not affect the MRS signal.

The maximum effective resistivity is linked to the electromagnetic skin depth calculated for a plane wave. The skin depth, using a constant frequency, increases for increasing resistivity. Also the MRS maximum depth detection increases for increasing resistivity, using a constant pulse moment. However, there is an upper limit of the MRS depth detection determined by the loop size and by the maximum pulse moment used. The resistivity where the MRS maximum depth detection and the skin depth intersect can be used as a criterion to estimate the maximum effective resistivity.

As recently MRS is extended to 2D investigations, also the effect of 2D resistivity structures is studied, and it is compared to 1D laterally stratified subsurfaces. It has been shown that a 1D approximation is valid if the centre of the loop is in a distance of one loop diameter to the structure or if the extension of the structures is two loop diameters. The substitution of a 2D resistivity with a 1D equivalent layer model has been found impossible due to the different 2D sensitivities.

The essential part of this work is the realisation of a 1D inversion scheme for determining water content and resistivity from MRS. This is the basis for using MRS as stand-alone method. Also the determination of the water content is improved when using an appropriate resistivity model. Analysing the resistivity has shown the limitations of the inversion with regard to resistivities greater than a cut-off value depending

on the loop size and deeper layers. The maximum effective resistivity increases linearly with the loop size.

Finally, the achievements presented in this study are demonstrated on field data. It has been shown that it is essential to take the 2D resistivity along with a 2D water content into account. Additionally, the feasibility of the inversion scheme is shown on field data of two sites. The successful determination of the resistivity by MRS alone is demonstrated by comparing the resistivity derived from MRS with the resistivity derived from conventional methods like geoelectric and time domain electromagnetic.

Having the resistivity along with the water content distribution as inversion result, MRS gives an information about the mineralisation of the aquifer, and thereby, the quality of the aquifer can be estimated. This is of utmost interest for the further hydrogeological interpretation. This specific information cannot be achieved by geoelectrics alone, because of the nonuniqueness in resistivity concerning water content and mineralisation.

This study is confined on the initial amplitude and phase extrapolated to the time $t = 0$. The exponential decay of the MRS response and the corresponding decay time has not been investigated. In future studies the inversion approach presented in this work will be extended such that the time-decaying MRS signal of each pulse moment is taken into account in the inversion. By that, inversion parameters will be water content, resistivity and decay time distribution of the subsurface. Thus, information about the amount of water, the mineralisation of the water and the pore sizes of the water bearing layer, linking to the hydraulic conductivity, can be estimated from MRS measurements alone.

Besides the extension regarding the decay times, the inversion scheme can be also extended regarding the measurement dimension. The effects of 2D resistivity have been presented in this study for the forward modelling, a 2D MRS inversion regarding the water content has been already realised. Some efforts have been already done for a 2D inversion of water content and decay times. The final aim is a 2D inversion for determining water content, decay times and resistivity. Technical problems such as the long computation time of the excitation field may be overcome by sophisticated solvers or by technological progress in the future.

9. Acknowledgements

Many people contributed to this PhD thesis in innumerable ways, and I am grateful to all of them. First and foremost, I thank Prof. Dr. Ugur Yaramanci for supervising my work and for providing perfect working conditions. His ideas and encouragements contributed a lot to my work.

I am grateful to Prof. Dr. Anatoly Legchenko, who agreed to be the second referee of my PhD thesis. His valuable comments and critical questions greatly improved my work. Furthermore, I thank him for providing the data of the measurements in Israel.

I thank Gerhard Lange for many years of scientific cooperation and support in MRS application.

Special thanks to Dr. Marian Hertrich for the enjoyable team work, many fruitful discussions and successful days in the field.

Many thanks to Ines Rommel, Oliver Mohnke, Dr. Martin Müller, Mike Müller-Petke, Jürgen Schmalholz, Stephan Strehl and all other former and present colleagues at the Department of Applied Geophysics of the Technical University of Berlin for a great team work and a pleasant working atmosphere.

I thank Dr. Jean-François Girard and Marie Boucher for providing a priori information about the test site St-Cyr-en-Val.

Finally, I am grateful to my parents and my family for supporting me in many ways. I am deeply grateful to Alexander and our daughter Alina for their endless patience, love and support.

Bibliography

Becken, M., Burkhardt, H., 2004. An ellipticity criterion in magnetotellutic tensor analysis. Geophysical Journal International 159, 69–82.

Boucher, M., Girard, J., Legchenko, A., Baltassat, J., 2005. Éléments de méthodologie pour l´étalonnage de mesures de Résonance Magnétique Nucléaire (RMN) avec des données hydrodynamiques. Tech. rep., BRGM/RP-53666-FR.

Braun, M., 2002. Untersuchungen komplexwertiger Oberflächen-NMR Signale im leitfähigen Untergrund. Master's thesis, Technische Universität Berlin.

Braun, M., Hertrich, M., Yaramanci, U., 2002. Modelling of the phase behaviour in the SNMR signal. In: Proceedings of the 8th EEGS conference, Aveiro/Portugal. EEGS-ES.

Braun, M., Hertrich, M., Yaramanci, U., 2003. SNMR investigations with variable parameters and loop geometries - A comprehensive study. In: Proceedings of the 2nd International workshop on MRS, Orleans, France. pp. 137–140.

Braun, M., Hertrich, M., Yaramanci, U., 2005a. Study on complex inversion of magnetic resonance sounding signals. Near Surface Geophysics 3 (3), 155–163.

Braun, M., Rommel, I., Yaramanci, U., 2005b. Modelling of magnetic resonance sounding using finite elements (FEMLAB) for 2D resistivity extension. In: Proceedings der Femlab Konferenz 2005. No. ISBN 3-00-017211-4. pp. 191–196.

Braun, M., Rommel, I., Yaramanci, U., 2006. Influence of the electrical conductivity on Magnetic Resonance Sounding regarding 2D modelling and 1D inversion. In: 3rd international workshop on MRS, Madrid, Spain. pp. 49–52.

Braun, M., Yaramanci, U., 2003. Inversions of Surface-NMR signals using complex kernels. In: Proceedings of the 9th EEGS conference, Prague/Czech Republic. pp. O–49.

Braun, M., Yaramanci, U., 2006. 1D inversion of resistivity and water content of Magnetic Resonance Sounding. In: Proceedings of Near Surface 2006 - 12th European Meeting of Environmental and Engineering Geophysics, Helsinki, Finland. p. P016.

COMSOL, 2005. COMSOL Multiphysics User's Guide. COMSOL AB, COMSOL 3.2 Edition.

Corona, A., Marchesi, M., Martini, C., Ridella, S., 1987. Minimization multimodal functions of continuous variables with the simulated annealing algorithm. ACM Transactions on Mathematical Software 13 (3), 262–280.

Ezersky, M., Bruner, I., Keydar, S., Trachtman, P., Rybakov, M., 2006. Integrated study of the sinkhole development site on the Western shores of the Dead Sea using geophysical methods. Near Surface Geophysics 4, 335–343.

Girard, J. F., Legchenko, A., Boucher, M., August 2005. Stability of MRS signal and estimation of data quality. Near Surface Geophysics 3 (3), 187–194.

Hertrich, M., 2005. Magnetic resonance sounding with separated transmitter and receiver loops for the investigation of 2D water content distributions. Ph.D. thesis, Technical University of Berlin.

Hertrich, M., Braun, M., Yaramanci, U., 2005a. High resolution 2D inversion of separated loop magnetic resonance sounding (MRS) surveys. In: Proceedings of EAGE Near Surface 2005 Meeting, Palermo/Italy. EAGE, p. A021.

Hertrich, M., Braun, M., Yaramanci, U., 2005b. Magnetic resonance soundings with separated transmitter and receiver loops. Near Surface Geophysics 3 (3), 131–144.

Hertrich, M., Müller-Petke, M., Yaramanci, U., 2006. Potential of the application of magnetic resonance sounding to deep targets. In: 3rd international workshop on MRS, Madrid, Spain. pp. 41–44.

Iris Instruments, 2000. NumisPlus - Surface Proton Magnetic Resonance system for water prospecting. Reference Manual.

Legchenko, A., 2004. Magnetic Resonance Sounding: Enhanced Modeling of a Phase Shift. Applied Magnetic Resonance 25, 621–636.

Legchenko, A., Baltassat, J.-M., Beauce, A., Bernard, J., 2002. Nuclear magnetic resonance as a geophysical tool for hydrogeologists. Journal of Applied Geophysics 50 (1-2), 21–46.

Legchenko, A., Ezersky, M., Camerlynck, C., Al-Zoubi, A., Chalikakis, K., 2006a. MRS study of groundwater flow and its relationship with sinkholes developments in the dead sea coastal area. In: Proceedings of Near Surface 2006 - 12th European Meeting of Environmental and Engineering Geophysics, Helsinki, Finland. p. P015.

Legchenko, A., Ezersky, M., Girard, J.-F., Baltassat, J.-M., 2006b. Interpretation of MRS measurements in rocks with high electrical conductivity. In: 3rd international workshop on MRS, Madrid, Spain. pp. 45–48.

Legchenko, A., Shushakov, O., 1998. Inversion of surface NMR data. Geophysics 63 (1), 75–84.

Legchenko, A., Valla, P., 1998. Processing of surface proton magnetic resonance signals using non-linear fitting. Journal of Applied Geophysics 39, 77–83.

Levitt, M. H., 1997. The signs of frequencies and phases in NMR. Journal of Magnetic Resonance 126, 164–182.

Levitt, M. H., 2002. Spin Dynamics - Basics of Nuclear Magnetic Resonance. John Wiley & Sons, LTD.

Lubczynski, M., Roy, J., 2003. Hydrogeological interpretation and potential of the new magnetic resonance sounding (MRS) method. Journal of Hydrology 283, 19–40.

Mansfield, P., Maudsley, A., Morris, P., Pykett, I., 1979. Selective Pulses in NMR Imaging: A reply to Criticism. Journal of Magnetic Resonance 33, 261–274.

MATLAB, 2007a. Optimization Toolbox User's Guide. The MathWorks.

MATLAB, 2007b. Partial Differential Equation Toolbox User's Guide. The MathWorks.

McGillivray, P., Oldenburg, D., 1990. Methods for calculating Fréchet derivatives and sensitivities for the non-linear inverse problem: A comparative study. Geophysical Prospecting (38), 499–524.

Militzer, H., Weber, F. (Eds.), 1985. Angewandte Geophysik - Band 2. Springer-Verlag Wien / Akademie-Verlag Berlin.

Müller, M., Hertrich, M., Yaramanci, U., 2006. Analysis of magnetic resonance sounding kernels concerning large scale applications using SVD. In: Proceedings of SAGEEP, Seattle/USA.

Müller-Petke, M., Hertrich, M., Yaramanci, U., 2007. Optimization and resolution studies for Magnetic Resonance Sounding (MRS) using SVD. Journal of Applied GeophysicsSubmitted to special issue on MRS.

Mohnke, O., Yaramanci, U., 2002. Smooth and block inversion of surface NMR amplitudes and decay times using simulated annealing. Journal of Applied Geophysics 50 (1-2), 163–177.

Mohnke, O., Yaramanci, U., 2005. Forward modeling and inversion of MRS relaxation signals using multi-exponential decomposition. Near Surface Geophysics 3 (3), 165–185.

Rommel, I., 2006. The effect of the topography on Magnetic Resonance Tomography (MRT). Master's thesis, Technical University of Berlin.

Rommel, I., Hertrich, M., Yaramanci, U., 2006. The effect of topography on MRS measurements with separated loops. In: 3rd international workshop on MRS, Madrid, Spain. pp. 33–36.

Roy, J., Lubczynski, M., 2003. The magnetic resonance sounding technique and its use for groundwater investigations. Hydrogeology Journal 11, 455–465.

Roy, J., Lubczynski, M., November 2005. MRS multi-exponential decay analysis: aquifer poresize distribution and vadose zone characterization. Near Surface Geophysics 3 (4), 287–298.

Schirov, M., A. Legchenko, Creer, G., 1991. A new direct non-invasive groundwater detection technology for Australia. Exploration Geophysics 22, 333–338.

Shushakov, O., 1996. Groundwater NMR in conductive water. Geophysics 61 (4), 998–1006.

Trushkin, D., Shushakov, O., Legchenko, A., 1995. Surface NMR applied to an electroconductive medium. Geophysical Prospecting 43, 623–633.

Vouillamoz, J., Chatenoux, B., Mathieu, Baltassat, J., Legchenko, A., 2007. Efficiency of joint use of MRS and VES to characterize coastal aquifer in Myanmar. Journal of Applied Geophysics 61, 142–154.

Ward, S. H., Hohmann, G. W., 1988. Electromagnetic theory for geophysical applications. In: Nabighian, M. N. (Ed.), Electromagnetic methods in applied geophysics. Vol. 1 of Investigations in Geophysics. Soc. Expl. Geophys., Ch. 4, pp. 131–311.

Weichman, P. B., Lavely, E. M., Ritzwoller, M., 1999. Surface nuclear magnetic resonance imaging of large systems. Physical Review Letters 82 (20), 4102–4105.

Weichman, P. B., Lavely, E. M., Ritzwoller, M. H., 2000. Theory of surface nuclear magnetic resonance with applications to geophysical imaging problems. Physical Review E 62 (1, Part B), 1290–1312.

Weidelt, P., 2005. Geoelektrik Grundlagen. In: Knödel, K., Krummel, H., Lange, G. (Eds.), Handbuch zur Erkundung des Untergrundes von Deponien. Vol. 3 Geophysik. Springer-Verlag Berlin Heidelberg, pp. 71–100.

Yaramanci, U., Hertrich, M., 2006. Groundwater Geophysics. Springer-Verlag, Ch. 8 Magnetic Resonance Sounding, pp. 253–273.

Zimmerman, W., Hewakandamby, B., 2004. Partial differential equations and the finite element method. In: Zimmerman, W. (Ed.), Process Modelling and Simulations with Finite Element Methods. World Scientific Publishing Co., Ch. 2, pp. 63–105.

A. Appendix to Chapter 4.1

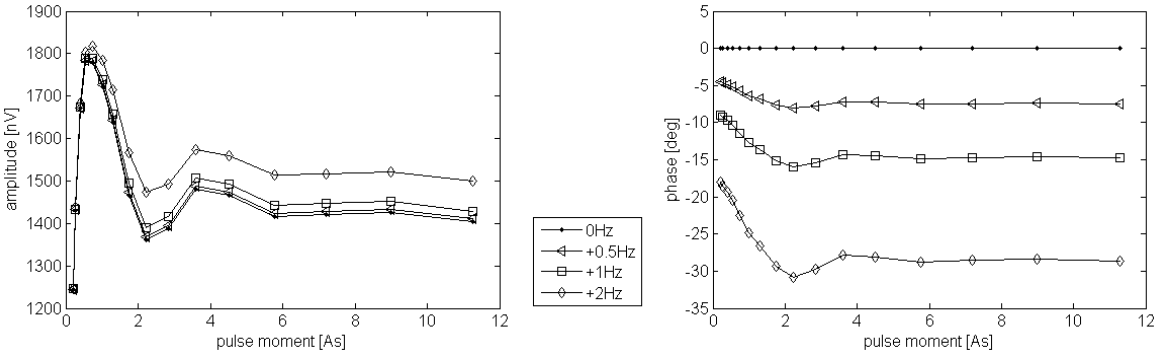

Figure A.1.: Effect of the frequency deviation between the clock frequency ($f_{\mathrm{rf}} = 2086.8$ Hz) and the measured Larmor frequency f_0. Data are calculated assuming a constant frequency offset and a resistive subsurface (1E6 Ωm) using a circular loop ($d = 50$ m), 100 vol.% water content, 60°N inclination, pulse length $\tau = 40.3$ ms.

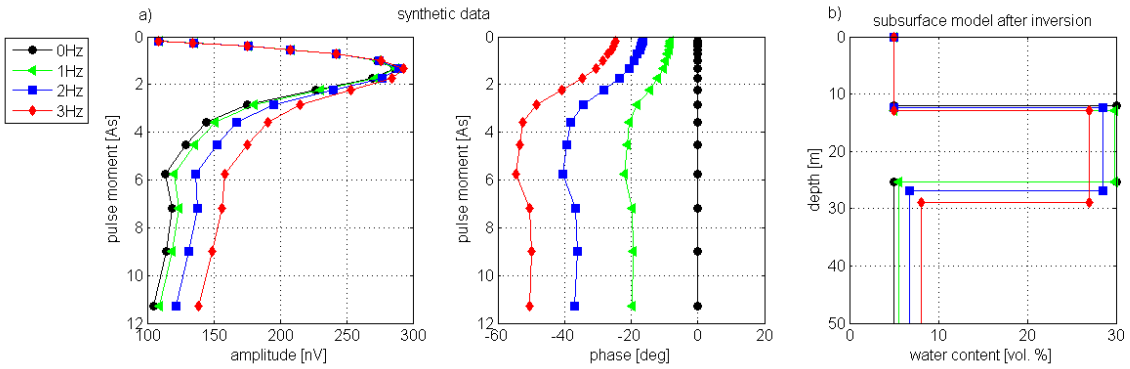

Figure A.2.: Effect of the frequency deviation between the clock frequency ($f_{\mathrm{rf}} = 2086.8$ Hz) and the measured Larmor frequency f_0 on the inversion result. a) Data are calculated assuming a constant frequency offset and a resistive subsurface (1E6 Ωm) using a circular loop ($d = 50$ m), 30 vol.% water content between 12 and 25 m, 5 vol.% in the surrounding, 60°N inclination, pulse length $\tau = 40.3$ ms. b) Inversions are conducted neglecting the frequency deviation. Only the amplitude is used for the inversion.

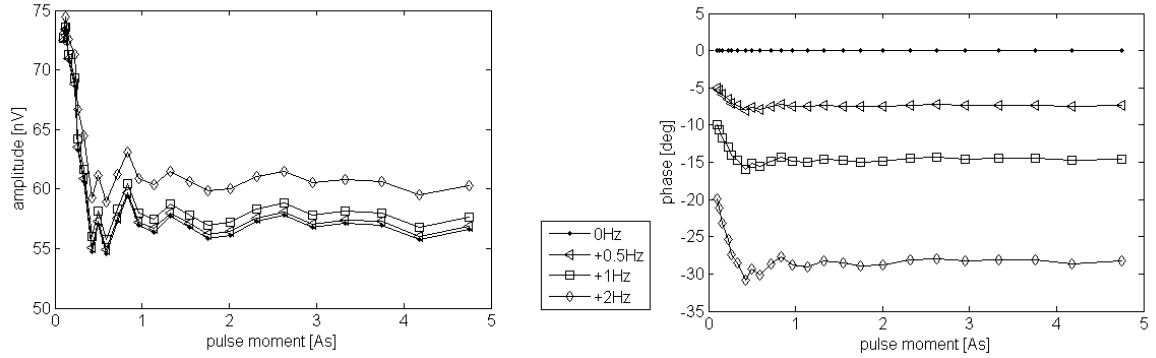

Figure A.3.: Effect of the frequency deviation between the clock frequency ($f_{\mathrm{rf}} = 2086.8$ Hz) and the measured Larmor frequency f_0. Data are calculated assuming a constant frequency offset and a resistive subsurface (1E6 Ωm) using a circular loop ($d = 10$ m), 100 vol.% water content, 60°N inclination, pulse length $\tau = 40.3$ ms.

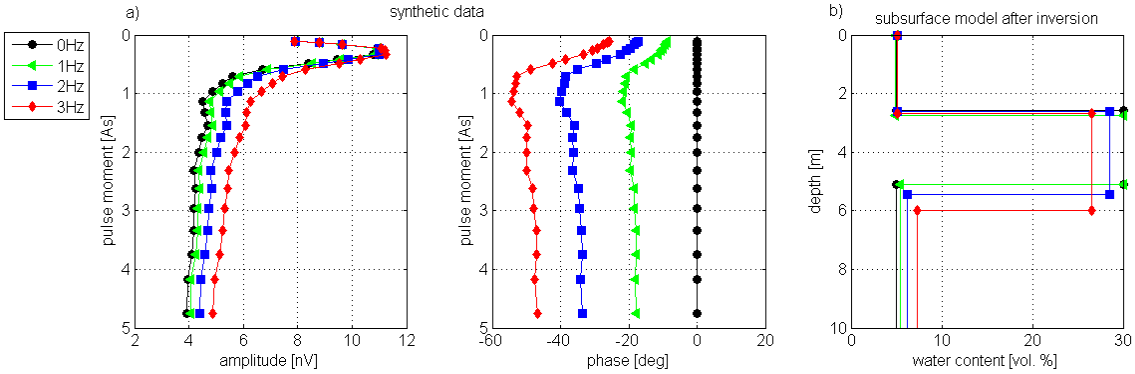

Figure A.4.: Effect of the frequency deviation between the clock frequency ($f_{\mathrm{rf}} = 2086.8$ Hz) and the measured Larmor frequency f_0 on the inversion result. a) Data are calculated assuming a constant frequency offset and a resistive subsurface (1E6 Ωm) using a circular loop ($d = 10$ m), 30 vol.% water content between 2.5 and 5 m, 5 vol.% in the surrounding, 60°N inclination, pulse length $\tau = 40.3$ ms. b) Inversions are conducted neglecting the frequency deviation. Only the amplitude is used for the inversion.

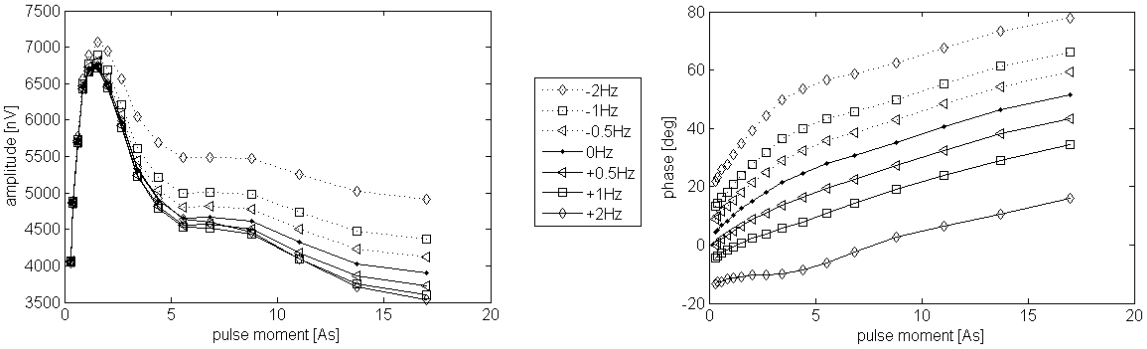

Figure A.5.: Effect of the frequency deviation between the clock frequency ($f_{\mathrm{rf}} = 2086.8$ Hz) and the measured Larmor frequency f_0. Data are calculated assuming a constant frequency offset and a conductive subsurface (50 Ωm) using a circular loop ($d = 100$ m), 100 vol.% water content, 60°N inclination, pulse length $\tau = 40.3$ ms.

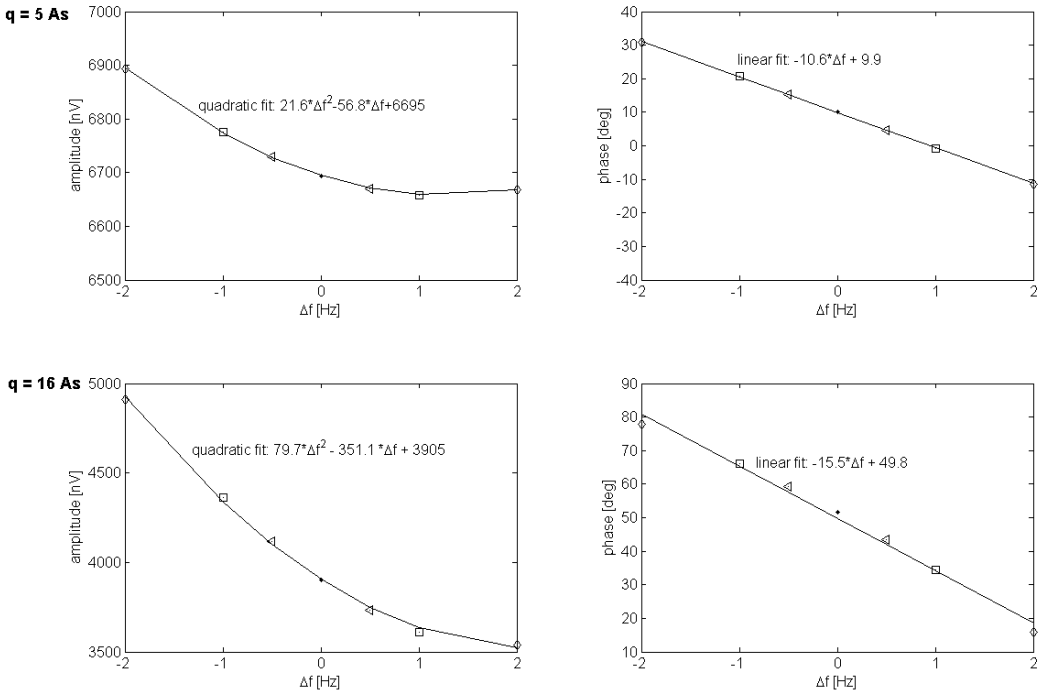

Figure A.6.: Amplitude and phase values versus frequency offset, exemplary for two pulse moments. The amplitudes can be described with a power law and the phase values with a linear fit. Data are calculated assuming a constant frequency offset and a conductive subsurface (50 Ωm) using a circular loop ($d = 100$ m), 100 vol.% water content, 60°N inclination, pulse length $\tau = 40.3$ ms.

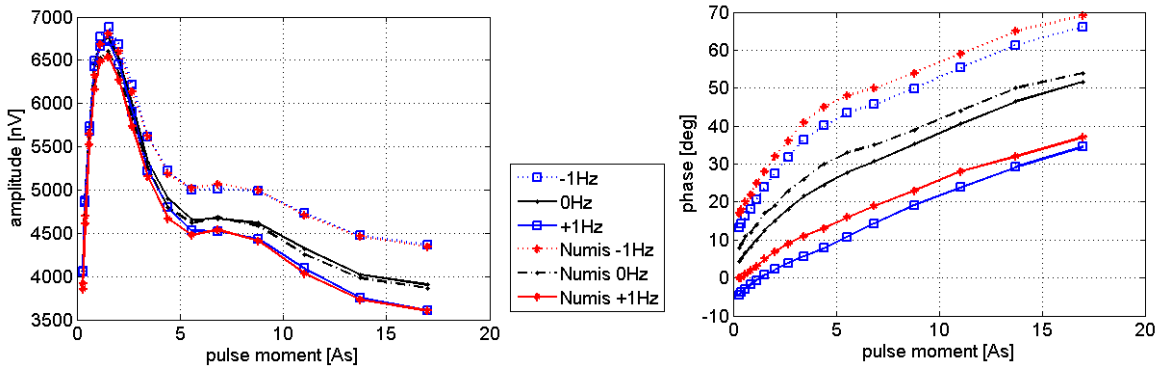

Figure A.7.: Effect of the frequency deviation between the clock frequency ($f_{\mathrm{rf}} = 2086.8$ Hz) and the measured Larmor frequency f_0. Comparison of the data calculated with my own algorithm and with the commercially available Numis programme MRS04_5.exe and Samogon. Data are calculated assuming a constant frequency offset and a conductive subsurface (50 Ωm) using a circular loop ($d = 100$ m), 100 vol.% water content, 60°N inclination, pulse length $\tau = 40.3$ ms.

B. Appendix to Chapter 4.2

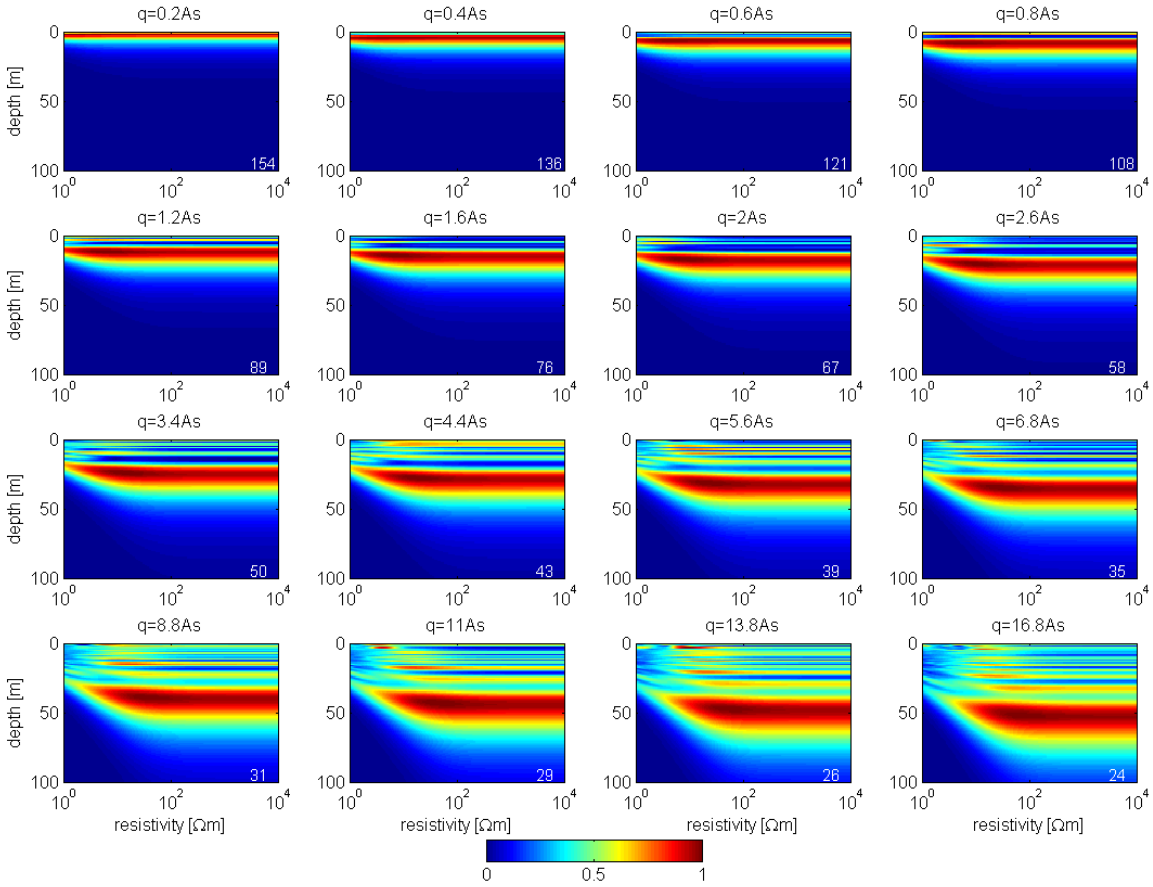

Figure B.1.: Image of the amplitude of the MRS kernel function of selective pulse moments for homogeneous half-spaces with resistivities between 1 and 10000 Ωm. The amplitudes are normalised on their maximum value, that is indicated in the lower right corner of each plot. The data are calculated using a circular loop ($d = 50$ m) and magnetic field intensity of 48000 nT and 60°N inclination.

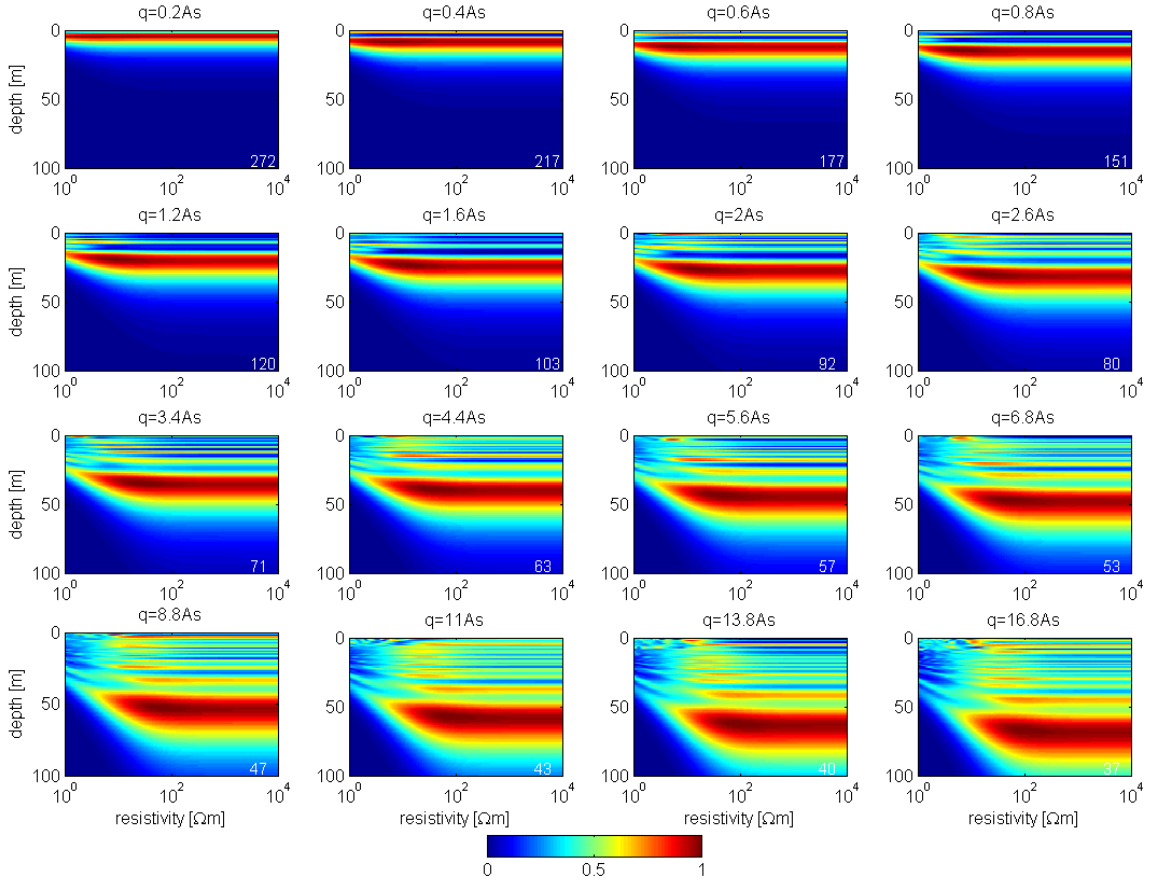

Figure B.2.: Image of the amplitude of the MRS kernel function of selective pulse moments for homogeneous half-spaces with resistivities between 1 and 10000 Ωm. The amplitudes are normalised on their maximum value, that is indicated in the lower right corner of each plot. The data are calculated using a circular loop ($d = 50$ m, 2 turns) and magnetic field intensity of 48000 nT and 60°N inclination.

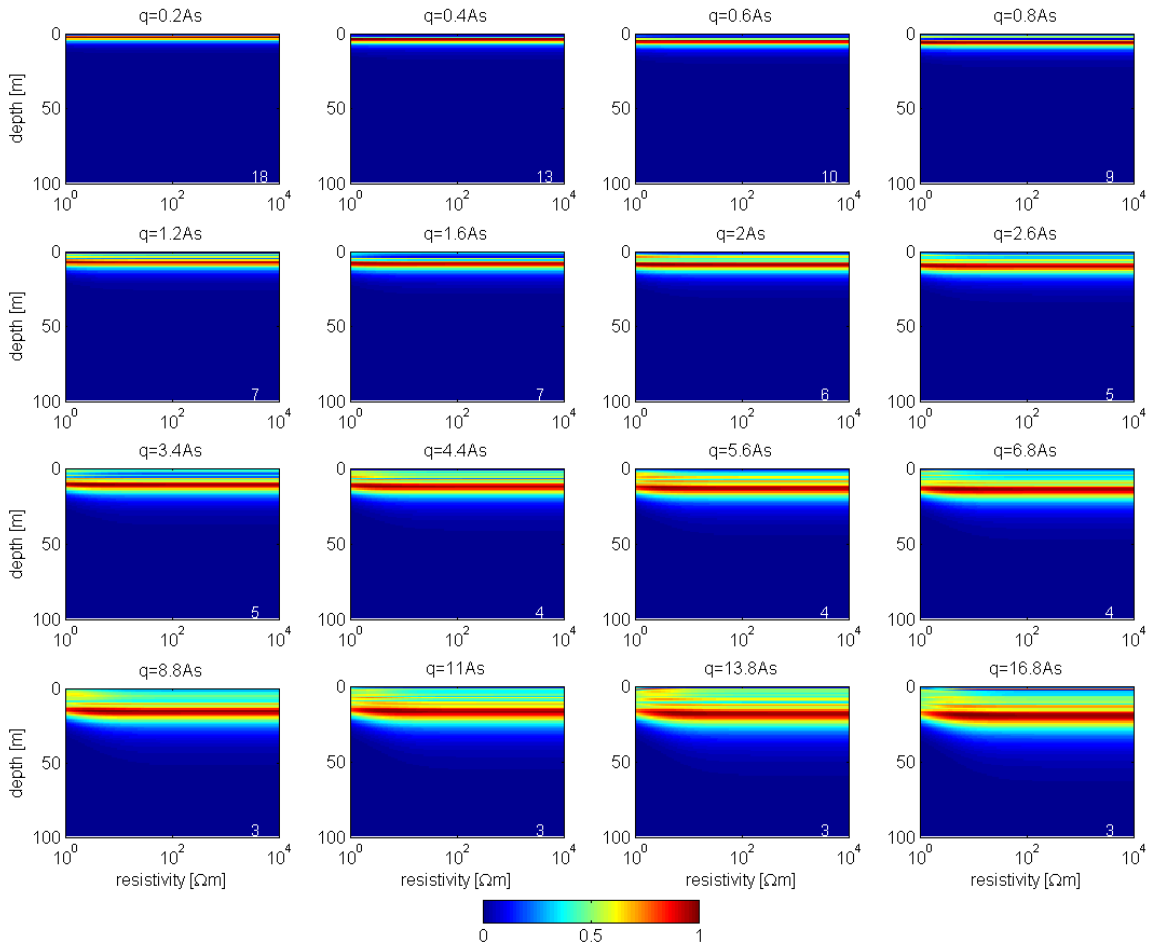

Figure B.3.: Image of the amplitude of the MRS kernel function of selective pulse moments for homogeneous half-spaces with resistivities between 1 and 10000 Ωm. The amplitudes are normalised on their maximum value, that is indicated in the lower right corner of each plot. The data are calculated using a circular loop ($d = 10$ m) and magnetic field intensity of 48000 nT and 60°N inclination.

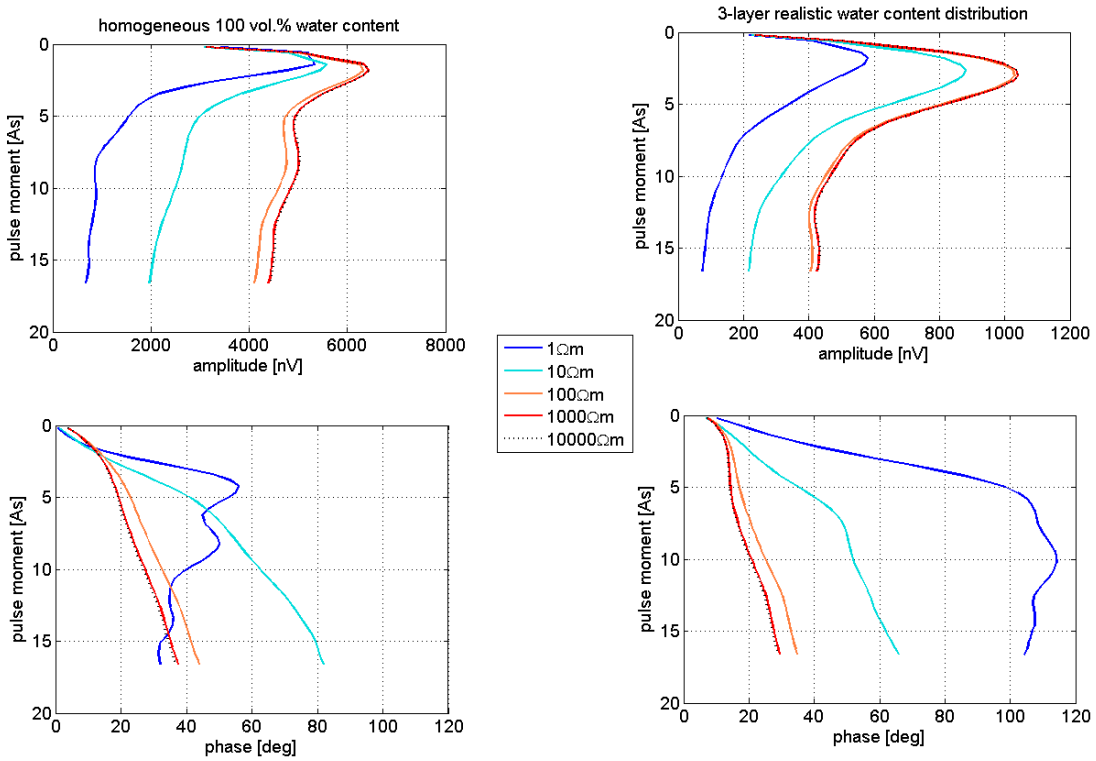

Figure B.4.: MRS data using 100 vol.% water content (left) and a realistic water content distribution (5 vol.% for the 1st and 3rd layer and 30 vol.% for the 2nd layer between 25 m and 50 m, right) for a 3-Layer model with resistivities of 50 Ωm of the 1st and 3rd layer and for several resistivities between 1 and 10000 Ωm of the 2nd layer. The data are calculated using a circular loop (d = 100 m) and magnetic field intensity of 48000 nT and 60°N inclination.

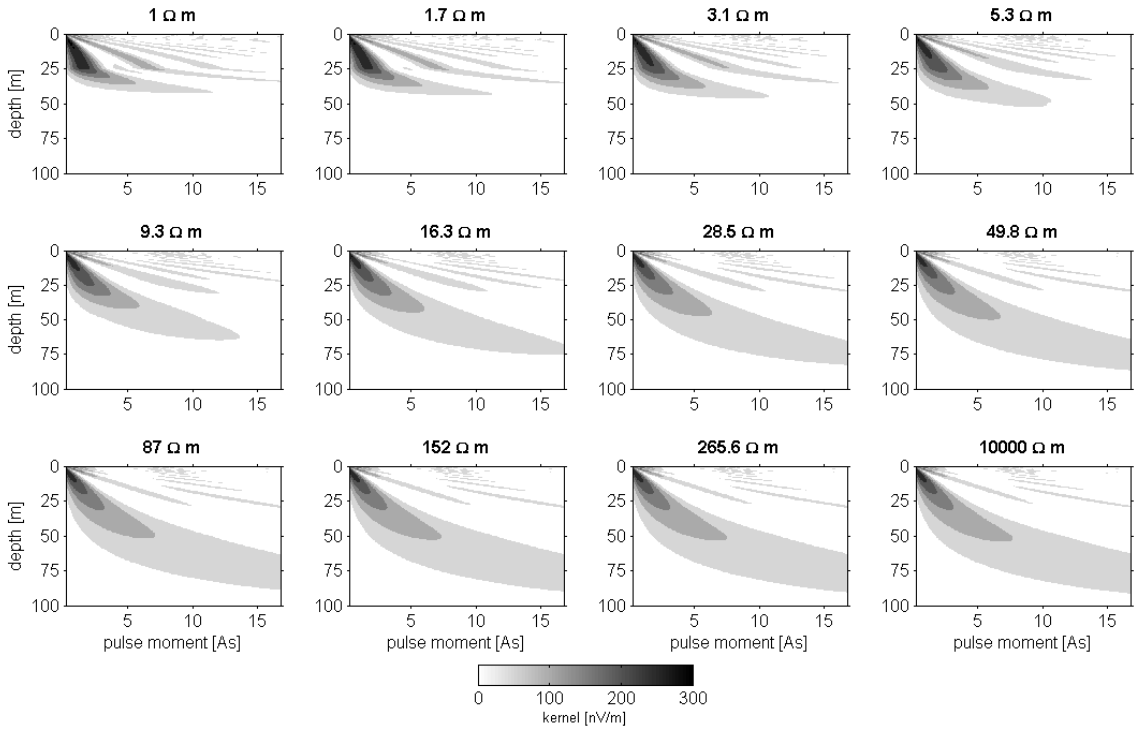

Figure B.5.: Contour plot of the amplitude of the 1D MRS kernel function for selective resistivities using a 3-Layer model with resistivities of 50 Ωm of the 1st and 3rd layer and for resistivities between 1 and 10000 Ωm of the 2nd layer (shown in the title of each plot). The data are calculated using a circular loop (d = 100 m) and magnetic field intensity of 48000 nT and 60°N inclination.

C. Appendix to Chapter 6.4

model no.	1	2	3	4	5	6	7	8
thickness 1st layer [m]	5	5	5	5	10	10	10	10
thickness 2nd layer [m]	5	10	25	50	5	10	25	50
model no.	9	10	11	12	13	14	15	16
thickness 1st layer [m]	25	25	25	25	50	50	50	50
thickness 2nd layer [m]	5	10	25	50	5	10	25	50

Table C.1.: Numeration and layer thickness of the synthetic models. The principal resistivity distribution is the same for all models: 50 Ωm for the 1st layer, 5 Ωm (Fig. C.1) or 500 Ωm (Fig. C.2) for the 2nd layer and 50 Ωm for the 3rd layer. Also the principal water content distribution is the same for all models: 5 vol.% for the 1st layer, 30 vol.% for the 2nd layer and 5 vol.% for the 3rd layer.

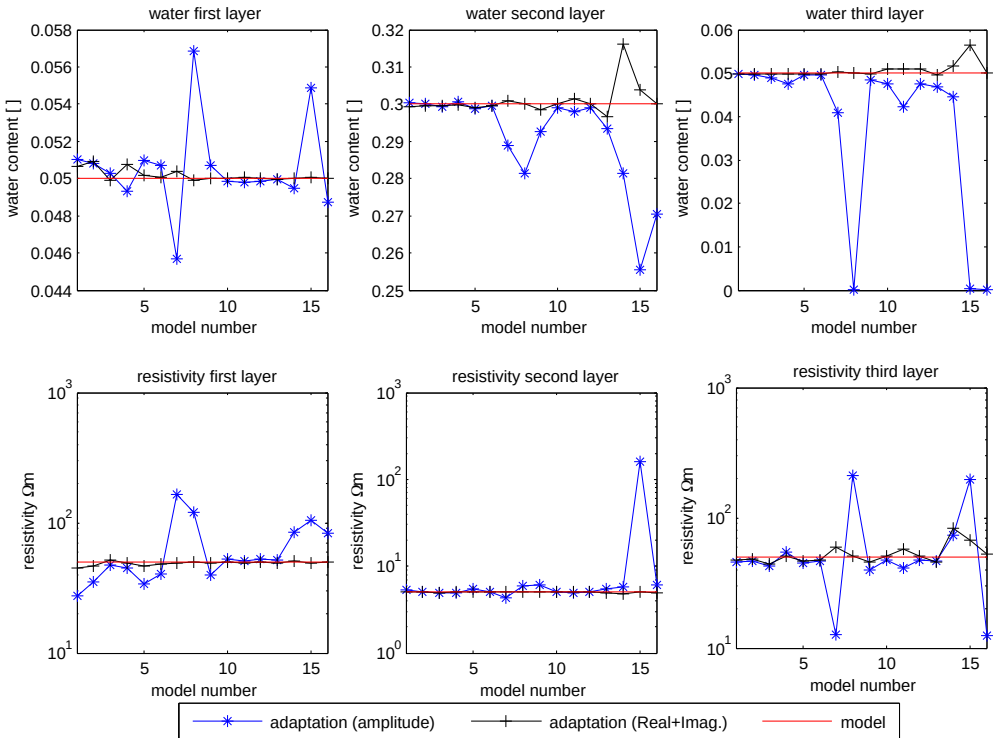

Figure C.1.: Inversion result for a resistivity of 5 Ωm of the aquifer. The numeration is explained in Tab. C.1. The layer thicknesses are given as a priori information. The used MRS data are calculated for a circular loop (d =100 m) with pulse moments between 2 and 16 As using a magnetic field of 48000 nT, 60°N. The inversion results for a pure amplitude inversion are compared with those of a complex inversion (fitting amplitude and phase).

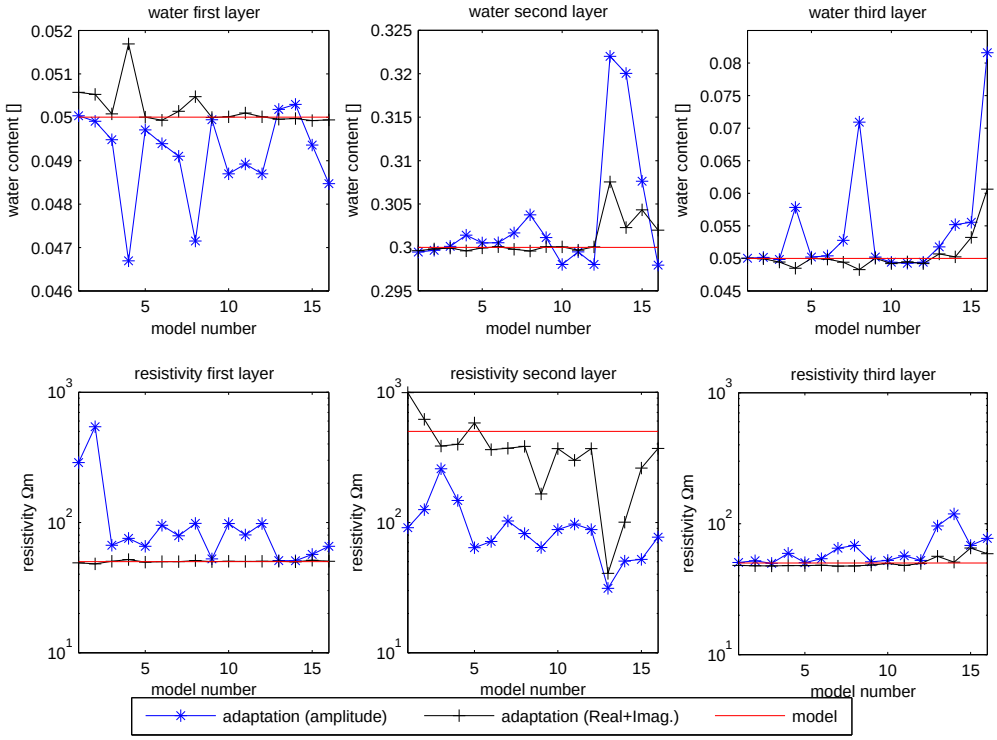

Figure C.2.: Inversion result for a resistivity of 500 Ωm of the aquifer. The numeration is explained in Tab. C.1. The layer thicknesses are given as a priori information. The used MRS data are calculated for a circular loop ($d = 100$ m) with pulse moments between 2 and 16 As using a magnetic field of 48000 nT, 60°N. The inversion results for a pure amplitude inversion are compared with those of a complex inversion (fitting amplitude and phase).

List of Figures

List of Tables